UNIVERSITY OF CALIFORNIA
RIVERSIDE

Application of Solid-State NMR to Photoreaction Mechanism in Material Science

A Dissertation submitted in partial satisfaction
of the requirements for the degree of

Doctor of Philosophy

in

Physics

by

Lingchao Zhu

December 2013

Dissertation Committee:
Dr. Leonard J. Mueller, Co-Chairperson
Dr. Leonid Pryadko, Co-Chairperson
Dr. Ward P. Beyermann

The Dissertation of Lingchao Zhu is approved:

_____

_____

Committee Co-Chairperson

_____

Committee Co-Chairperson

University of California, Riverside

ACKNOWLEDGMENTS

The text of this thesis in part is a reprint of the material as it appears in:

CrystEngComm, 2012, 14, 7792-7799

I would like to acknowledge the following individuals for their contributions:

Dr. Leonard J. Mueller directed and supervised the research which forms the foundation of this thesis.

Dr. Leonid Pryadko provided suggestions and guide for this physics dissertation.

The co-authors Dr. Christopher J. Bardeen and Dr. Taehyung Kim prepared the samples of 9-MA and 4Cl-CA and provided valuable discussions on experiments for Chapter Ⅱ and Ⅲ.

Dr. Lingyan Zhu prepared the powder sample of 9TBAE (^{13}C labeled).

Dr. John M. Kaiser introduced the probe construct technique.

Daniel Adams helped in the design and mechanic fabrication of the goniometer part of single-crystal probe.

Dr. Ye Tian and Dr. Jinfeng Lai assisted in part of solid-state NMR experiments.

Ryan Kudla assisted in drying the sample of 9-MA.

CrystEngComm, 2012, 14, 7792-7799

http://dx.doi.org/10.1039/C2CE25811K

I would like to express my sincere gratitude to my advisor, Professor Leonard J. Mueller, for his patience and support to help me get through the tough part of my research. He is more like a knowledgeable and warm-hearted friend, to encourage and motivate me on my way to pursuing the Ph.D.

I wish to express my sincere thanks to Professor Leonid Pryadko, my co-advisor, who introduced and guided me on the physics track toward my Ph.D. research.

I owe my sincere gratitude to my reading committee members, Professor Ward P. Beyermann, and my candidacy committee members, Professor Shan-Wen Tsai and Professor Chia-en Chang, for their detailed and valuable comments.

I really want to give my special thanks to my family. My parents support me with their blessing and my wife, Xin, is always staying with me in her love. With their love, I always feel in full power during my Ph.D. life.

Last but not least, I would also like to thank all of my lab mates and friends who made my Ph.D. life colorful and enjoyable.

Riverside, CA, USA, October 2013

Lingchao Zhu

ABSTRACT OF THE DISSERTATION

Application of Solid-State NMR to Photoreaction Mechanism in Material Science

by

Lingchao Zhu

Doctor of Philosophy, Graduate Program in Physics
University of California, Riverside, December 2013
Dr. Leonard J. Mueller, Co-Chairperson
Dr. Leonid Pryadko, Co-Chairperson

Solid-state nuclear magnetic resonance (NMR) has been frequently used in solving protein structures and material sciences. The benefits from solid-state NMR, such as Magic-Angle-Spinning, contribute a lot to improving the resolution of NMR spectrum, which is important in protein structure assignments. This thesis will bring another view of benefits from solid-state NMR. The photochemical reaction of materials can be clearly drawn by solid-state NMR during the photodimerization. Single-crystal NMR is another powerful tool for investigating the photochemical reaction, which has orientation dependence. The spin-lattice relaxation curve is also useful for determining the domain interactions and domain sizes.

Characteristics of anthracene-9-carboxylic acid tert-butyl ester (9TBAE) during the photodimerization were investigated in chapter two. The objective is to prove the photoreaction will form a metastable intermediate crystal and this intermediate structure will have the ester sidegroups pointing inward prior to rotating to the lower energy

outward-facing position. A newly designed single crystal goniometer probe was used for ^{13}C CP NMR experiments of 9TBAE. The design details, benefits and performance of this home-built probe are presented in this chapter. This probe has the two axes adjustment system and Hall Effect sensor for sample tube orientation. The ester sidegroups rotation was determined by the change of quartet peaks based on ^{13}C dipolar coupling.

The photodimerization and T1 measurement of 9-methylanthracene (9-MA) by ^{13}C solid-state NMR were investigated in chapter three. ^{1}H T1 relaxation curves were obtained for both the monomer and the dimer. A series of Solid-state NMR spectra provide the process of photodimerization based on various UV exposure times. The spin diffusion rate between the monomer and the dimer is quite small from a global fitting of spin diffusion model. It will contribute to determine that the domain size is over 1000 nm, which indicates the formation of large dimer domains in our sample.

The photochemical dynamics of crystals composed of 4-chlorocinnamic acid (4Cl-CA) was investigated in chapter four, whose photochemistry is dominated by an irreversible {2+2} photodimerization reaction. The ^{13}C CPMAS solid-state NMR spectra showed the whole progress of photodimerization. While 4Cl-CA is probably not of practical interest as a photomechanical material, our results provide evidence that the photoinduced twisting of this class of photoreactive crystals is a general phenomenon. We discuss possible mechanisms for this size dependence, and propose a mechanism by which the mechanical response of photoreactive molecular crystals may be enhanced by reducing the crystal dimensions.

Table of Contents

List of Figures

Chapter 1

Chapter 2

Chapter 3

Chapter 4

List of Tables

Chapter 1

Introduction and Background

1.1 Solid-State Nuclear Magnetic Resonance Spectroscopy

1.1.1 Nuclear Magnetic Resonance

Nuclear magnetic resonance (NMR), referred to a physical phenomenon, is that nuclei in a magnetic field absorb and re-emit electromagnetic radiation. It was first discovered and measured in 1938 by Isidor Rabi [1]. Then Felix Bloch and Edward Mills Purcell put application of NMR on liquids and solids in 1946 [2]. Some specific quantum mechanical magnetic properties of the atomic nucleus can be observed by NMR spectroscopy. Today, NMR spectroscopy is widely used to study molecular physics, crystals, and non-crystalline materials. Also, some advanced imaging techniques use NMR to exploit medical diagnosis, such as magnetic resonance imaging (MRI).

If nuclei have a spin of one-half, like 1H or 13C, it has two possible spin states: m = 1⁄2 or m = −1⁄2. If a nucleus is put in a magnetic field, however, the interaction between the nuclear magnetic moment and the external magnetic field will not let the two states stay at the same energy level. In Figure 1.1, the energy difference between these two states is:

$$\Delta E=\gamma\hbar B_0$$

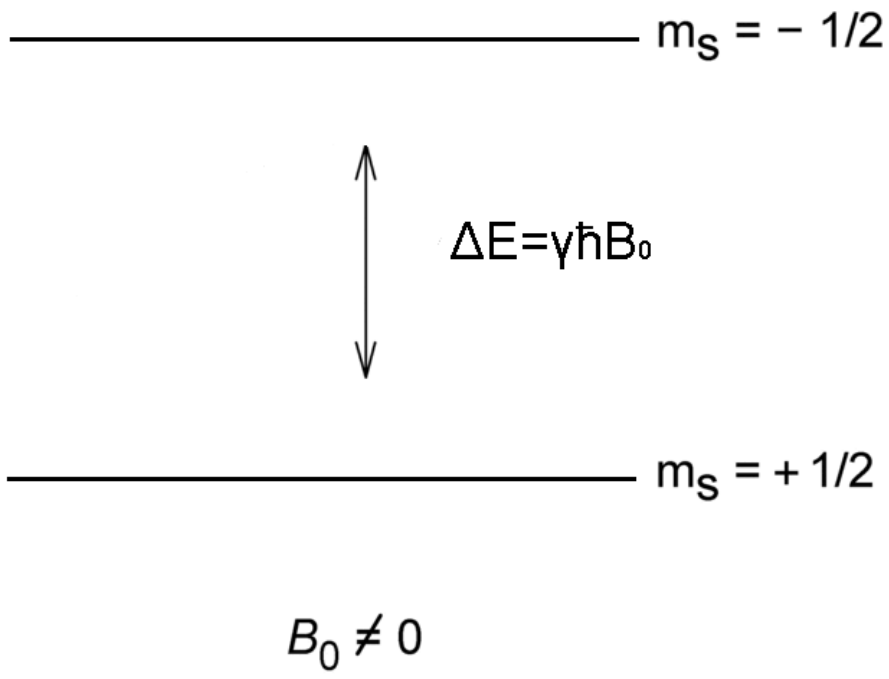

Figure 1.1 Splitting of nuclei spin states in external magnetic field

When electromagnetic radiation of the corresponding frequency is applied to match the energy difference:

$$\Delta E = 2\pi\hbar\upsilon = \gamma\hbar B_0$$

The magnetic resonant absorption by nuclear spins will occur. Thus, a magnetic resonance absorption will only occur when $\upsilon = \gamma B_0/2\pi$. Such magnetic resonance frequencies will be in the range of the radio frequency (or called RF). We can see, in Figure 1.2, a line in the spectrum is associated with the resonant absorption of the relevant energy gap.

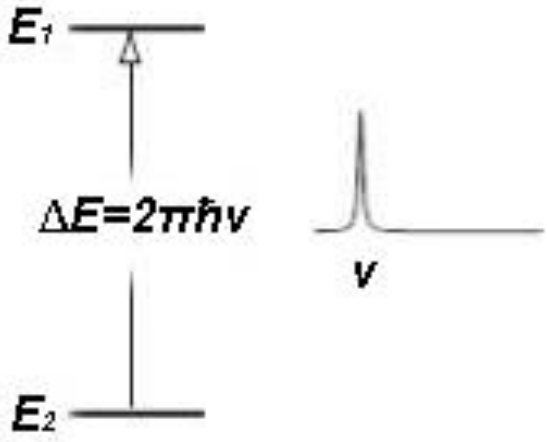

Figure 1.2 A line in the spectrum is associated with relevant energy gap

NMR spectroscopy is one of the powerful techniques used to obtain information of physical and chemical properties about molecules due to the chemical shift, Zeeman Effect, or a combination of both, on the resonant frequencies of the nuclei present in the sample. It can provide detailed information on the mechanism, dynamics and three-dimensional structure of molecules in solution and the solid state.

1.1.2 Solid-State Nuclear Magnetic Resonance

The technique, crystallography, is frequently applicable to molecules in solid state. In solid state NMR, anisotropic interactions have a substantial influence on the behavior of nuclei spins. Though nuclear magnetic resonance can be used to study solids state materials, it is especially challenging to obtain extensive molecular structural information in the solid state.

Anisotropic interactions will always bring a line-broadening effect in NMR spectra, because those interactions modify the nuclear spin energy. However, in some cases, the presence of anisotropic interactions can be particularly desired, since they provide structural detail of molecule, such as orientation parameters.

This is different from liquid-state NMR. For a classical liquid-state NMR experiment, anisotropic interactions can be neglected on the time-scale of the NMR experiment, as an averaging of anisotropic interactions can be achieved by Brownian motion.

1.1.3 Solid-State NMR Hamiltonian

In quantum mechanics, the Hamiltonian is the operator corresponding to the total energy of the system. The Hamiltonian of the interaction of the nucleus with the magnetic field is:

$$\boldsymbol{H} = -\gamma \vec{S} \bullet \vec{B}$$

In NMR rotating frame [3-4], for the nuclear spin of one-half, the NMR Hamiltonian [4-6] is:

$$\boldsymbol{H} = \boldsymbol{H}_{CSA} + \boldsymbol{H}_{ICS} + \boldsymbol{H}_{D} + \boldsymbol{H}_{J} + \boldsymbol{H}_{RF}$$

$\boldsymbol{H}_{CSA}$ and $\boldsymbol{H}_{ICS}$ are chemical shift anisotropy and isotropic chemical shift Hamiltonians [7-8]. $\boldsymbol{H}_{D}$ and $\boldsymbol{H}_{J}$ are Hamiltonians of dipolar coupling and scalar coupling (J-coupling). $\boldsymbol{H}_{RF}$ is radio frequency Hamiltonian. Spin-rotation interaction and quadrupolar interactions are beyond the discussion of this thesis.

1.2 Solid-State NMR Techniques and Methods

1.2.1 Magic Angle Spinning

Magic angle spinning was first described in 1958 by Edward Raymond Andrew at Nottingham University [9]. In nuclear magnetic resonance, magic angle spinning (MAS) is a technique used to increase the resolution in solid-state NMR spectroscopy. If the sample is spinning at a frequency of 1 to 70 kHz and is tilted by the angle θ_m (approximately 54.74 °, where $\cos^2\theta_m=1/3$) with respect to the direction of the magnetic field B_0, as indicated in Figure 1.3, the broad lines from anisotropic interactions will become narrower. This could lead to better spectrum for identification and analysis.

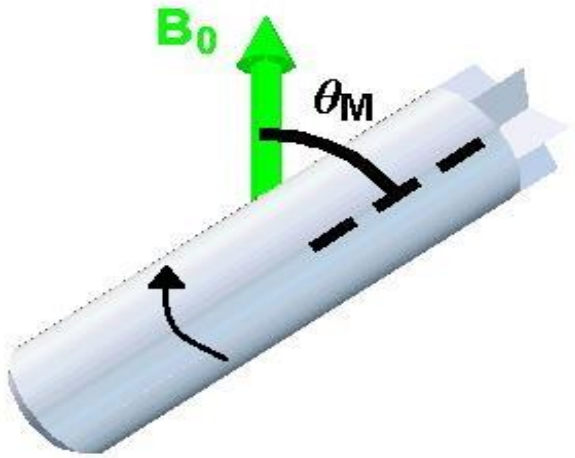

Figure 1.3 Magic angle spinning: the sample tube is rotating and the rotating axis is tilted by the magic angle θ_m

From NMR Hamiltonian view, the dipole coupling term averages to zero because it is time-dependent. Meanwhile, the chemical shift anisotropy term averages to a non-zero value and often causes spinning sidebands which can be used to determine the chemical shift anisotropy of the nuclei [10].

1.2.2 Cross Polarization

Cross polarization (CP) is another powerful technique in solid state NMR experiments. CP was first created by Michael Gibby and Alexander Pines in 1972 [11-12]. They realized that the signal of nuclei with a low gyromagnetic ration (e.g. ^{13}C) can be enhanced by using magnetization transformation from those with a high gyromagnetic ratio (e.g. ^{1}H). The benefit of this technique is that the polarization of dilute spins (e.g. ^{13}C) is increased greatly by the abundant spins (e.g. ^{1}H).

This polarization transfer will require series of π pulses to lock the magnetization on x-y (transverse) plane. In experiment, the RF pulses applied on two channels must satisfy the Hartmann-Hahn condition (e.g. $^{1}H \rightarrow {}^{13}C$) [13]:

$$\gamma_{1H} B_{1H} = \gamma_{13C} B_{13C}\,; \qquad \omega_{1H} = \omega_{13C}$$

In this instance ($^{1}H \rightarrow {}^{13}C$), by matching the condition above, the rotating field B_1 of carbon channel must be 4 times stronger than the proton channel. Besides a much stronger signal, this technique also gives faster relaxation time (it now depends on T1 of ^{1}H). It is also used in multi-dimensional NMR experiment to transfer magnetization between different nuclei.

With MAS, CP-MAS [14] is a basic starting point of most pulse sequences in solid-state NMR spectroscopy. Under MAS, the relationship between power on the RF coil and sample rotation rate is well defined by the Hartmann-Hahn condition. The CP conditions are optimized as one of the routine tasks during solid-state NMR experiment in this work.

1.2.3 Scalar Coupling

Scalar coupling arises due to indirect interaction between the two nuclear spins through the electrons connecting the nuclei. Comparing to dipolar coupling (over 100 Hz to 1000 Hz) in solid state NMR, magnitude of scalar coupling is typically very small (over 10 to 100 Hz). However, scalar coupling based spectrum can help us solve the structures of big proteins under fast MAS and proton decoupling methods [15]. So scalar coupling based experiments now become equally important in solid state NMR as the dipolar coupling experiments.

Scalar coupling can mainly provide three parts of information: the multiplicity, the magnitude of the coupling and the sign of the coupling. With this feature, we can use spectra editing to improve resolution of 2D NMR spectrum based on scalar coupling parameters. This spectra editing method could be a potential tool to do peak assignments for big proteins. Also, it is very potent in small protein peak assignments, such as GB1.

In liquid state NMR, scalar coupling is regularly used because most magnetization transfer is done through the J-coupling, even in multi-dimensional experiments, such as COSY, HSQC and HMQC [16-17].

1.2.4 Decoupling

The magnetization transformation (CP) makes cross polarization work, but it can also lead to line-broadening. Spin interactions can be removed (decoupled) by using heteronuclear decoupling sequences, such as TPPM, XiX, SPINAL64 [18-20].

The idea of decoupling sequence is based on averaging dipolar interaction after a rapid flip of proton magnetization. ^{13}C NMR spectroscopy is usually run fully proton decoupled. In this case, ^{13}C spectra should have very narrow line-shape and high signal/noise ratio. So we can get the most information of carbon atoms from the chemical shift.

Homonuclear decoupling is rare in unlabeled sample (low natural abundance), such as ^{13}C-^{13}C, so it is beyond the discussion of this thesis. However, homonuclear coupling may give us more structure information in labeled sample, especially in single-crystal sample static NMR experiment. It is very sensitive to the dipolar coupling between the atoms and the distribution of atoms in cell unit. In this work, we will see that the splitting peaks of ^{13}C dipolar coupling will be clearly different under the photo radiation of crystal sample. It can provide detailed information of photodimerization from the chemical shift and peak shape.

1.2.5 Phase Cycling

Phase cycling can eliminate the signals from other pathways but select one particular pathway. To do this, the phases of pulse sequence are manipulated to match the receiver phases.

One common example is double quantum filtered COSY pulse sequence. In Figure 1.4, the coherence transfer pathway and phase cycle selected pathway is shown [21].

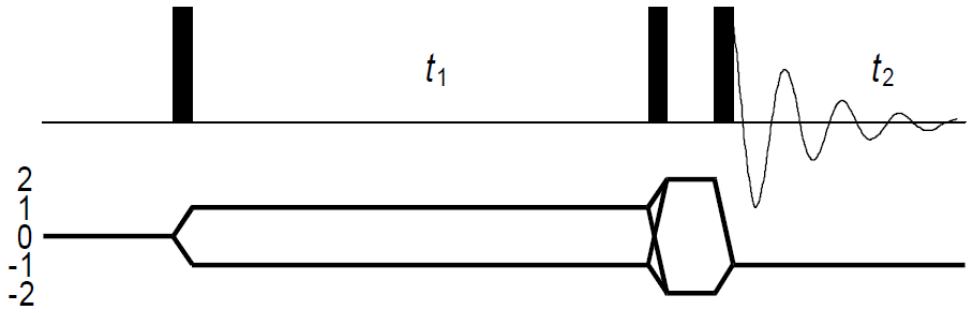

Figure 1.4 Coherence transfer pathway for DQF COSY experiment [21]

With phase cycling technique, selecting specific detecting signal in multi-dimensional NMR experiment becomes achievable. It can also help to isolate influences between pulses. The general idea of phase cycling is, adding up all possible contributions first and then combining subsequent signals to cancel out the unwanted ones.

There are many other techniques and methods for NMR spectroscopy, such as chemical exchange [22-24] and nuclear overhauser effect [25-27], which help extract dynamic information and improve NMR experiment sensitivity.

1.3 Objectives

The main objective of this thesis is to investigate the application of solid-state NMR in photo-responsible material science. This research will provide a straightforward view for beneficial use of solid-state NMR in explanation of photoreaction mechanism. The organization of thesis is described as follows.

1. Chapter two will investigate characteristics of anthracene-9-carboxylic acid tert-butyl ester during the photodimerization [28]. The objectives are to prove the photoreaction will form a metastable intermediate crystal and this intermediate structure will have the ester sidegroups pointing inward prior to rotating to the lower energy outward-facing position. The solid-state NMR experiments are performed in home-built single crystal goniometer probe. As the single-crystal NMR is orientation dependent, the appropriate angle of sample tube will be calibrated by two axes adjustment and Hall Effect sensor on the probe. A set of quartet peaks based on ^{13}C dipolar coupling will be accomplished to determine ester sidegroups rotation at different photo radiation times.
2. Chapter three will focus on T1 measurement of 9-methylanthracene by solid-state NMR. The objective is to investigate the spin diffusion between the monomer and the dimer [29]. The T1 relaxation curves for the monomer and the dimer based on various exposure times will provide characteristics of this two-spin system. A global fitting of spin diffusion model will be accomplished to determine the spin diffusion rate between the monomer and the dimer. Then the domain structure

generated by photodimerization will tell us where the reaction happens in the monomer.

3. Chapter four will investigate the photochemical dynamics of crystals composed of 4-chlorocinnamic acid. This chapter will contribute to understand crystal morphology of 4-chlorocinnamic acid on the photoresponsive behavior. Solid-state NMR plays a vital role in explaining possible mechanisms and provides clear view of photodimerization. With powder X-ray diffraction and optical and electron microscopy, this work shows that photo-induced twisting can be observed in photoreactive systems.

Throughout this thesis, techniques and methods above are used to improve the sensitivity and resolution of NMR experiment. The use of solid-state NMR for photochemical reaction of materials leads to unveiling another potent pathway for material science research.

References

1. Rabi, I.I.; Zacharias, J.R.; Millman, S. and Kusch, P. Physical Review, 1938, 53 (4), 318–327.

2. Filler, Aaron. The History, Development and Impact of Computed Imaging in Neurological Diagnosis and Neurosurgery: CT, MRI, and DTI. Nature Precedings, 2009

3. Becher, E.D. High Resolution NMR, Theory and Chemical Applications. Second Edition, Academic Press, New York, 1980.

4. Demco, D. E.; Tegenfeldt, J.; Waugh, J. S. Physical Review B 1975, 11, 4133-4151.

5. Mehring, M. Principle of High Resolution NMR in Solids, Second Edition, 1983.

6. Haeberlen, U. High Resolution NMR in Solids: Selective Averaging, 1976.

7. Herzfeld, J.; Berger, A. E. Journal of Chemical Physics 1980, 73, 6021-6030.

8. Maricq, M. M.; Waugh, J. S. Journal of Chemical Physics 1979, 70, 3300-3316.

9. Andrew, E. R.; Bradbury, A.; Eades, R. G. Nature, 1958, 182, 1659.

10. Wu, G.; Sun, B.; Wasylishen, RE.; Griffin, RG. Journal of Magnetic Resonance 2006, 124, 366–371.

11. Pines, A.; Waugh, J. S.; Gibby, M. G. Journal of Chemical Physics 1972, 56, 1776-1777

12. Pines, A.; Gibby, M. G.; Waugh, J. S. Journal of Chemical Physics 1973, 59, 569-590.

13. Hartmann, S.R.; Hahn E.L. Physical Review 1962, 128, 2042.

14. Schaefer, J.; Stejskal, E. O. Journal of the American Chemical Society 1976, 98, 1031-1032.

15. Tian,Y.; Chen, L.; Niks, D.; Kaiser, J.M.; Lai, J.; Rienstra, C.M.; Dunn, M.F.; Mueller, L.J. Physical Chemistry Chemical Physics 2009, 11(32), 7078-7086.

16. Bodenhausen, G.; Ruben, D. J. Chemical Physics Letters 1980, 69, 185-189.

17. Kay, L. E.; Keifer, P.; Saarinen, T. Journal of the American Chemical Society 1992, 114, 10663-10665.

18. Bennett, A. E.; Rienstra, C. M.; Auger, M.; Lakshmi, K. V.; Griffin, R. G. Journal of Chemical Physics 1995, 103, 6951-6958.

19. Detken, A.; Hardy, E. H.; Ernst, M.; Meier, B. H. Chemical Physics Letters 2002, 356, 298-304.

20. Fung, B. M.; Khitrin, A. K.; Ermolaev, K. Journal of Magnetic Resonance 2000, 142, 97-101.

21. Keeler, James. Understanding NMR Spectroscopy 2002.

22. Newmark, R. A.; Sederhol, C.H. Journal of Chemical Physics 1965, 43, 602-623.

23. Binsch, G. Journal of the American Chemical Society 1969, 91, 1304-1309.

24. Bain, A. D. Progress in Nuclear Magnetic Resonance Spectroscopy 2003, 43, 63-103.

25. Overhauser, A. W. Physical Review 1953, 92, 411-415.

26. States, D. J.; Haberkorn, R. A.; Ruben, D. J. Journal of Magnetic Resonance 1982, 48, 286-292.

27. K. Wuthrich, NMR of Proteins and Nucleic Acids, Wiley, New York, 1986.

28. Zhu, L.; Agarwal, A.; Lai, J.; Mueller, L.J.; Bardeen, C.J. Journal of Materials Chemistry 2011, 21, 6258-6268.

29. Takegoshi, K.; Nakamura, S.; Terao, T. Solid State Nuclear Magnetic Resonance 1998, 11, 189-196.

CHAPTER 2

Characterization of Anthracene-9-carboxylic acid tert-butyl ester via Solid-State NMR Single Crystal Goniometer Probe with Hall Effect Sensor

This chapter focuses on studying characteristics of anthracene-9-carboxylic acid tert-butyl ester (9TBAE) during the photodimerization. It aims to prove the photoreaction will form a metastable intermediate crystal and this intermediate structure will have the ester sidegroups pointing inward prior to rotating to the lower energy outward-facing position. A newly designed single crystal goniometer probe was used for the studies of 9TBAE in this thesis. The design details, benefits and performance of this home-built probe are presented in this chapter. ^{13}C CP NMR experiments were performed at varied orientation with the two axes adjustment system. The Hall Effect sensor on this probe was used for calibration of the sample tube orientation. A set of quartet peaks based on ^{13}C dipolar coupling was accomplished and ester sidegroups rotation was determined at different photo radiation times.

2.1 Introduction

2.1.1 Anthracene-9-carboxylic acid tert-butyl ester (9TBAE)

People have been studying organic solid-state photoreactions for a long time to solve the problems like how spatial constraints influence chemical reactivity [1-3]. Many crystal samples show that the crystal molecules can induce crystal deformation with physical reconstruction [4-5].

To get better understanding origins of the photomechanical response in molecular level, we choose anthracene-9-carboxylic acid tert-butyl ester (9TBAE) as our candidate. The crystalline nanorods composed of 9TBAE keep unaffected after 15% expansion [6]. Figure 2.1 shows the molecular structure of 9TBAE.

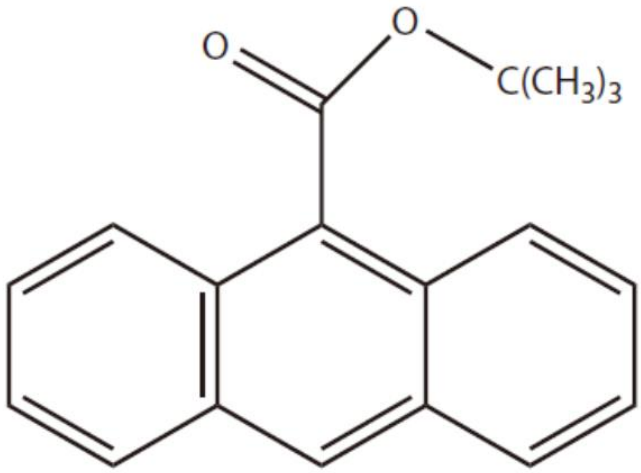

Figure 2.1 Molecular structure of anthracene-9-carboxylic acid tert-butyl ester (9TBAE)

In each cell unit, there are four monomer molecules of 9TBAE before UV irradiation. After UV light exposure, the monomer crystal will react to form the solid-

state reacted dimer (solid-state reacted dimer, SSRD) crystal. This metastable dimer intermediate will convert into low energy dimer crystal structure (solution grown dimer, SGD) over a few months [7]. Figure 2.2 shows the whole progress.

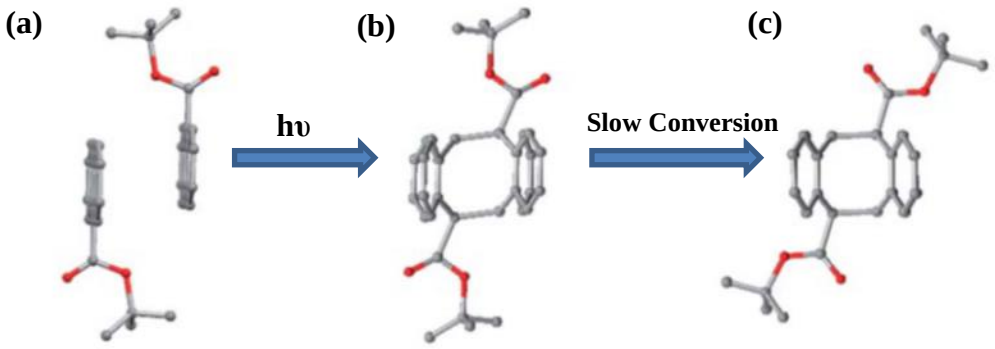

Figure 2.2 Photodimerization progress of 9TBAE (a) monomer (b) PRD: partially reacted dimer (c) SGD

If PRD is fully photo reacted, it becomes the solid-state reacted dimer (SSRD). The difference between PRD and SGD is that the ester sidegroups of the PRD are inward-facing but rotates almost 180 °to face outward for in the SGD.

In this work, we will grow 9TBAE single crystal to do the ^{13}C NMR experiment because the single crystal NMR is orientation dependent. It will give us more details about the ester sidegroups in PRD and SSRD. This information can help us conform that the ester sidegroups in PRD or SSRD are facing inward, which is a big benefit from single crystal NMR.

2.1.2 NMR Probe and RF Electronics

The most important thing for NMR probe RF circuit design is the power deposition for nutation frequencies. It is the power-handling capability for the probe because higher power deposition often means better sensitivity and resolution in the spectrum. Coil quality factor (Q) is another standard reference of probe performance.

$$Q = \frac{Im[Z]}{Re[Z]} = \frac{stored\ energy}{dissipated\ energy}$$

Before the discussion about those probe performances, let's have a review on RF electronics. The impedance of an ideal resistor is Z_R=R so there is no phase difference between the voltage and current. The impedance of inductors and capacitors are as follows:

$$Z_L = j\omega L \quad \text{and} \quad Z_C = \frac{1}{j\omega C}$$

For a RLC circuit, in Figure 2.3, the self-resonance frequency is $f = \frac{1}{2\pi\sqrt{LC}}$

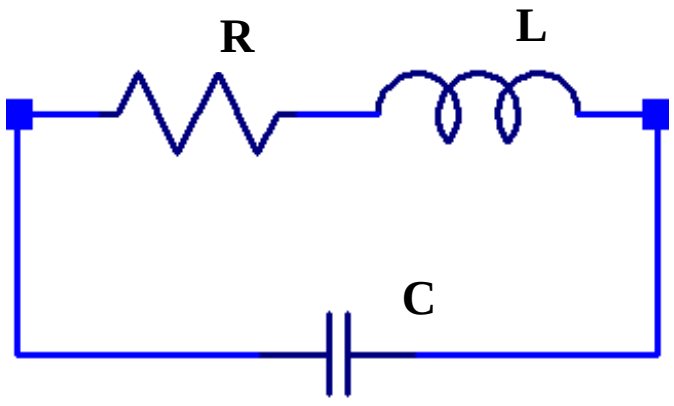

Figure 2.3 RLC circuit (R-resistor, L-inductor, C-capacitor)

Inductance for a single-layer solenoid is obtained approximately:

$$\mathrm{L} = \frac{n^2 r^2}{9r + 10l} 10^{-3}$$

Where the inductance is in nH, n is the number of turns, r is the radius in inches to the solenoid center and l is the length of solenoid in inches.

The coil of probe will wrap the sample entirely to get the most efficiency of power, so the coil geometry should be homogeneous for each turn. To reduce the radial inhomogeneity, flattened wire can be used to make probe coil.

The common impedance reference of transmit-receive switching circuits, amplifiers and other circuits designs is 50 Ω. So the design of probe circuit will have two jobs to do: (1) transform the impedance of each channel (each frequency in NMR) to 50 Ω; (2) isolate the signal (or frequency) from each channel. The single channel resonance circuit is showed in Figure 2.4 below [8]:

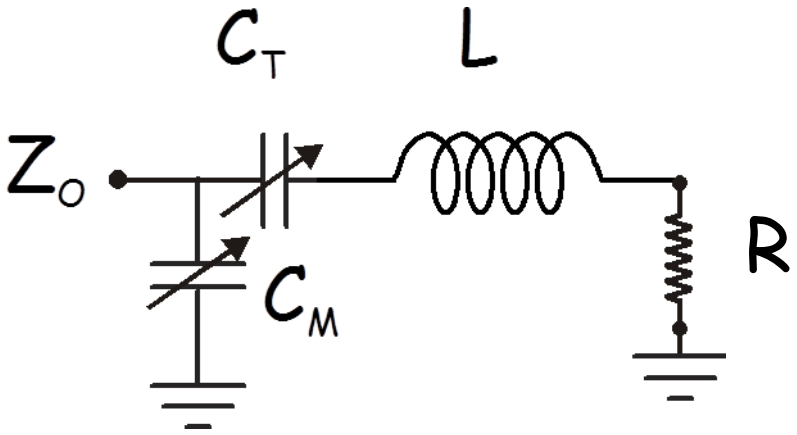

Figure 2.4 Single channel resonance circuit (Z_0-Impedance, C_T-tuning capacitor, C_M-matching capacitor, L-coil, R-other resistors)

The impedance matching formula is:

$$\frac{1}{Z_0} = \frac{1}{Z_{in}} = j\omega C_M + \frac{1}{\frac{1}{j\omega C_T} + j\omega L + R} = R' + jX$$

Z_0=50 Ω is the impedance reference for all the circuits designs. First, we will set X=0 to find resonant frequency, which is approximately equal to $\frac{1}{\sqrt{LC_T}}$. Then we can choose C_T/C_M to make R'=1/Z_0 impedance matching. This is the standard procedure for tuning and matching each channel (each frequency). However, sometimes it is hard to distinguish the function of the tuning capacitor and matching capacitor. Tuning and matching procedure is complex from many combinations. Figure 2.5 shows the tuning and matching procedure in the software.

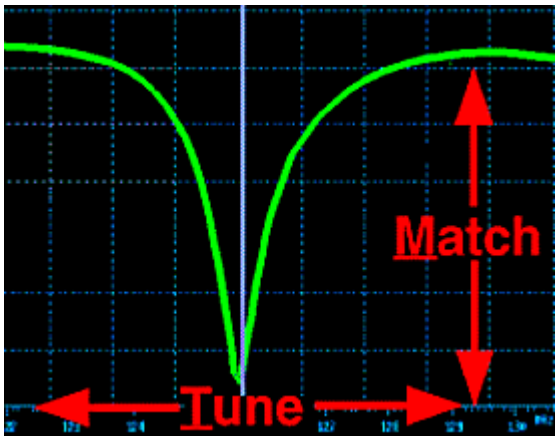

Figure 2.5 Tuning and matching for one frequency in the software

When the frequency is perfectly tuned and matched, which means the impedance is matching to 50 Ω, the green dip is in the center of frequency line (the solid vertical line) and will go down as far as it can.

Let's get back to the coil quality factor Q. It can be obtained by:

$$Q = \frac{Im[Z]}{Re[Z]} = \frac{stored\ energy}{dissipated\ energy} = \frac{\omega R}{L} = \frac{\omega}{3dB\ bandwidth}$$

Today, people always use double resonance probe (^{1}H and ^{13}C) and triple resonance probe (^{1}H, ^{13}C and ^{15}N) for research. There are many smart and excellent designs on those circuits [9-12].

2.2 Materials and Methods

2.2.1 Materials

Anthracene-9-carboxylic acid tert-butyl ester (9TBAE) powders were made with tert-butyl group ^{13}C labeled. Single crystals of 9TBAE were grown by using the slow evaporation method. 10 mg of 9TBAE was dissolved in 0.6 mL THF in a 5 mL glass vial, which was then placed in a larger glass vial with 6 mL methanol in the bottom. The larger glass vial is sealed and the THF diffuses into the methanol over the course of several days. After all the THF has partitioned into the methanol, single crystals of 9TBAE were collected from the bottom of the 5 mL vial. The single crystals with good sharp were chosen and wrapped by laboratory film which is light transparent. So the single crystals are protected and good to undergo UV exposure. Figure 2.6 shows the single crystal growing setup for 9TBAE.

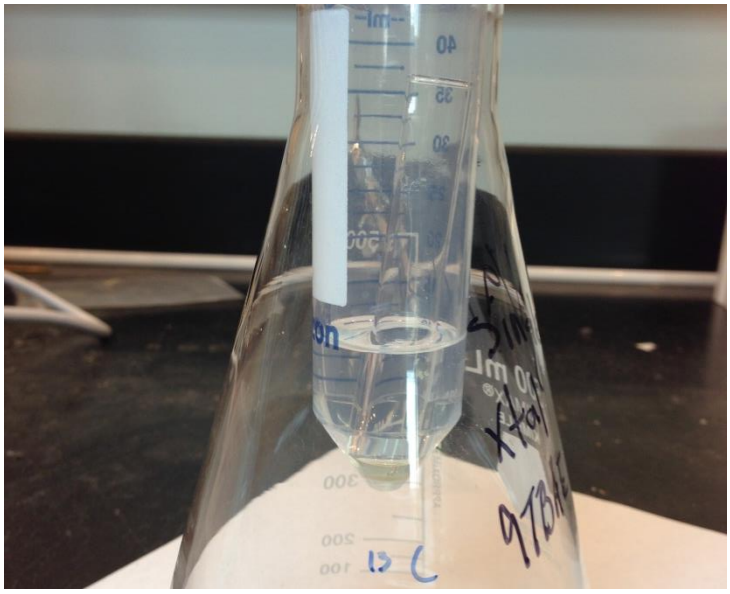

Figure 2.6 Single crystal growing setup for 9TBAE

2.2.2 Single-crystal Goniometer Probe

The single-crystal goniometer probe is a re-design and development of old goniometer probe with triple resonances. Figure 2.7a and 2.7b show the goniometer part and triple resonance circuit from the old probe.

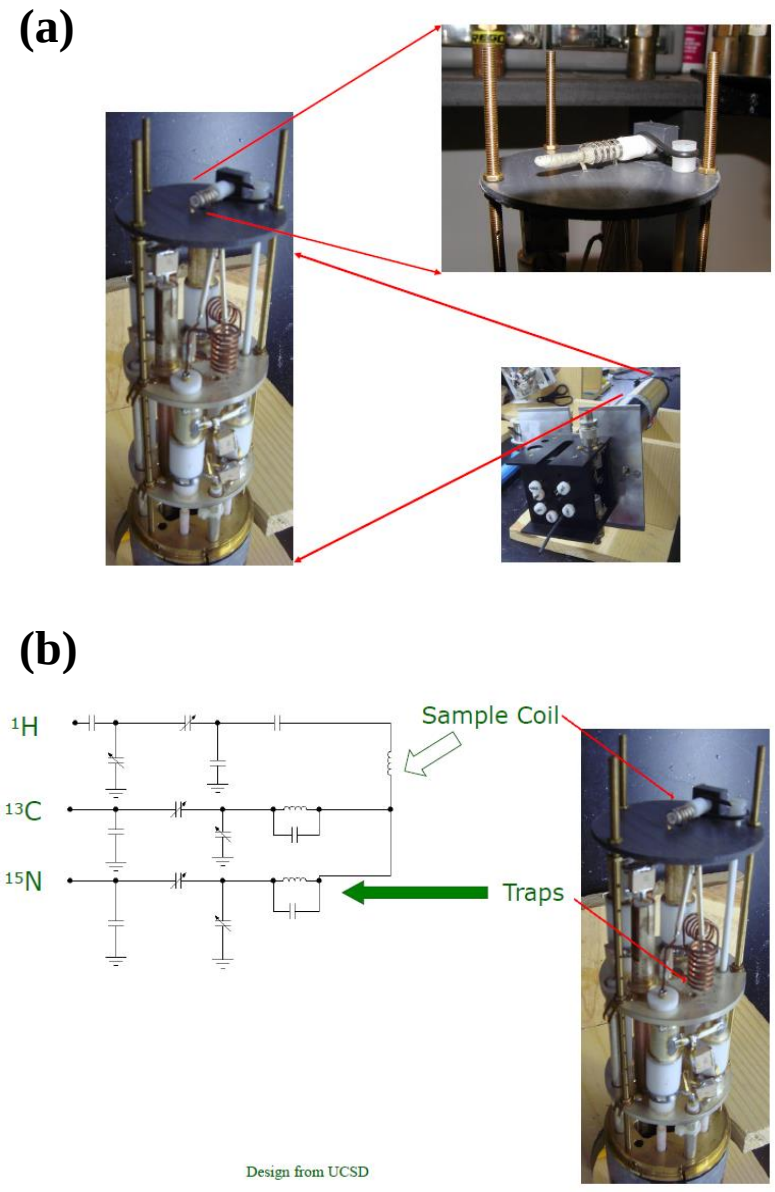

Figure 2.7 Old probe design (a) goniometer part (b) triple resonance circuits

The major problem of the old probe is the goniometer part only has one axis adjustment, which can rotate the sample tube along the center axis. So we made the new goniometer part with two axes adjustment in Figure 2.8.

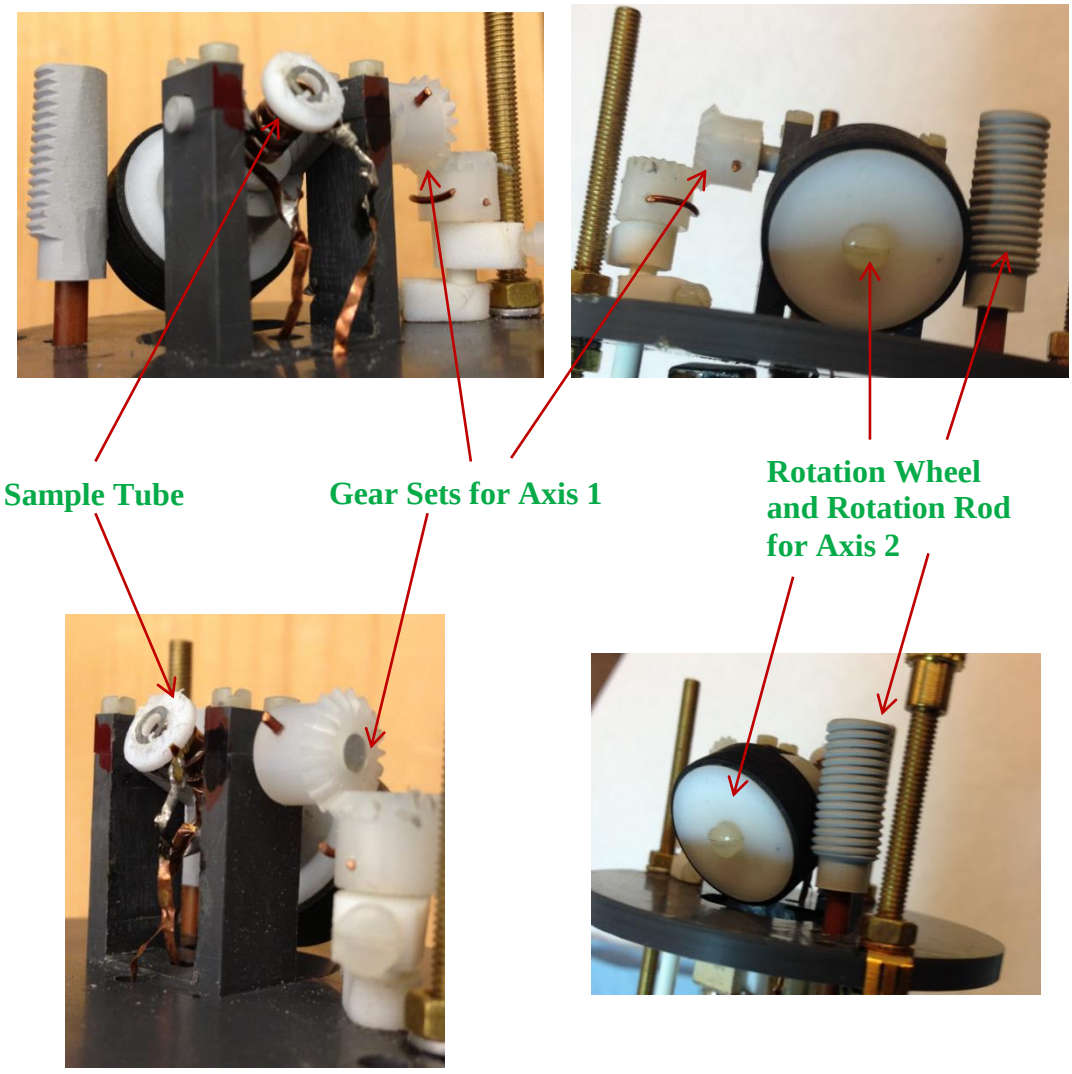

Figure 2.8 New design of goniometer part with two axes adjustment

With the gear sets for axis 1, the sample tube can be rotated like seesaw, up and down. With the rotation wheel and rod, the sample tube can rotate 360 ° along the center axis. The rod has two sides: flat side and circle side. When the flat side is facing to the wheel, the rod will not touch the rotation wheel. At this time, the gear set can be used to rotate along axis 1 and the rotation of axis 2 is off. When the circle side is facing the wheel, the rod is connected to the rotation wheel and the rotation of axis 2 is on. Because the axis 2 is connected to the sample tube only, rotating the wheel will not affect the axis rotation. The axis 1 and axis 2 are independent and convenient to rotate. Figure 2.9 shows those two axes in the goniometer part.

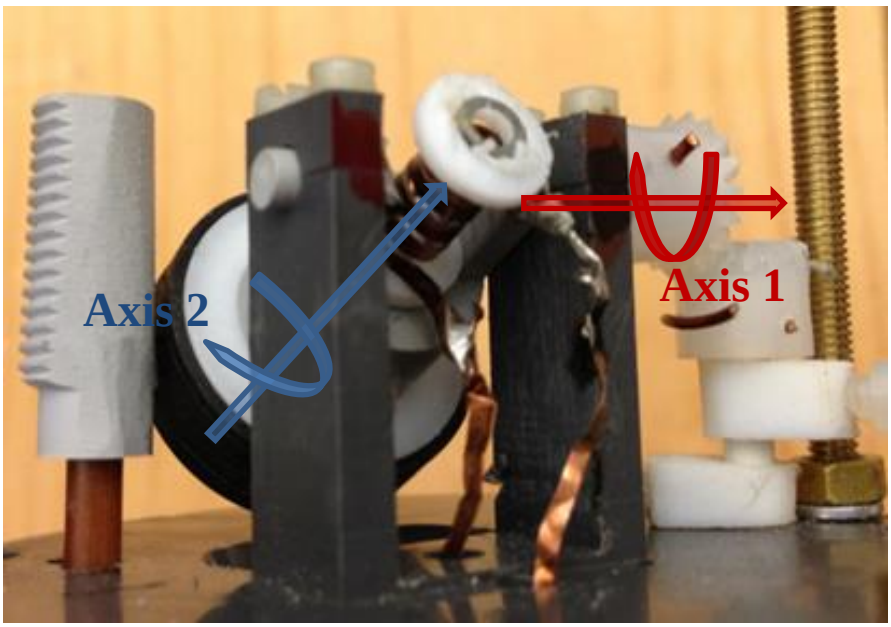

Figure 2.9 Axis 1 and 2 in goniometer part of the single-crystal probe

For the RF circuits, we removed the ^{15}N channel as it was not necessary for 9TBAE and the broken capacitors might have influence on other channel. All the bad capacitors were substituted with brand new capacitors and the lead materials were carefully chosen (Copper wire 99% Oxygen free). The coil material was chosen from the flat copper wire with 99% oxygen free. All the soldering was done by spot-welding method to eliminate the unnecessary capacitance and inductance.

The new single-crystal probe has two channels: ^{1}H and ^{13}C. Figure 2.10 shows the double resonance circuit for the new probe.

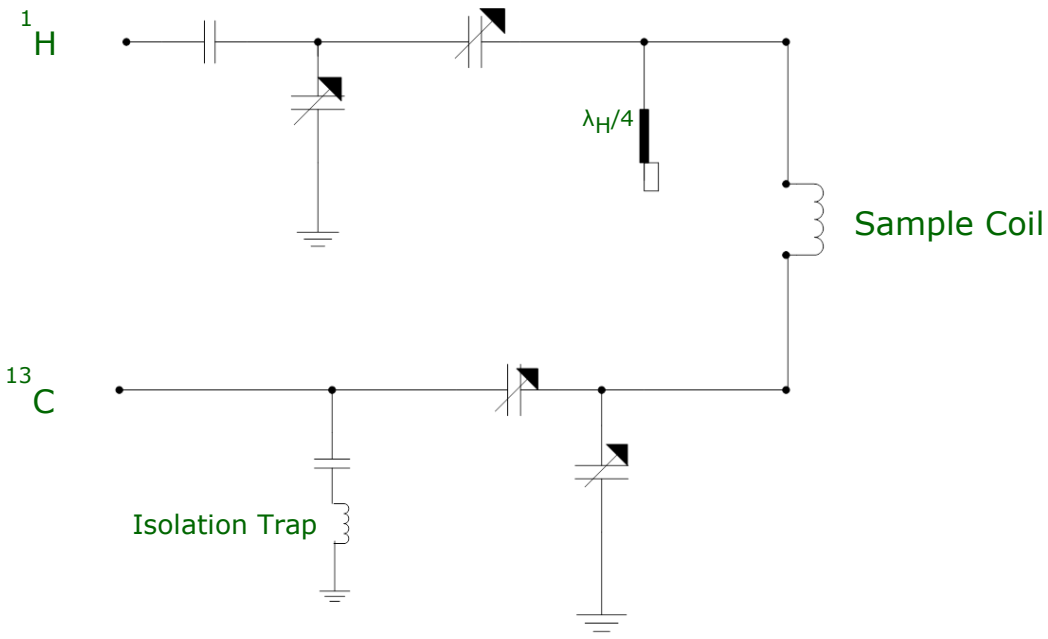

Figure 2.10 Double resonance circuit of the new single-crystal probe

The $\frac{\lambda_H}{4}$ transmission shunt was connected in the proton channel. The length of shunt was determined by the one quarter of wavelength at the particular magnetic field. For this probe, it was always used in 9.4 T spectrometer, where the proton frequency is 400 MHz. With some correction factor (0.75), the estimated length was approximately at 14 cm. The actual length was determined by the tune of ^{1}H channel. The main function of this $\frac{\lambda_H}{4}$ transmission shunt was to create virtual ground points on each side of coil for both ^{1}H and ^{13}C channels [9].

Some isolation trap circuit has been added in carbon channel to capture the proton signal. In the isolation trap, a capacitor (4.7 pF) was chosen to connect to a home-built inductor. Ground copper clips were carefully installed around the probe body.

Another challenge is the angle calibration of the rotation for the single-crystal probe. We were expecting to calibrate the angle of rotation inside the spectrometer and keep the experiment run in homogeneity. So we decided to use Hall Effect sensor to help us do the calibration. Based on the theory of Hall Effect, the Hall voltage will change if the angle between magnetic field and Hall Effect device plane changes. The Hall Effect sensor (HGCT-3020) and current power supply (120 Current Source) were purchased from Lakeshore Cryotronics (www.lakeshore.com). The Hall voltage was measured by 6 ½ digit multimeter (34401A) from Agilent. The connection between the Hall Effect sensor and those current or voltage meters was made by USB cable. Figure 2.11 shows the installation of the Hall Effect sensor on goniometer part of the probe.

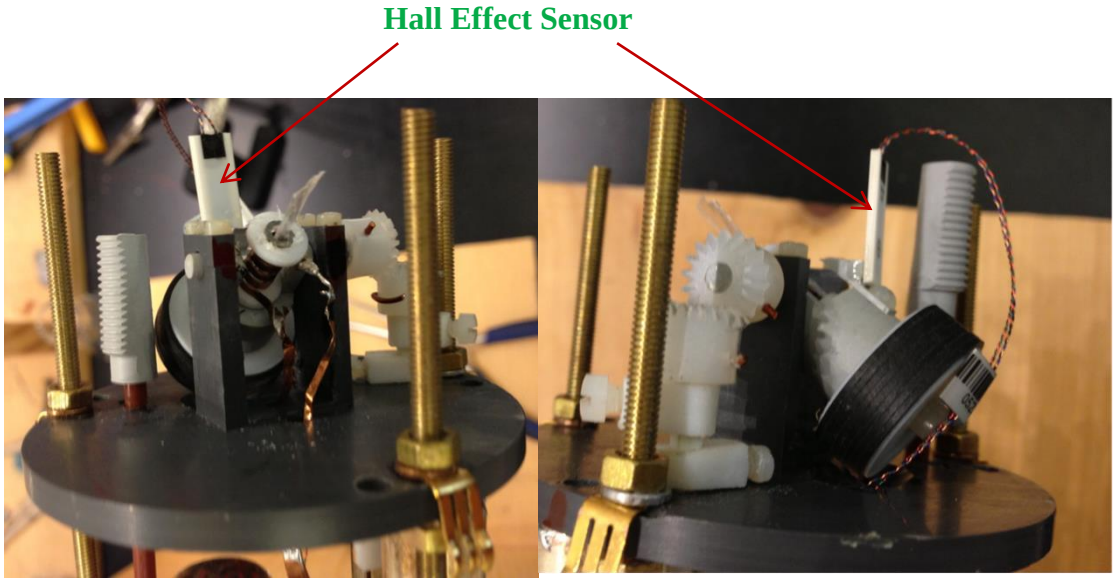

Figure 2.11 Installation of Hall Effect sensor on the single-crystal probe

The Hall voltage can be calculated by the following formula [13]:

$$V_{\mathrm{H}} \cong V_{\mathrm{H}}^{0} + \frac{I_c B}{q\rho d} \cos\beta_{\mathrm{HL}}$$

V^0_H is the offset voltage (< 100 μV), I_c=100 mA from the current supply, B=9.4 T, q is the charge on the current carriers, ρ is the density of charge carriers and d is the thickness of the Hall device plane. From the calculation, estimated value of $\frac{I_c B}{q\rho d}$ is between 0.9 and 1.7 mV. β_{HL} is the angle between the normal to Hall device plane and the magnetic field B. This Hall Effect sensor can only be used to measure the angle in Axis 1 since the Axis 1 angle is more important for the magic angle of NMR experiment.

The USB cable has four wires isolated inside so it is the perfect connecting cable for our Hall Effect sensor. Figure 2.12 shows the USB cable connections in details.

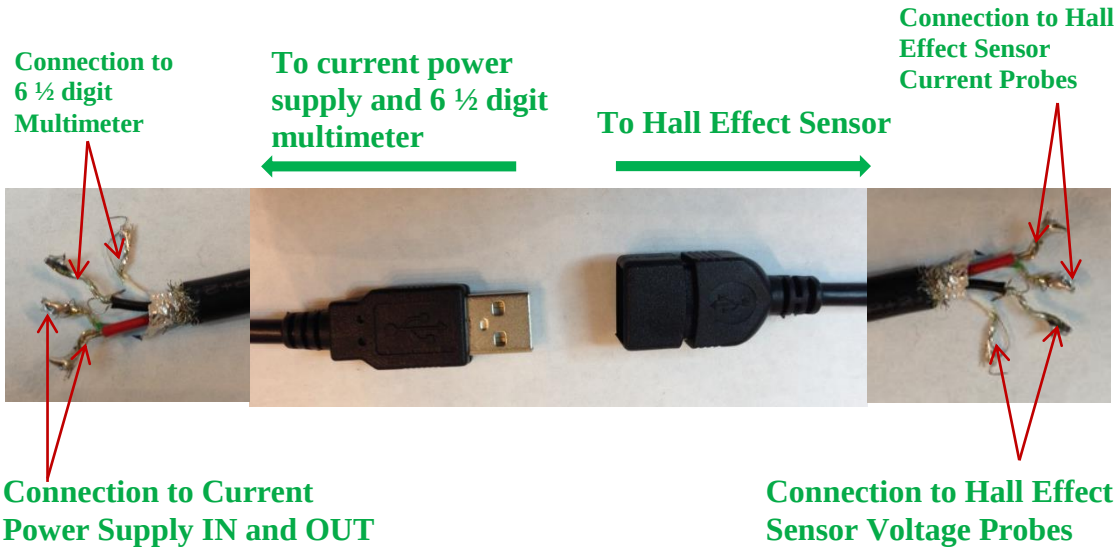

Figure 2.12 USB connections between Hall Effect Sensor to current power supply and 6 ½ digit multimeter

The whole single-crystal probe is done and the overview is showed in Figure 2.13 below.

Figure 2.13 Overview of the single-crystal probe (without ground shell)

2.2.3 ^{13}C Solid-state NMR

Cross-polarization (CP) solid-state NMR experiments were performed at 9.4 T (^{1}H frequency 400 MHz) on a Bruker AVANCE spectrometer equipped with home-built single-crystal probe. 83 kHz ^{1}H $\pi/2$ and decoupling pulses were used along with a 2 ms CP spin-lock. During CP the ^{13}C nutation rate was set to 40.5 kHz and the ^{1}H nutation rate ramped from 58–77 kHz. For each spectrum, 1024 complex data points with a dwell of 10 μs (spectral width 50 kHz, total acquisition time 10.29 ms) were acquired with a recycle delay of 3 s for a total experiment time of 51 min.

Double-quantum-filtered correlation spectroscopy (2QF COSY) [14] was also performed in the same spectrometer with the same probe. For 2D spectrum, 1024 complex data points for F2 channel and 128 complex data points for F1 with a dwell of 10 μs (spectral width 50 kHz for F2 and 16.7 KHz for F1, total acquisition time 10.29 ms for F2 and 3.84 ms for F1) were acquired with a recycle delay of 3 s for a total experiment time of 3 hour and 30 min. All the CP conditions are the same.

2.3 Results and Discussion

2.3.1 Probe Performance

With two axes adjustment, the single crystal sample's initial position is not that vital any more. The sample tube can be rotated by those two axes and the orientation of single crystal can be adjusted after it was put inside the sample tube.

The Hall Effect sensor did the angle calibration very well, corresponding to $\frac{I_c B}{q\rho d} = 1.5$ mV. With the help of angle calibration, we can easily find the angle which was at good orientation, even after we accidently changed the angle in Axis 1. In other words, the sample tube of probe can get back to its best position at any time, especial inside the NMR spectrometer. This benefit can save a lot of work on resetting the Axis 1 angle, such as finding the magic angle for some NMR experiments.

Table 2.1 and 2.2 show the probe performance of power deposition and coil quality factor Q.

Table 2.1 Nutation frequency and power deposition of the single-crystal probe

Channel	π/2 Pulse Length	Frequency	Power
^{1}H	3 μs	83KHz	200W
^{13}C	5 μs	50KHz	120W

Table 2.2 Coil quality factor Q of the single-crystal probe

Channel	Q
^{1}H	~134
^{13}C	~100

The power deposition performances for ^{1}H and ^{13}C channels are very good comparing to those commercial solid-state NMR probe. We did not try the upper limit of the power but those power depositions on the two channels were quite stable at least for 48 hour experiment.

Usually a good probe, the coil quality factor should be around 100 or more. The coil quality factors of ^{1}H and ^{13}C channels are both above 100 so we had a very reliable coil quality for our single-crystal probe.

Figure 2.14a and 2.14b show the resonance and isolation curve for ^{1}H and ^{13}C channels respectively. The resonance curves were deep and narrow for ^{1}H (400 MHz) and ^{13}C (100 MHz). The isolation is -49 dB for ^{1}H channel and -45 dB for ^{13}C channel. That means the isolation trap in the circuit works very well to remove the proton signal. Without the isolation trap part, the isolation drops to around -20 dB, which is not good enough for our NMR experiments.

(a)

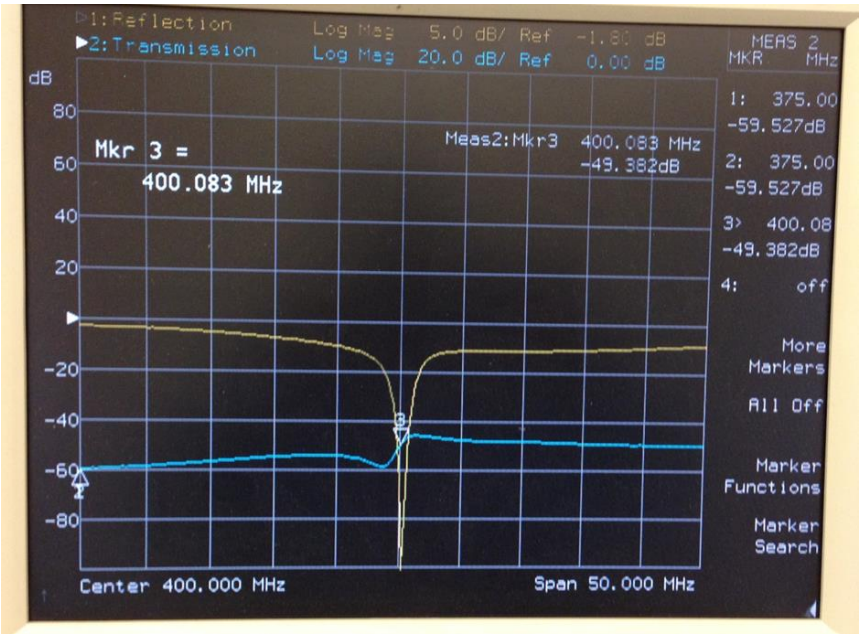

(b)

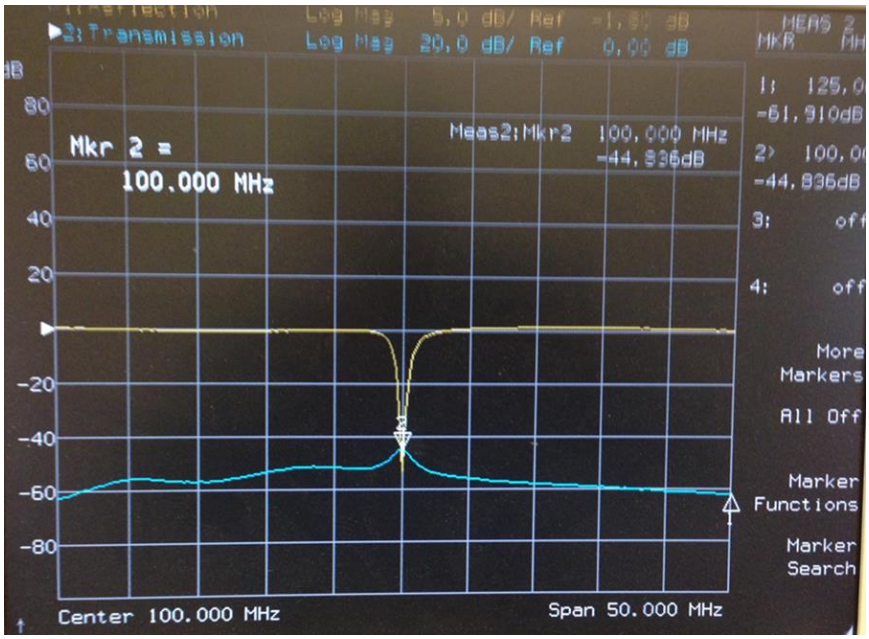

Figure 2.14 Resonance (yellow) and isolation (blue) curves for (a) ^{1}H channel; (b) ^{13}C channel

2.3.2 ^{13}C Solid-State NMR Experiment for 9TBAE Single Crystal

To investigate the rotation of ester sidegroups in 9TBAE, dipolar coupling term $\sim\frac{1-3cos^2(\theta)}{2}$ in NMR Hamiltonian is introduced and θ is the angle between the dipole and magnetic field. There are four monomer molecules of 9TBAE in one unit cell and they will form two dimer molecules after UV exposure. Two classes of ester sidegroups are present in one unit cell [7]. In each ester sidegroup, there is one butyl carbon with three methyl carbons rotating along the C=O axis. So all the dipolar couplings between butyl carbon and methyl carbons will project along the C=O axis. Then two classes of ester sidegroups form two classes of dipolar couplings between butyl carbon and methyl carbons. There is an angle between these two dipolar couplings (here dipolar coupling direction means the projected direction).

If the dipolar coupling is along the magic angle, as θ=54.7°, there is only one narrow peak (singlet) in ^{13}C spectrum because the dipolar coupling term in Hamiltonian is zero. Otherwise there is one quartet peak in ^{13}C spectrum since there are three butyl and methyl carbon dipolar couplings for each tert-butyl group.

In the discussion above, two classes of dipolar coupling are in the single crystal of 9TBAE. If one of them is along the magic angle and other one is along the magnetic field (to make the dipolar coupling Hamiltonian big), we will see one narrow singlet peak and one quartet peak in ^{13}C spectrum for each class of dipolar coupling. This orientation can help us follow the ester sidegroup rotation change when the photodimerization happens because it will have nice and separate two groups of butyl carbon peak in ^{13}C spectrum.

Those peaks will not overlap each other and make themselves clear to be recognized. This orientation is the one we need and we call it “good orientation”.

If those two dipolar couplings are along arbitrary axis, two quartet peaks will be seen in ^{13}C spectrum and at most of time they are overlapped. This orientation is useless for us to follow the ester sidegroup rotation change and we call it “bad orientation”.

Figure 2.15 shows the comparison of ^{13}C spectrum from the two orientations.

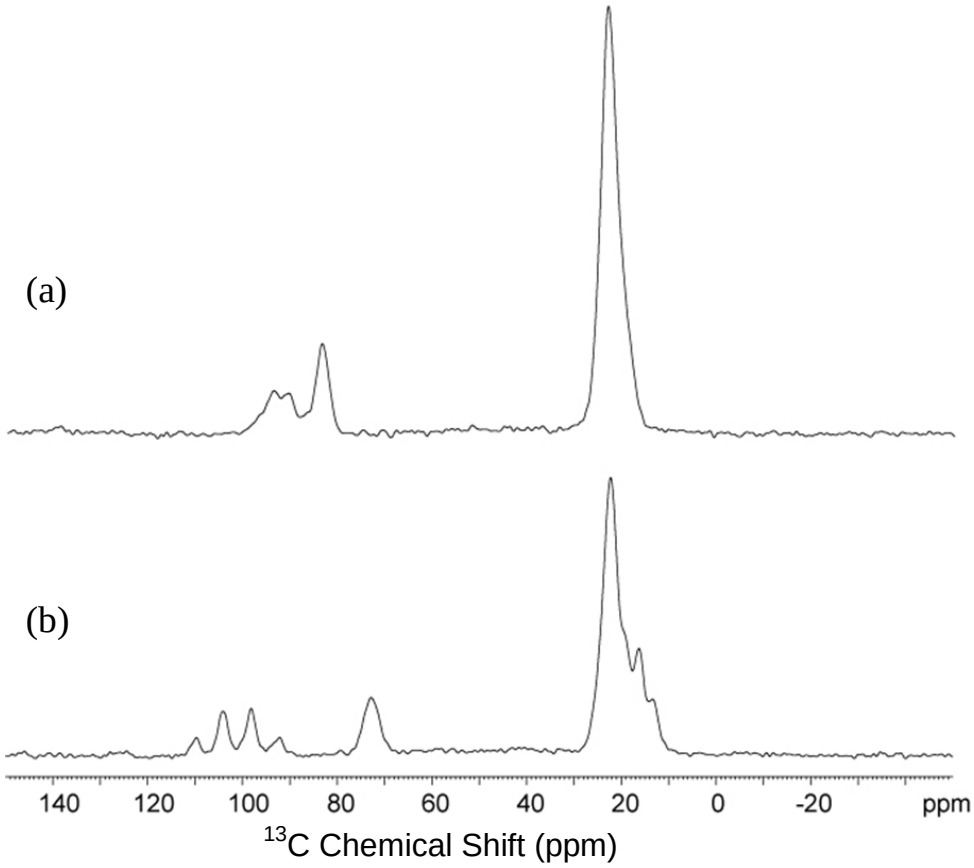

Figure 2.15 ^{13}C CP NMR spectra of single crystal of 9TBAE monomer
(a) bad orientation (b) good orientation

In Figure 2.15a, the bad orientation brings us one giant methyl peak in 20 ppm and some overlapped butyl peaks from 80 to 100 ppm. This spectrum can only provide little information of the ester sidegroup rotation. In the contrast, Figure 2.15b provides separate butyl peaks. The singlet peak at 72 ppm is from the dipolar coupling along the magic angle and the quartet peak at 100 ppm from the other dipolar coupling. They are distinguished easily besides the methyl peaks at 20 ppm. The intensity ratio of the quartet peak is 1:3:3:1, which is consistent with three dipolar couplings.

With the good orientation, we did 2D ^{13}C NMR experiment to check the correlation between the carbons, as showed in Figure 2.16.

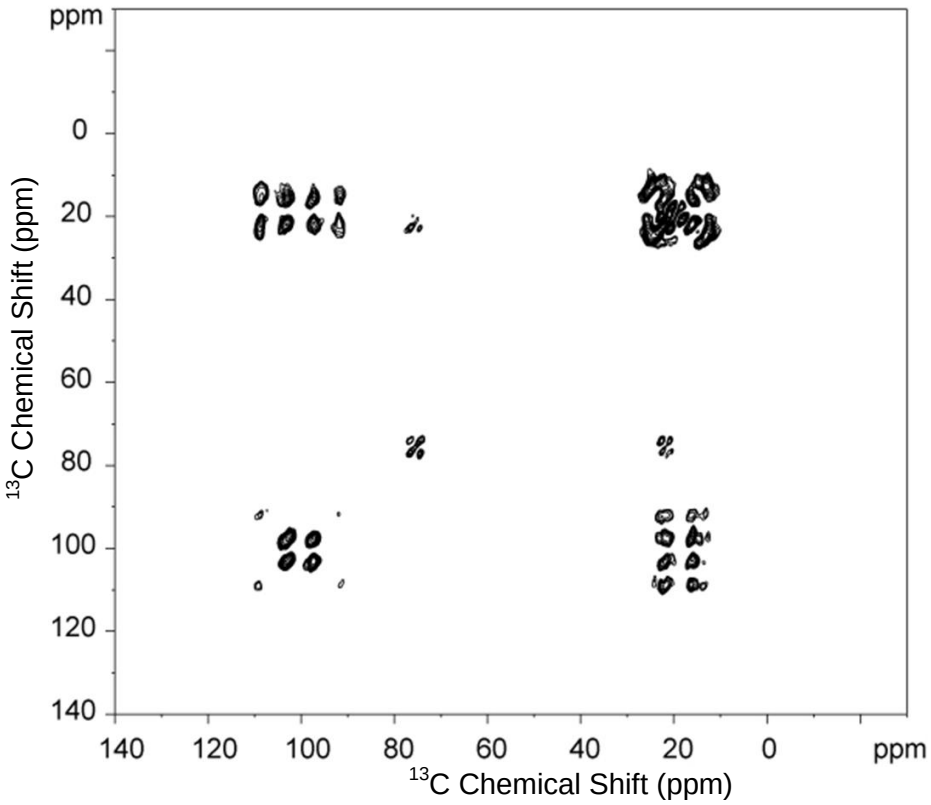

Figure 2.16 2QF COSY 2D spectrum of 9TBAE monomer single crystal

The 2QF COSY 2D spectrum gives us a direct view of the carbon correlations between the methyl carbons and butyl carbons. The cross peaks at (20 ppm, 100 ppm) and (20 ppm, 80 ppm) show that those two classes of butyl carbons respectively at 80 ppm and 100 ppm in Figure 2.15b have correlations with the methyl carbons surrounding them. The good orientation provides more information both in 1D and 2D spectrum, which could be useful for monitoring ester sidegroup rotation.

Series of ^{13}C CP spectra were done after various UV exposure times. UV exposure was done by using laser pointer irradiation directly into the sample tube. This time the benefits of Hall Effect sensor let us get back to the good orientation position very quickly and precisely. Figure 2.17 shows the ^{13}C CP spectra based on different UV exposure times.

After one hour UV light irradiation, the quartet peak at 100 ppm goes down and becomes broader. The singlet butyl carbon peak at 80 ppm shifts a little to 76ppm and becomes broader too. As the UV irradiation time goes longer, the quartet peak at 100 ppm is getting lower and broader. The singlet butyl carbon peak at 80 ppm shifts to 75 ppm and is becoming broader or two peaks overlapped. The methyl peaks at 20 ppm also becomes broader. However, all the chemical shifts of carbon peaks remain the same or just shift a little. The explanation for this is that the ester sidegroups does not rotate or rotate a little (<5°) when PRD or SSRD of 9TBAE is forming. In other words, the chemical environment surrounding those carbons does not change too much, which is reflected on the spectra in Figure 2.17. The peak broadening and shifting may be due to a small angle rotation for the ester sidegroup.

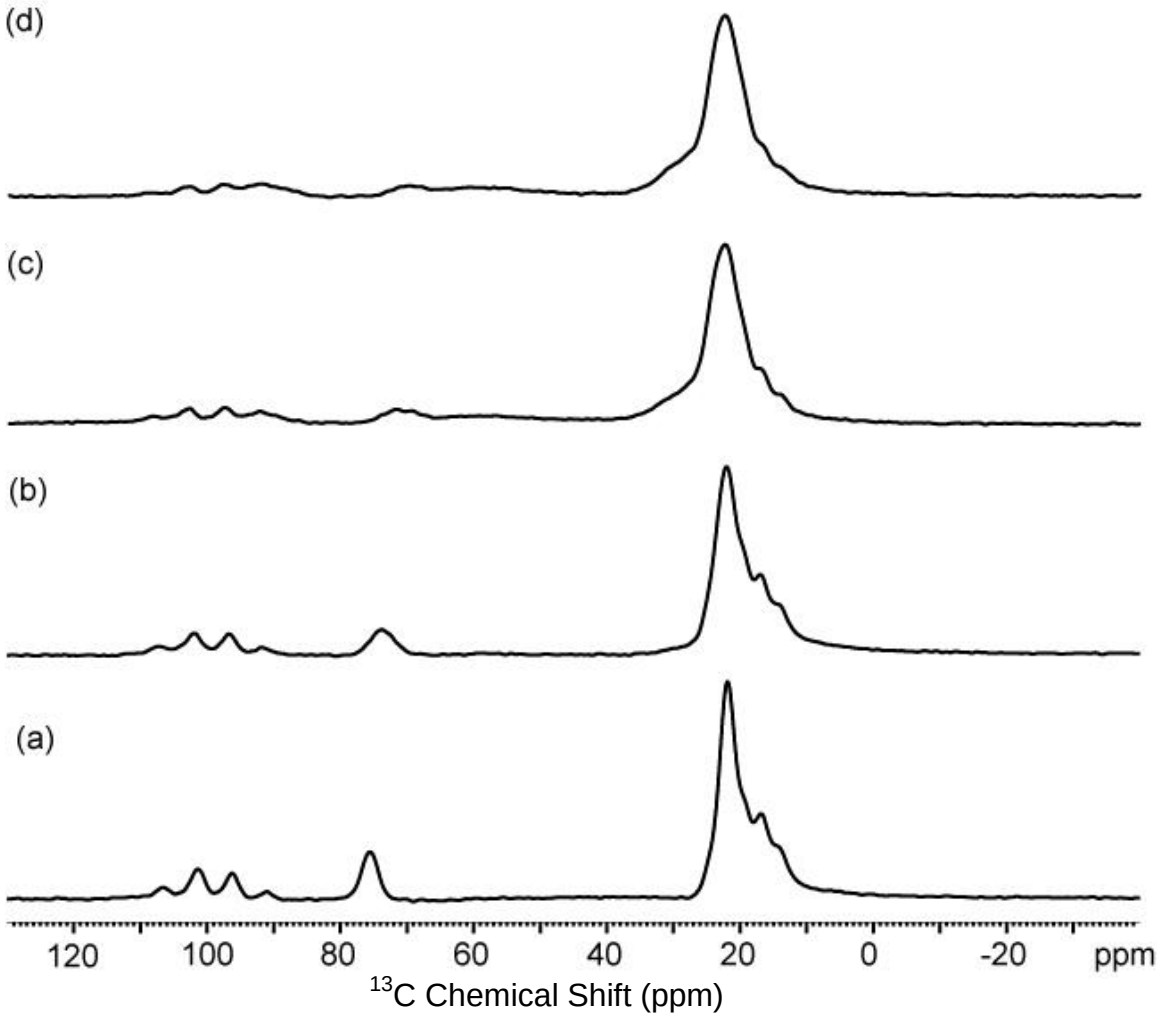

Figure 2.17 ^{13}C CP spectra of 9TBAE single crystal based on different UV exposure times (a) 0 min (b) 1 hour (c) 3 hours (d) 4.5 hours

Another interesting result is that we can get the direction of the other dipolar coupling (not along the magic angle) from the spitting gap of quartet peak. The splitting gap is around 500 Hz, C-C bond length is 1.512 Å and the projection angle of dipolar couplings is 78 °. From the formula of dipolar coupling Hamiltonian, the estimated angle θ is 0, which is along the magnetic field direction and makes the dipolar coupling term

big. This result is consistent with our expectation of the good orientation: Make one dipolar coupling along the magic angle direction to get rid of dipolar coupling term; Make the other one along the direction to maximize dipolar coupling term. This rough estimation can also be used to calculate the rotation angle in each step once the rotation is happening under the irradiation.

Overall, our results have confirmed that the ester sidegroups of 9TBAE are pointing inward when the PRD or SSRD is forming during the photodimerization. The good orientation can provide more useful information when doing the single crystal NMR experiments.

2.4 Conclusion

The single-crystal probe with two axes adjustment has the feature of two independent angle rotations for sample tube. The adjustment of goniometer part may lead to different orientations for the sample, especially for single crystal sample. This goniometer part may be very useful for a wide range of NMR single crystal experiments. The initial position of sample may not be the big issue for the experiment running since the orientation can be easily adjusted. The Hall Effect sensor provides the calibration of sample tube orientation and the Hall voltage is the reflection of the orientation to magnetic field. The Hall device brings the reproducible orientation adjustment with the provision of stable current source and high resolution voltmeter. The recovery of good orientation can be easily achieved by the angle calibration from the Hall device. Also the Hall device is independent component in the probe and can be uninstalled like LEGO bricks.

The detailed study of 9TBAE single crystal sample provides a deep understanding of molecular-level dynamics. We have used single crystal NMR measurements to conform that ester sidegroups are pointing inward when the PRD or SSRD of 9TBAE is forming. With detecting dipolar couplings of ^{13}C labeled tert-butyl group, monitoring of single crystal molecular movement is straightforward and easy. The ^{13}C spectrum can also provide more information, such as direction of molecular groups respect to the magnetic field. This method can be extended to study the photochemistry of other materials. The dipolar coupling in NMR experiment can be very useful for determining the single crystal orientation. With this novel single-crystal probe and method, predictive

understanding of solid-state photomechanical response becomes possible and orientation of the molecular groups can be estimated properly. It provides another pathway to study solid-state materials in single crystal structure.

2.5 Future Work

The single-crystal goniometer probe can be improved or developed in the following aspects:

(1) Improve the shielding and stability of the probe. The shielding of USB cable inside the probe may be another issue to improve since the current through the USB cable can create some small magnetic field.

(2) Second Hall Effect Sensor can be installed in the goniometer part to calibrate the angle of Axis 2. The challenge of this work is from the twisting of Hall device wires because the Axis 2 can be rotated by 360 °. One possible solution is to make the wires loose and long enough for the rotation.

(3) Laser photochemical reaction will be available inside the probe by installing laser fiber nearby the sample tube. Isolation and orientation of the laser fiber will be the main issue to solve.

References

1. Cohen, M. D. Angewandte Chemie International Edition 1975, 14, 386-393.

2. McBride, J. M.; Segmuller, B. E.; Hollingsworth, M. D.; Mills, D. E.; Weber, B. A. Science 1986, 234, 830-835.

3. MacGillivray, L. R.; Papaefstathiou, G. S.; Friscic, T.; Hamilton, T. D.; Bucar, D. K.; Chu, Q.; Varshney, D. B.; Georgiev, I. G. Accounts of Chemical Research 2008, 41, 280-291.

4. Koshima, H.; Ojima, N.; Uchimoto, H. Journal of the American Chemical Society 2009, 131, 6890-6891.

5. Naumov, P.; Kowalik, J.; Solntsev, K. M.; Baldridge, A.; Moon, J.-S.; Kranz, C.; Tolbert, L. M. Journal of the American Chemical Society 2010, 132, 5845-5857.

6. Al-Kaysi, R. O.; Muller, A. M.; Bardeen, C. J. Journal of the American Chemical Society 2006, 128, 15938-15939.

7. Zhu, L.; Agarwal, A.; Lai, J.; Mueller, L.J.; Bardeen, C.J. Journal of Materials Chemistry 2011, 21, 6258-6268.

8. Zilm, K. Tutorial Lecture for NMR probe in ENC 2011.

9. Cross, V.R.; Hester, R.K.; Waugh, J.S. Review of Scientific Instruments 1976, 47, 1486.

10. Doty, F.D.; Inners, R.R.; Ellis, P.D. Journal of Magnetic Resonance 1981, 43, 399-416.

11. McKay, R.A. USA Patent #4, 1984, 431, 446.

12. Schaefer, J.; McKay, R.A. USA Patent#5, 1999, 748, 861.

13. Mamone, S.; Dorsch, A.; Johannessen, O.G.; Naik, M.V.; Madhu, P.K.; Levitt, M.H. Journal of Magnetic Resonance 2008, 190, 135-141.

14. Piantini, U.; Sorensen, O.W.; Ernst, R.R. Journal of the American Chemical Society 1982, 104, 6800-6801.

Chapter 3

Studies of Photodimerization Reaction of 9-methylanthracene via Solid-State NMR

This chapter focuses on photodimerization and T1 measurement of 9-methylanthracene by ^{13}C solid-state NMR. The objective is to investigate the ^{1}H T1 relaxation curves for the monomer and the dimer based on various exposure times. A series of Solid-state NMR spectra provide the process of photodimerization based on various UV exposure times. The spin diffusion between the monomer and the dimer will provide characteristics of this two-spin system. A global fitting of spin diffusion model will be accomplished to determine the spin diffusion rate between the monomer and the dimer. It will contribute to understand the distribution of a dimer during the course of photodimerization.

3.1 Introduction

The solid state photodimerization was studied and developed by Schmidt [1], and indicated that the structure can be predicted by the feature of the crystal structure. So the molecular movement should be minimized. However, the photo-reaction is likely to occur in the defect if the transfer rate of light absorption is faster than the reaction rate. Then the molecular movements become available since there is enough room for that.

The photo-reaction will happen when 9-substituted anthracenes are under light irradiation. Two arrangements of 9-substituted monomers in a crystal lattice will form two different dimers: head-to-tail (trans) and head-to-head (cis), based on preparation methods [2-3]. For instance, the phtodimerization of 9-cyanoanthracene happens at the defects and molecular movements will make the dimer in different way. It can form both trans dimer and cis dimer.

In this chapter, we will use ^{13}C solid-state NMR to investigate the distribution of photodimerization of 9-methylanthracene (9-MA). The photo-reaction will happen when 9-methylanthracene is under light irradiation [4]. Figure 3.1 shows the {4+4} photodimerization of 9-MA from two monomers to trans dimer. The crystalline photodimer is stable at room temperature. The 9-MA system thus provides an opportunity to characterize crystals over the course of their photomechanical response, controlling the the fraction of reacted 9MA molecules by varying the duration of light exposure.

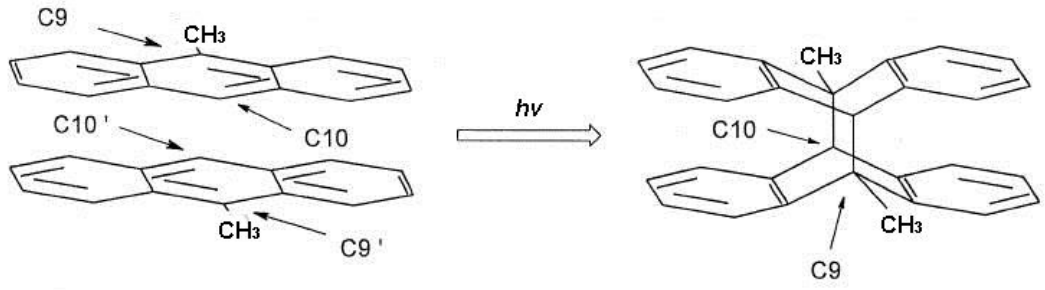

Figure 3.1 Photo-reaction scheme of 9-MA in head-to-tail dimer

^{13}C solid-state NMR has routinely been used to investigate the domain structure of mixture of different polymers [5]. By fitting ^{1}H spin-lattice relaxation decay T1, we can distinguish monomer and dimer peaks easily. Spin diffusion model was established to estimate the distribution of domain structure. Fittings were done simultaneously through all the samples with various UV exposure time. The ^{1}H spin-lattice relaxation can be used to estimate the domain size, which contributes to understand domain formation during the solid state photodimerization.

We also used ultra-fast magic-angle-spinning solid-state NMR ^{1}H experiments to enhance the understanding of photodimerization of 9-MA. Microneedles would show more efficient photodimerization process but the same photo-reaction during the UV exposure. Microneedles of 9-MA were studied by fluorescence microscope and SEM to investigate the mechanism of photochemical reaction.

This work demonstrates the heterometry mechanism in action for a prototypical photoreactive molecular crystal and provides fundamental insights for the design of photomechanical molecular crystal structures. Although 9-MA itself probably will not be

a practical photomechanical material due to its irreversibility, it is an ideal model system that illustrates how heterogeneous reaction kinetics and crystal size and shape can be used as design elements for the development of new photomechanical materials.

3.2 Materials and Methods

3.2.1 Materials

9-methylanthracene (9-MA) was purchased from Aldrich (99%) and used as received. All solvents used were analytically pure and were filtered before use to remove any dust particles that might act as nucleation sites. Materials were prepared in two different ways:

(1) Powders. 9-MA powder samples were powdered using a mortar and pestle and suspended in MilliQ water during their UV exposure. Or the powders were stirred in degassed water during the UV exposure and they show the same photoreaction result.

(2) Microneedles. These crystals were grown by the floating drop method. 1.1 mL of 9MA solution in hexanes with 1.9 mg/mL concentration and was slowly added onto the surface of MilliQ Millipore purified water in a Petri dish with 15 mm diameter. The Petri dish was covered with a glass plate and stored for 24-48 hours without being exposed to light. The 9-MA crystallized out as needle-shaped crystals on the surface of water. Microneedles were exposed in MillliQ water from the same radiation source (UV light).

All above samples were dried by schlenk lines and vacuum lines system.

3.2.2 Solid-state NMR experiments

Ultra-fast magic-angle-spinning solid-state NMR ^{1}H experiments were performed at 14.1T (^{1}H frequency 600 MHz) on a Bruker AVANCE spectrometer equipped with a triple-resonance 1.3 mm MAS probe, spinning at a MAS rate of 50 kHz. ^{1}H $\pi/2$ pulses were set to 83 kHz. For each spectrum, 4096 complex data points with a dwell of 5 μs (spectral width 100 kHz, total acquisition time 20.53 ms) were acquired with a recycle delay of 423 s for 2 scans.

Cross-polarization (CP) magic-angle-spinning (MAS) solid-state NMR experiments were performed at 14.1 T (^{1}H frequency 600 MHz) on a Bruker AVANCE spectrometer equipped with a double-resonance 4 mm MAS probe, spinning at a MAS rate of 10.5 kHz. 83 kHz ^{1}H $\pi/2$ and decoupling pulses were used along with a 2 ms CP spin-lock. During CP the ^{13}C nutation rate was set to 40.5 kHz and the ^{1}H nutation rate ramped from 58–77 kHz. For each spectrum (F2 channel), 2048 complex data points with a dwell of 10 μs (spectral width 50 kHz, total acquisition time 20.53 ms) were acquired.

^{1}H relaxation T1 was indirectly measured through ^{13}C by applying steady-state pulse sequence to ^{1}H prior to CP. T1 curves were obtained by using vdlist (variable delay list) experiment in Bruker Topspin 2.1. Vdlist experiment will repeat CPMAS experiment with steady-state sequence for a series of recycle delay times. The software treats the T1 experiment as a pseudo-2D experiment. The intensity of peaks versus delay times will provide the relaxation of T1. The variable delay list is {3, 4, 5, 7, 11, 15, 19, 27, 35, 67, 99, 131, 187, 259, 515, and 1027} in seconds.

All the experiments were performed at room temperature.

3.3 Results and Discussion

We used ultra-fast MAS solid-state NMR spectroscopy to monitor chemical changes for protons. In Figure 3.2a, we show the well-resolved ^{1}H spectrum of the monomer before irradiation. After irradiation, Figure 3.2b and 3.2c show a steady decrease in the areas of the monomer protons at chemical shifts about 4 ppm, with simultaneous growth of the dimer peaks clustered around 2 ppm, which are from C10. In Figure 3.2c, the monomer peak is hardly to see because it overlaps another small peak at around 6 ppm. The giant peak at 9 ppm is for those protons in aromatic ring. The loss of intensity for the monomer protons at 4 ppm and the appearance of a new proton peak at 2 ppm reflect the different chemical environments of the two C10 through the photodimerization. The ultra-fast MAS condition significantly averaging the ^{1}H-^{1}H homonuclear dipolar coupling can provide us well-resolved ^{1}H resonances in solid materials. The ^{1}H peaks are well resolved and clear enough to recognize.

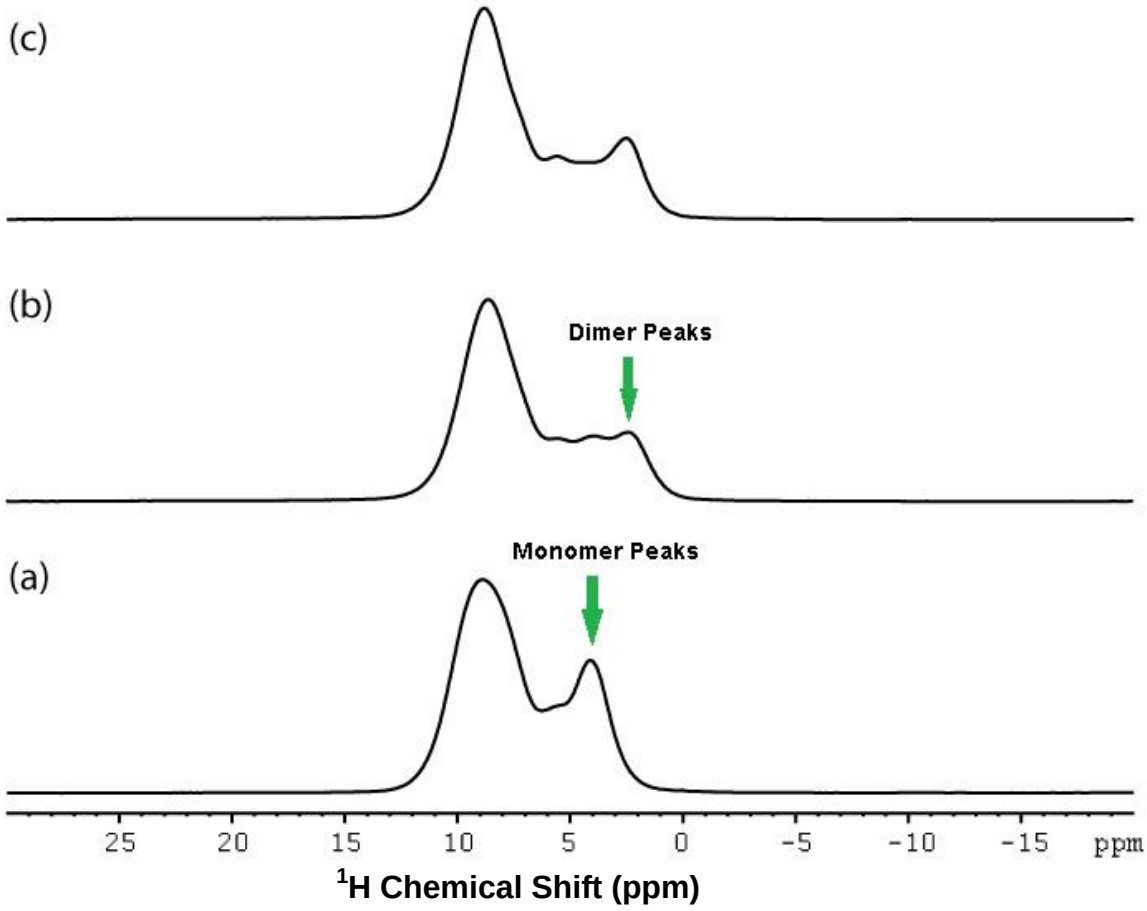

Figure 3.2 ^{1}H solid-state NMR data of 9-MA powder (a) before exposure to UV, (b) after 30 min of UV exposure, and (c) after 60 min of UV exposure. 9-MA monomer and dimer peaks are shown in the insets. Formation of the dimer is characterized by the appearance of dimer peaks at 2 ppm and the decrease of the monomer peaks at 4 ppm.

However, we did not try to fit the T1 curves from the ^{1}H spectra because some residue H_2O may exist in the sample and those ^{1}H may also have a coupling with ^{1}H in 9-MA, which could give us inaccurate T1 values.

So we used indirect measurement of ^{1}H T1 curves from the methyl ^{13}C peak of the monomer at 16 ppm and the dimer at 28 ppm. To confirm photodimerization of the 9-MA molecules, we used ^{13}C solid-state NMR spectroscopy to monitor chemical changes

for individual carbons. In Figure 3.3a, we show the well-resolved ^{13}C spectrum of the monomer before photo-irradiation, consistent with a well-ordered molecular crystal. After photo-irradiation, Figure 3.3b and 3.3c show a steady decrease in the areas of the methyl carbons at chemical shifts 16 ppm, with simultaneous growth of the methyl dimer peaks clustered around 28 ppm. Also, the experiments showed that the new peaks at 53.5 ppm and 68 ppm are assigned respectively to the nonprotonated bridge-head carbons (C9 in Figure 3.1) and the protonated bridge-head carbons (C10 in Figure 3.1). The overlapped aromatic carbon peaks are around 130 ppm while the peaks around 148 ppm are due to nonprotonated aromatic carbons. The loss of intensity in the aromatic region (125-135 ppm) is accompanied by the appearance of new bridge-head carbon peaks at 53.5 and 68 ppm and new nonprotonated carbons of the two outer benzenes left behind. Some interesting feature of the ^{13}C spectra is broadening and shifting of the methyl peaks as the reaction progresses, which is due to a distribution of microscopic environments giving rise to varying chemical shifts. Those two new bridge-head carbon peaks proved that the photodimerization is progressing in the head to tail way and the arrangement of monomers is in antiparallel way. The solid-state NMR data shows that the 9-MA solid-state photodimerization does form a new crystal phase, which is coincidence with the Figure 3.2.

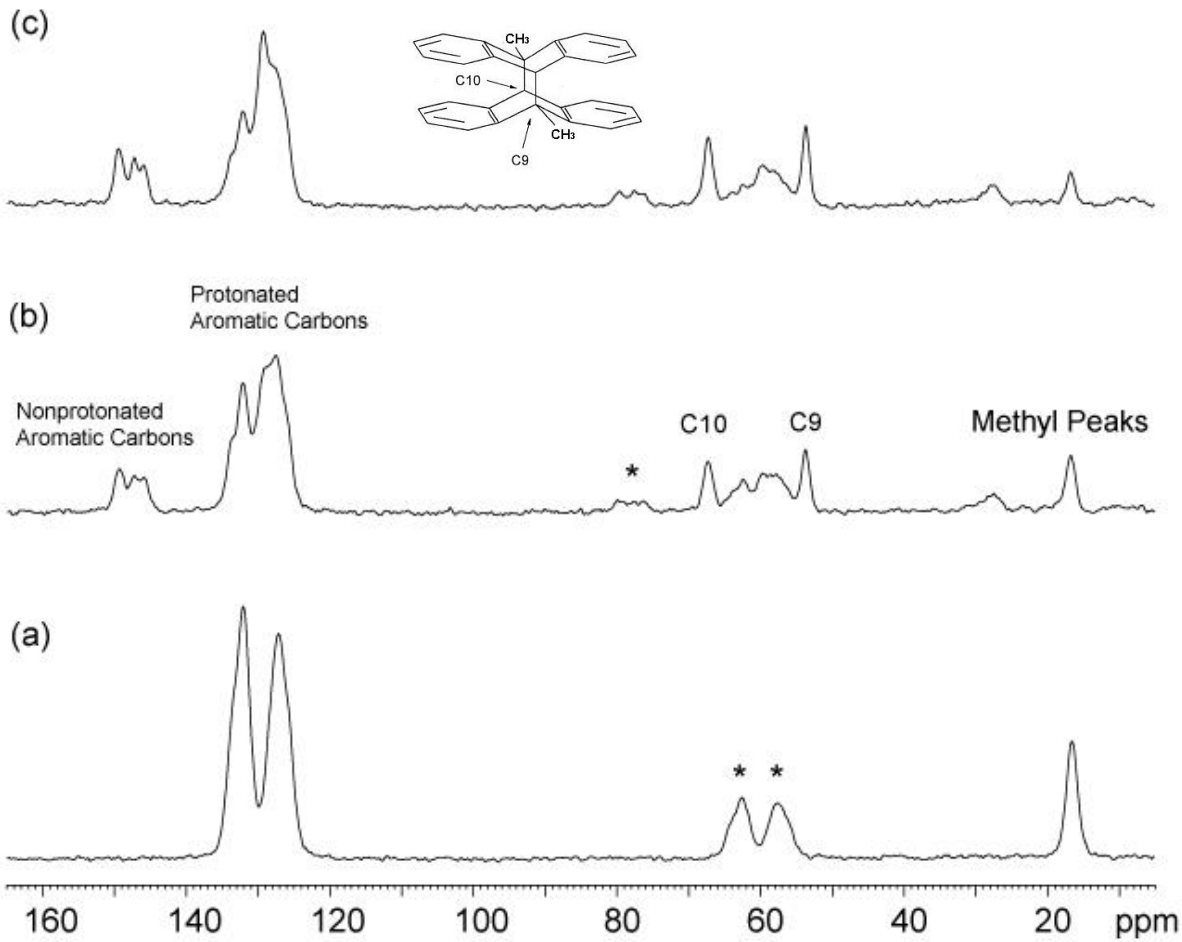

Figure 3.3 ^{13}C solid-state NMR data of 9-MA powder (a) before exposure to UV, (b) after 30 min of UV exposure, and (c) after 60 min of UV exposure. Carbon numbering of 9-MA monomer and dimer are shown in the insets. Formation of the dimer is characterized by the appearance of bridge-head carbon resonances at 53.5 ppm and 68 ppm. The nonprotonated aromatic carbon peaks around 148 ppm are other notable sign of dimer. Spinning sidebands are marked with asterisks.

We used Mathematica 8.0 for fitting the carbon peak intensity in the spectra (see codes in Appendix). With the intensity and delay time data, ^{1}H T1 decay curves are measured indirectly from ^{13}C resonances for 9-MA pure monomer. A single exponential decay curve of the 9-MA pure monomer was observed in Figure 3.4, with T1 of 139.5 s fitting in Mathematica 8.0 (see codes in Appendix). We used the methyl peak at 16 ppm as the monomer peak fitting.

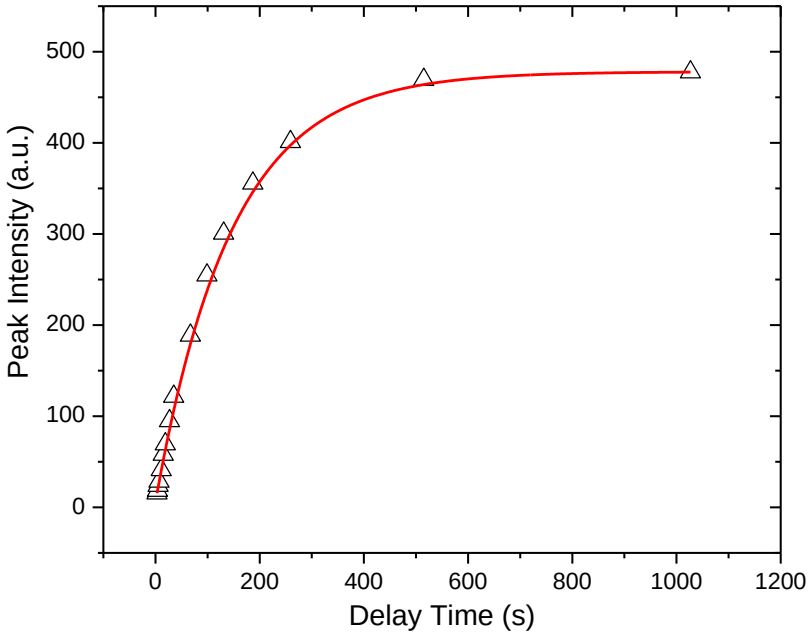

Figure 3.4 ^{1}H T1 decay curve of 9-MA pure monomer (Δ) has T1 of 139.5 s. The red line is the single exponential fitting line.

The single exponential fitting equation is indicated below:

$I = I_0(1 - e^{-\frac{t}{T_1}})$; I is the peak intensity.

Then we kept using the methyl peak at 16 ppm as the monomer peak in 9-MA samples with UV exposure while we used the protonated bridge-head carbons at 68 ppm as the dimer peak. T1 curves of monomer and dimer peaks for the 30 min UV exposure 9-MA sample are showed in Figure 3.5a and 3.5b.

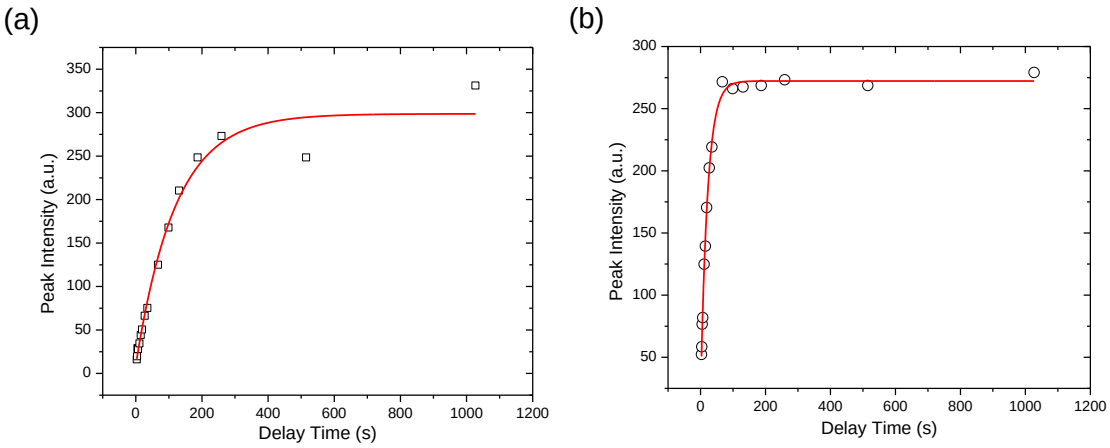

Figure 3.5 ^{1}H T1 decay curves of 9-MA monomer sample with 30 min UV exposure: (a) monomer T1 curve (□) and (b) dimer T1 curve (○). The red line is the single exponential fitting line.

The fraction of the monomer (f_M) in each sample is obtained by using the methyl carbon peaks conversion. The monomer peaks and dimer peaks used in formula are respectively at 16 ppm and 28 ppm.

$$f_M = \frac{Methyl\ Peak\ Intensity\ from\ Monomer\ Peaks}{Methyl\ Peak\ Intensity\ from\ Both\ Monomer\ Peaks\ and\ Dimer\ Peaks}$$

Table 3.1 shows more 9-MA samples with various UV exposure times. T1 of monomer peaks and dimer peaks are different based on different UV exposure times.

Table 3.1 T1 and f_M of 9-MA samples with various UV exposure time

UV Exposure Time (min)	T1 of Monomer Peaks (s)	T1 of Dimer Peaks (s)	Monomer Fraction f_M
0	139.5	N/A	1.00
15	142.9	9.2	0.69
30	109.9	18.9	0.58
45	139.9	14.8	0.54
60	107.9	22.0	0.41
240	122.3	17.2	0.38

In 9-MA crystal, there is always some monomer bulk not reacted by the UV irradiation because the outside 9-MA crystal may block the light absorption. So for the 240 min sample, it still has some residual amount of monomer peaks.

The T1 value is slightly different because the monomer and the dimer are microscopically mixed well. So the spin diffusion may take place between the monomer and the dimer. To investigate the spin diffusion effect, a spin diffusion equation describing a two-domain model should be introduced below [4]:

$$-\frac{d}{dt}\begin{pmatrix} I_M \\ I_D \end{pmatrix} = \begin{pmatrix} \frac{1}{T_{1M}} + (1-f_M)K & -f_M K \\ -(1-f_M)K & \frac{1}{T_{1D}} + f_M K \end{pmatrix}\begin{pmatrix} I_M - I_M^0 \\ I_D - I_D^0 \end{pmatrix}$$

I_M and I_D are the intensities for the monomer and the dimer while I^0_M and I^0_D are the equilibrium intensities. T_{1M} and T_{1D} are the T1 values of pure monomer and dimer. K

is the spin diffusion rate and f_M is the fraction of the monomer calculated by the methyl carbon peaks conversion ratio.

A global fitting is done by solving the spin diffusion model and minimizing κ^2 value for all the samples (see codes in Appendix). We used T_{1M}=139.5 s from pure monomer sample and f_M from Table 3.1. From the fitting result, we got T_{1D}=15.8 s shared for all the samples. The spin diffusion rate K is obtained individually according to each f_M, showed in Table 3.2.

Table 3.2 Spin diffusion rate of 9-MA samples with various UV exposure time

UV Exposure Time (min)	K (s^{-1})
0	N/A
15	4.0×10^{-11}
30	0.01
45	7.7×10^{-11}
60	0.005
240	0.002

The fitting graphs are showed in Figure 3.6 for each sample and the global fitting seemed very well fitted with the experimental data points.

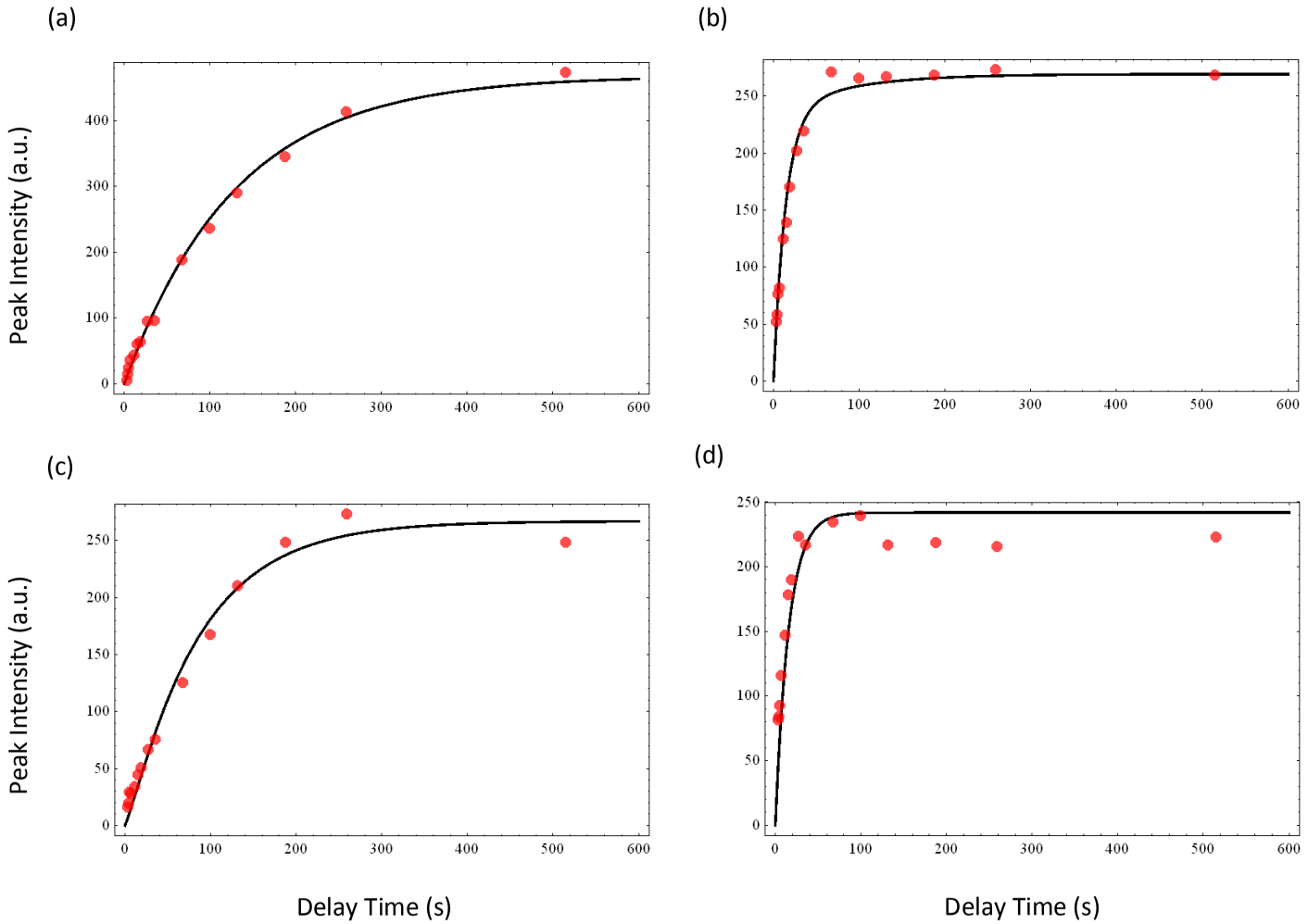
(a)
(b)
(c)
(d)
Peak Intensity (a.u.)
Peak Intensity (a.u.)
Delay Time (s)
Delay Time (s)

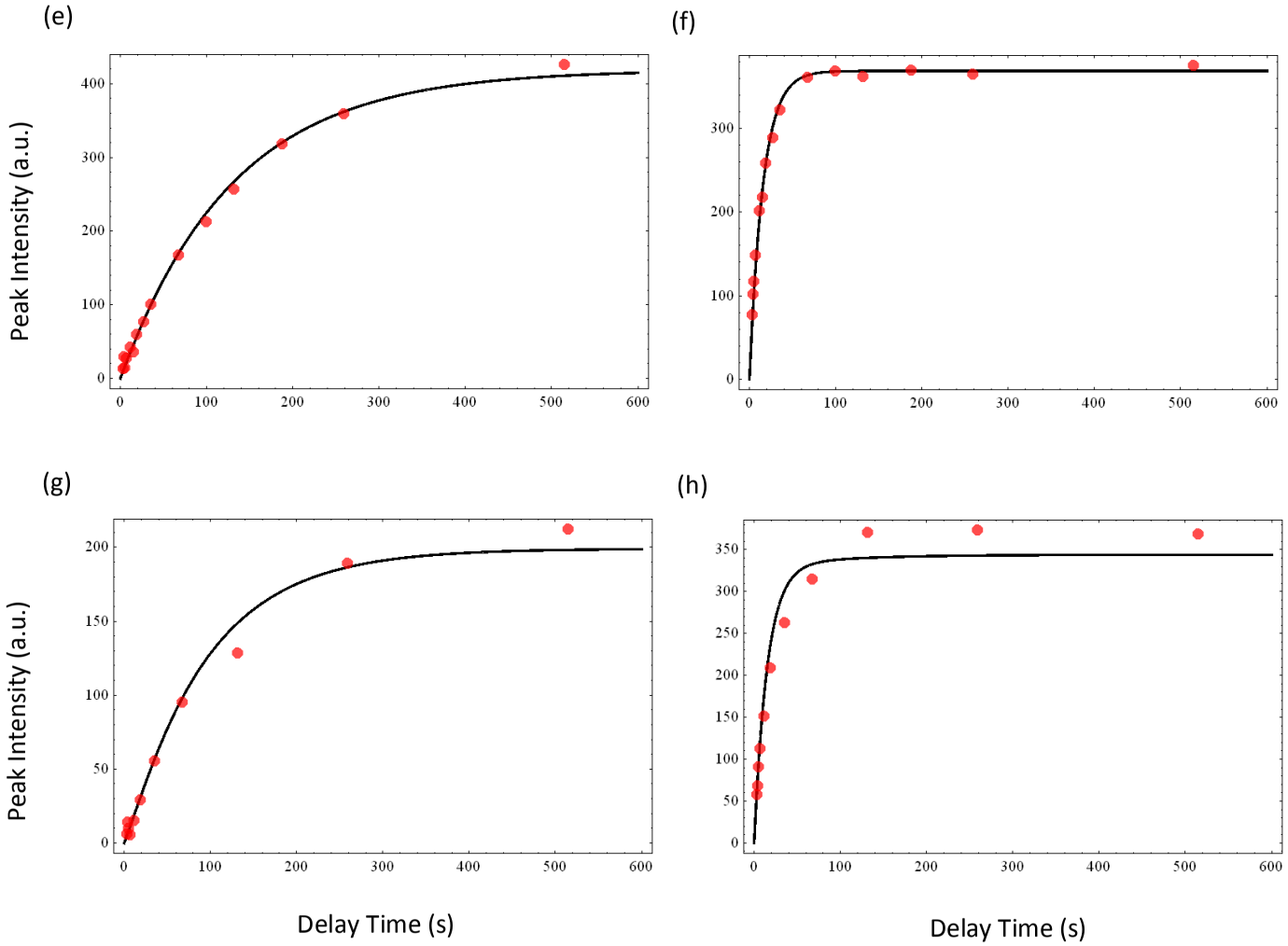
(e)
(f)
(g)
(h)
Peak Intensity (a.u.)
Peak Intensity (a.u.)
Delay Time (s)
Delay Time (s)

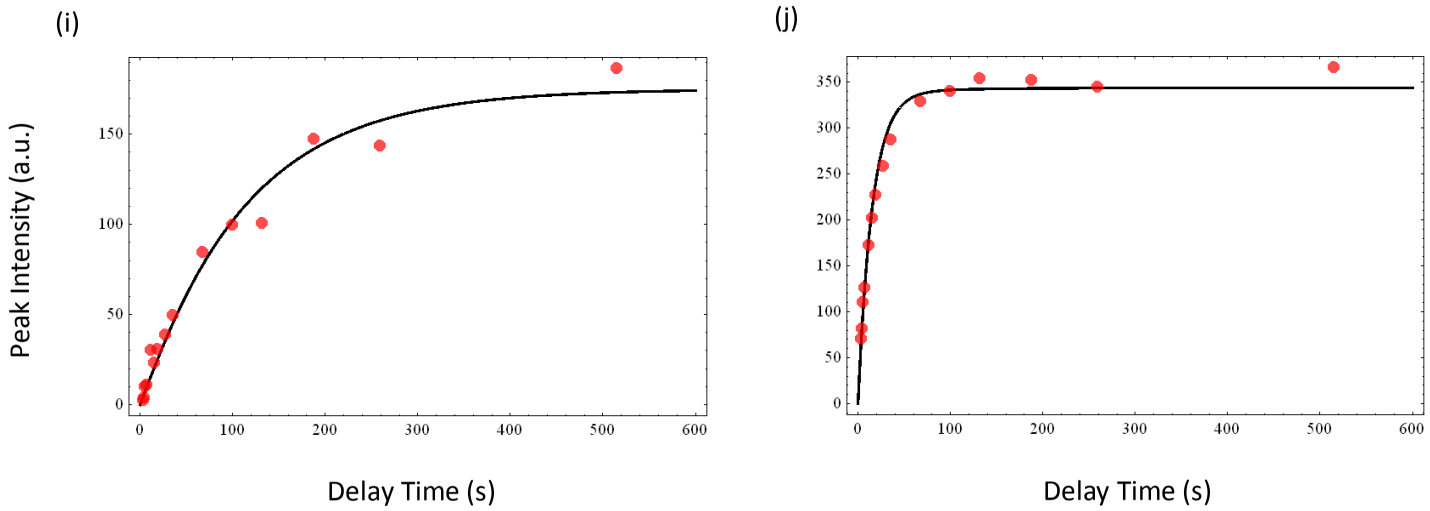

Figure 3.6 Global fitting curves on ^{1}H decay curves: (a) monomer fitting curve for 15 min UV exposure sample, (b) dimer fitting curve for 15 min UV exposure sample, (c) monomer fitting curve for 30 min UV exposure sample, (d) dimer fitting curve for 30 min UV exposure sample, (e) monomer fitting curve for 45 min UV exposure sample, (f) dimer fitting curve for 45 min UV exposure sample, (g) monomer fitting curve for 60 min UV exposure sample, (h) dimer fitting curve for 60 min UV exposure sample, (i) monomer fitting curve for 240 min UV exposure sample, and (j) dimer fitting curve for 240 min UV exposure sample. The red points are the experimental data and the black solid line is the fitting curves.

The spin diffusion rates from the global fitting are quite small. To reexamine the K values, we solved the spin diffusion model, exhibited some curve with limited K values and compared those curve with ^{1}H T1 relaxation curves from our experiments. The comparisons of the monomer peaks are indicated in Figure 3.7 and the peak intensity has been normalized.

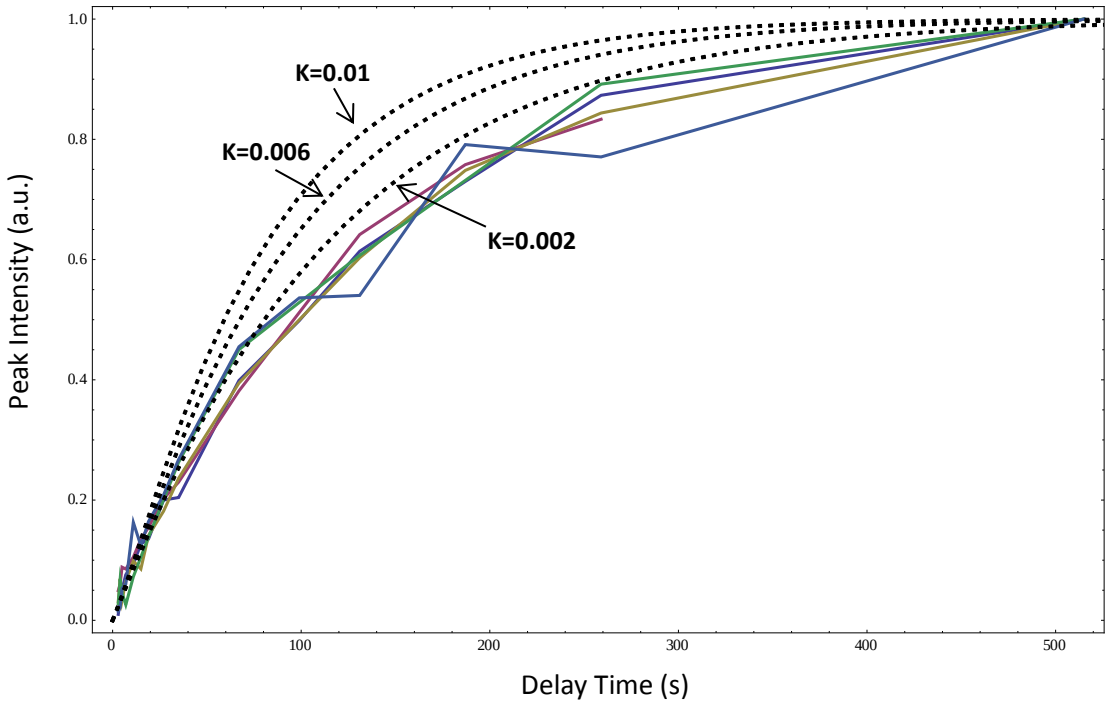

Figure 3.7 Experimental data points of monomer peaks are compared with spin diffusion model for various K values. The colorful solid lines are the experimental data points and the black dashed lines (K=0.002, 0.006, 0.01 s^{-1}, from bottom to top) are from the spin diffusion model.

Besides comparing with the monomer peaks, we did the same work on the dimer peaks in Figure 3.8. The dimer component fitting equation varied little based on different K values.

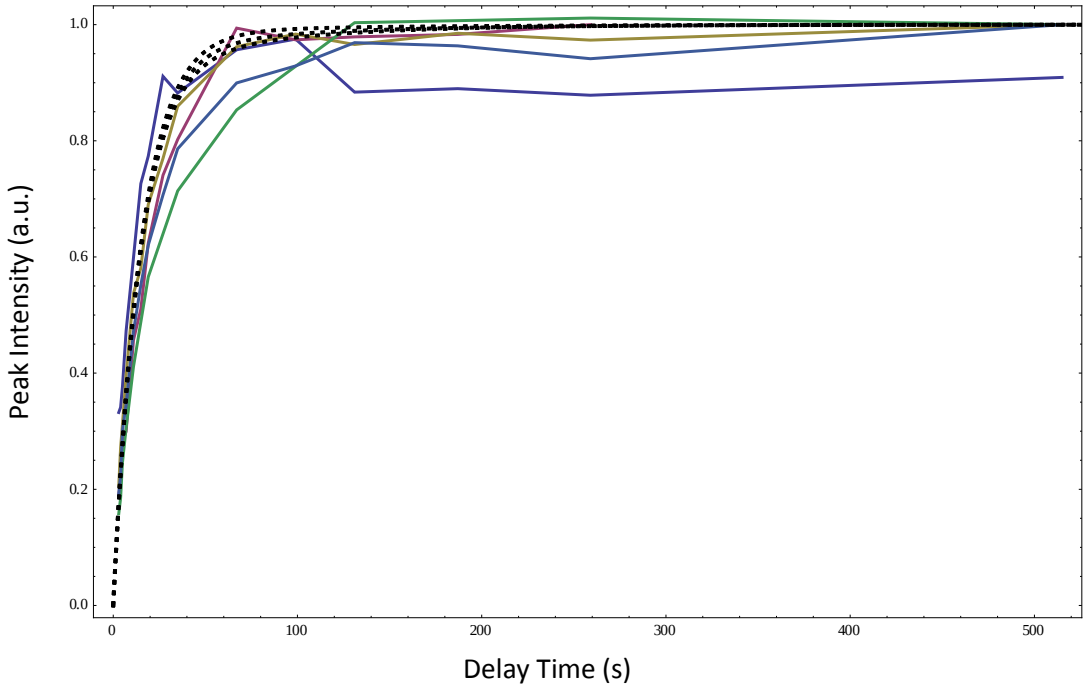

Figure 3.8 Experimental data points of dimer peaks are compared with spin diffusion model for various K values. The colorful solid lines are the experimental data points and the black dashed lines (K=0.002, 0.006, 0.01 s^{-1}, from bottom to top) are from the spin diffusion model.

By doing those comparisons and the global fitting, these experiments set an upper limit for the spin diffusion rate K between domains of $K \leq 2x10^{-3}$ s^{-1}. The inverse of this rate gives a value for $\tau \geq 500$ s for the average time for a spin to traverse a domain. We estimate the spin diffusion coefficient *D* [6] within a domain using

$$D = \frac{2r_0^2}{T_2} \qquad (1)$$

where r_0 is the proton Van der Waals radius (r_0= 0.117 nm), and T_2 is the spin-spin relaxation time, measured to be 80 μs in both the monomer and dimer from the ^1H

linewidths. Assuming isotropic diffusion in three dimensions, the average distance covered by the spin during this period is given by

$$R_{domain} = \sqrt{6D\tau} \quad (2)$$

From Equation (2), we estimate R_{domain} to be on the order of 1000 nm, even at the lowest conversion fraction (10%) studied. This was somewhat surprising given that Terao and coworkers had resolved changes in K from their T_1 data that suggested smaller domains whose size increased ruing the course of the reaction [4]. We can only surmise that differences in sample preparation and/or irradiation conditions may account for the discrepancy in T1 data, since the NMR conditions were very similar. In any case, although the estimate of domain size is fairly rough and involves significant assumptions, the lack of spin exchange in our data indicates the formation of large dimer domains at very early times in our samples.

^{13}C solid-state NMR experiments were also performed on the microneedles of 9-MA. All the photodimerization progress is the same. Under 1 min and 5 min UV exposure time, the monomer conversion fractions are 10% and 45% respectively. This fast photoresponsible reaction of 9-MA microneedles is the benefit from thin laying and small crystal distribution during the UV irradiation. The spin diffusion rate K is also very small, at 10^{-8} s^{-1} scale.

With the fluorescence microscope, PXRD and SEM data, we observed that the needles undergo a bending motion during irradiation, but then return to their original shape as time goes on. And the two most observations are 1) the type of photomechanical deformation depends on the shape of the crystal, even when the crystal orientation and

packing are identical, and 2) the deformation is maximized at intermediate stages during the photoreaction, and at the endpoint the crystal has returned to its original shape.

Mechanism for the deformation is the generation of strain energy between two different solid-state domains. In a sense, this is the same concept as generating a bimorph layer by illuminating one side of a thick crystal. The difference is that for our very small crystals, the spatial domains spontaneously form as a result of the intrinsic solid-state reaction dynamics, rather than as the result of special illumination conditions. Of course, in the case of 9-MA the motion depends on the amount of light exposure, since if the reaction goes to completion, the needle returns to its original shape once the crystal becomes predominantly single domain, i.e. the photoproduct. Although it is much more straightforward to control the duration of light exposure than the direction of illumination for a microcrystal, this still places a limitation on the robustness of the photomechanical response. But the fact that the solid-state reaction kinetics determine the shape change means that the use of small photoreactive crystals may be a general strategy for generating photomechanical motion on very small lengthscales.

In most crystal systems, it is difficult to achieve 100% reaction yields due to reactants that survive at surface or defect sites. For example, a considerable fraction (10-20%) of 9MA monomers do not react in our crystals, but this level of monomer is apparently not enough to maintain the physical deformation seen at intermediate times. Alternatively, the crystal structure itself can limit the reaction yield. For this material, a given crystal always twists the same amount, regardless of the amount of light exposure. A third strategy relies of photophysics rather than crystal engineering. If the reactants

and products have overlapping absorption spectra, a well-chosen excitation wavelength can generate a photostationary state where both reactants and products coexist in equilibrium. Based on our results, generating a robust mixture of reactant and product domains within a single crystal will be an important strategy for generating "intrinsic" directional motion in structures smaller than a wavelength of light.

3.4 Conclusion

In this chapter, we have used a prototypical solid-state reaction, the photodimerization of 9-MA, to investigate how crystal morphology and solid-state reaction dynamics combine to generate photomechanical deformations of single crystals. The different photoinduced motions of these different shapes, bending versus twisting, could be qualitatively understood in terms of the different cross-sectional shapes of these two crystal types. In microneedle crystal shape the maximum deformation occurs at roughly the midpoint of the reaction, rather than at its completion. NMR spin-lattice relaxation measurements and a kinetic analysis of the bending are consistent with the formation of monomer and dimer crystal domains whose interfacial surface area controls the amount of deformation. These observations provide strong evidence for the heterometry mechanism for the mechanical response. It is clear that both the crystal morphology and reaction kinetics must be considered in order to design a molecular nanocrystal with a well-defined "intrinsic" photomechanical response. But although it is a complex problem, the payoff could be considerable, since nanoscale actuators that can be powered remotely by light could have a broad range of applications.

References

1. Schmidt, G.M.J.; Pure and Applied Chemistry 1971, 27, 647.

2. Heller, E.; Schmidt, G.M.J. Israel Journal of Chemistry 1971, 9, 449.

3. Craig, D.P.; Sarti-Fantoni, P. Chemical Communications 1966, 742.

4. Takegoshi, K.; Nakamura, S.; Terao, T. Solid State Nuclear Magnetic Resonance 1998, 11, 189-196.

5. Takegoshi, K. Annual Reports on NMR Spectroscopy 1994, 30, 97.

6. Assink, R. Macromolecules 1978, 11, 1233.

Chapter 4

Photochemical Dynamics of Crystals Composed of 4-chlorocinnamic Acid

This chapter investigates the photochemical dynamics of crystals composed of 4-chlorocinnamic acid (4Cl-CA), whose photochemistry is dominated by an irreversible {2+2} photodimerization reaction. It will contribute to understand crystal morphology of 4-chlorocinnamic acid on the photoresponsive behavior. Solid-state NMR plays a vital role in explaining possible mechanisms and provides clear view of photodimerization. With powder X-ray diffraction and optical and electron microscopy, this work shows that photo-induced twisting can be observed in photoreactive systems. While 4Cl-CA is probably not of practical interest as a photomechanical material, our results provide evidence that the photoinduced twisting of this class of photoreactive crystals is a general phenomenon. Even more surprising, the photomechanical response is only evident in the microribbons, while larger crystals appear completely inert under the same conditions. We discuss possible mechanisms for this size dependence, and propose a mechanism by which the mechanical response of photoreactive molecular crystals may be enhanced by reducing the crystal dimensions.

4.1 Introduction

Recently, there has been a growing appreciation of molecular crystals as dynamic entities that can undergo a variety of chemical reactions. A dramatic illustration of the dynamic nature of molecular crystals is the light-induced bending or expansion of single crystals driven by the photochemical reaction of their constituent molecules [1–8]. We will refer to such photoinduced motions as the ‘‘photomechanical’’ response of the crystal. Such photomechanical crystals may have practical applications as actuators or switches. The use of solid-state photochemical reactions to drive crystal shape changes is limited by the tendency of the crystals to shatter due to internal stresses generated by the reaction [9]. Fortunately, the ability to make molecular crystals with nanoscale dimensions provides a way to avoid crystal fragmentation. First demonstrated for the photopolymerization of reprecipitated acetylene nanoparticles [10], this phenomenon has also been observed for the {2+2} photodimerization reaction in nanoscale cocrystals [11], and for {4+4} photodimerization reactions in molecular crystal nanorods [12]. The survival of the smaller crystals is attributed to their high surface-to-volume ratio, which permits the interfacial stress between reacted and unreacted crystal domains to be dissipated at the surfaces. Solid-state photochemical reactions that cause large crystals to fragment, rendering them useless for photomechanical applications, can proceed without fragmentation in a single-crystal-to-single-crystal fashion in nanoscale crystals.

The ability of nanoscale crystals to survive photochemical transformations provides one example of how the dynamic behavior or photoreactive molecular crystals can be controlled by size. In the current paper, we demonstrate how crystal size can affect

the very existence of a photomechanical response. When assessing the photomechanical properties of a material, our general strategy is to first observe the response of the macroscopic crystals. If they show motion or fracture, then we typically proceed to examine the nanostructured crystals. This strategy has served us well in the past, and in particular for our studies of the photomechanical properties of nano- and microcrystals composed of various crystalline anthracene derivatives [12–15]. 4-chloro-trans-cinnamic acid (4Cl-CA) is of interest because of its similarity to 9-anthracene carboxylic acid (9AC), which crystallizes in one-dimensional (1D) stacks where neighboring molecules undergo a reversible {4+4} photodimerization [16]. Due to statistical considerations, this dimerization reaction cannot go to completion, resulting in the presence of both monomer and dimer molecules after irradiation. The resulting interfacial strain energy can drive the reversible twisting of crystalline microribbons composed of this molecule [17]. We became interested in whether this crystal packing motif could be a general way to create photoresponsive twisting microribbons. We decided to investigate a different type of solid-statephotochemical reaction, the {2+2} photodimerization of cinnamic acid derivatives. The solid-state photochemistry of the trans-cinnamic acids has been a subject of study for over 50 years, and this class of molecules was instrumental in the development of the principles of topochemistry [18-19]. While cinnamic acid itself exists in at least three different crystal polymorphs, 4Cl-CA crystallizes exclusively in the β-form, as shown in Figure 4.1 [20]. This motif, consisting of 1D stacks paired together by hydrogen bonding between the carboxylic acid moieties, is very similar to that seen in 9AC [14].

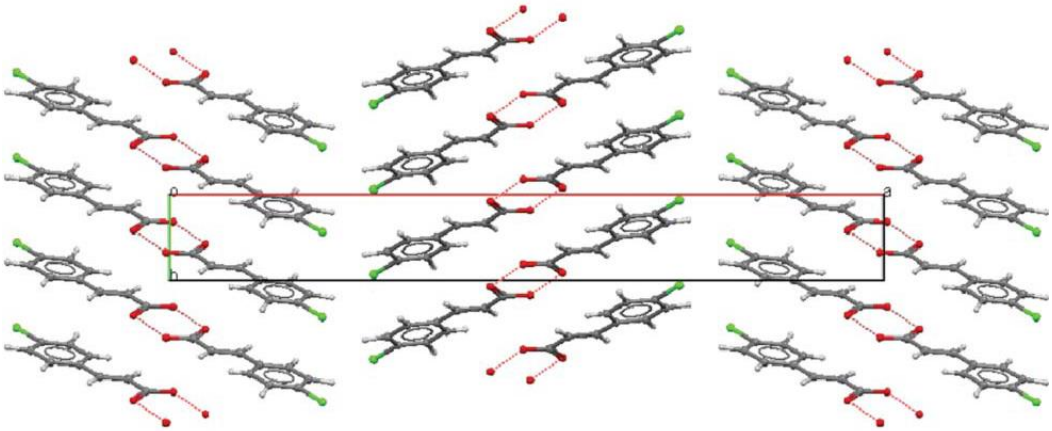

Figure 4.1 A view of the crystal packing of 4-chlorocinnamic acid (4Cl-CA) along the c-axis

Thus we hoped that the {2+2} photodimerization reaction, outlined in Figure 4.2, would generate molecular displacements comparable to that seen in the {4+4} photodimerization of 9AC.

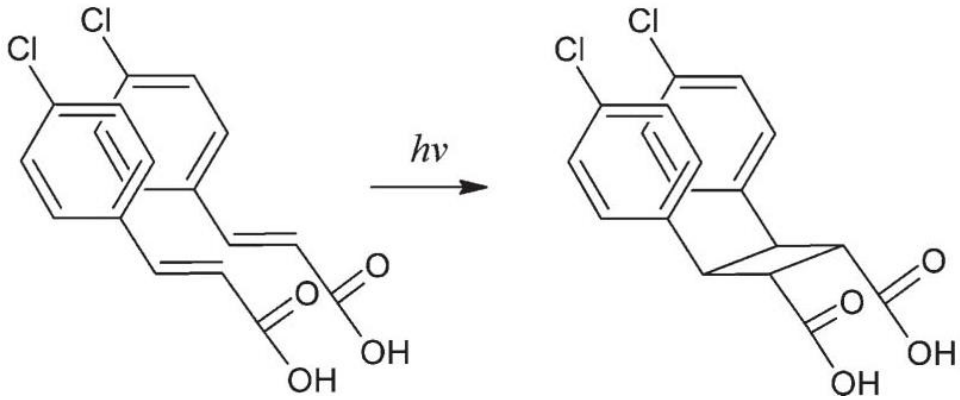

Figure 4.2 Reaction scheme of {2+2} photodimerization of 4Cl-CA in the β-type crystal

4.2 Materials and Methods

4.2.1 Materials

4-chlorocinnamic acid (4Cl-CA) was purchased from Aldrich (99%) and used as received. All solvents used were analytically pure and were filtered before use to remove any dust particles that might act as nucleation sites. Molecular crystals were prepared in three different ways, producing macroscopic shapes that we will refer to as rectangular prisms, plates, and microribbons.

(1) Rectangular prism. These crystals were grown by fast solvent evaporation. A saturated 4Cl-CA solution in ethyl acetate was prepared in an uncovered Petri dish at room temperature and evaporated inside a fume hood. After several hours, crystals were collected from the bottom of the Petri dish. From optical and scanning electron microscopy, most crystals were rectangular prisms with widths and thicknesses ranging between 5 and 20 mm, and lengths ranging from 40 and 100 mm.

(2) Plates. These crystals were grown by slow evaporation after cooling down of heated saturated solution of 4Cl-CA. A saturated 4Cl-CA solution in ethyl acetate was prepared in a Petri dish at 60 uC and covered with aluminum foil. The solution was placed inside a fume hood and the solvent evaporated over several days. Most crystals were irregular plates with hexagonal facets, with thicknesses ranging between 5 and 10 mm, and widths and lengths ranging between 50 and 300 mm.

(3) Microribbons. These crystals were grown by the floating drop method. 1.9 mg of 4Cl-CA was dissolved in 1.0 ml of ethyl acetate and slowly added to the surface of

10 ml MilliQ water in a Petri dish. The dish was covered and the solvent was evaporated over the course of 1–2 days. The 4Cl-CA crystallized out as microribbons on the surface of water, with thicknesses of 1 mm or less, widths ranging between 10 and 50 mm, and lengths ranging between 50 and 300 mm.

4Cl-CA crystals grown from ethyl acetate were powdered using a mortar and pestle and suspended in MilliQ water during their UV exposure.

4.2.2 ^{13}C Solid-state NMR

Cross-polarization (CP) magic-angle-spinning (MAS) solid-state NMR experiments were performed at 9.4 T (^{1}H frequency 400 MHz) on a Bruker AVANCE spectrometer equipped with a double-resonance 4 mm MAS probe, spinning at a MAS rate of 8 kHz. 83 kHz ^{1}H $\pi/2$ and decoupling pulses were used along with a 2 ms CP spin-lock. During CP the ^{13}C nutation rate was set to 40.5 kHz and the ^{1}H nutation rate ramped from 58–77 kHz. For each spectrum, 4096 complex data points with a dwell of 10 μs (spectral width 50 kHz, total acquisition time 41.01 ms) were acquired with a recycle delay of 240 s for a total experiment time of 17 h and 20 min.

4.3 Results and Disccusion

To confirm photodimerization of the 4Cl-CA molecules, we used ^{13}C solid-state NMR spectroscopy to monitor chemical changes for individual carbons. In Figure 4.3a, we show the well-resolved ^{13}C spectrum of the monomer before irradiation, consistent with a well-ordered molecular crystal. After irradiation, Figure 4.3b and 4.3c show a steady decrease in the areas of the vinyl carbons at chemical shifts 118.9 and 148.1 ppm, with simultaneous growth of the cyclobutane peaks clustered around 45 ppm. The aromatic region from 125–135 ppm retains its intensity and general shape, suggesting that only the {2+2} dimerization across the double bonds is occurring. The loss of intensity for the carboxylic acid resonance at 175 and the appearance of a new acid resonance at 185 ppm reflect the different chemical environments of the two COOH groups on the 4,4'-dichloro-truxinic acid photodimer product. All the changes in the ^{13}C spectrum are similar to those seen previously for other cinnamic acid derivatives [21–23]. The other notable feature of the ^{13}C spectra is broadening of the peaks as the reaction progresses, which is particularly evident in the carboxylic acid region. This broadening is due to a distribution of microscopic environments giving rise to varying chemical shifts and provides a qualitative measure of the disorder in the solid. To check whether dynamic motions play a role in the broadening, the ^{13}C spectrum of a partially reacted sample (20 min of exposure) was taken at both 20 Celsius degrees and 225 Celsius degrees. The broadening was identical at both temperatures. This provides at least a preliminary indication that the peak broadening is due to an increase in the static disorder within the solid as the photodimerization progresses. We cannot say whether this disorder

arises from an amorphous phase that is formed after reaction, or whether it is present in the crystal phases. The solid-state NMR data shows that the 4Cl-CA solid-state photodimerization does form a new crystal phase, but there is also indication of increased disorder or the generation of an amorphous phase.

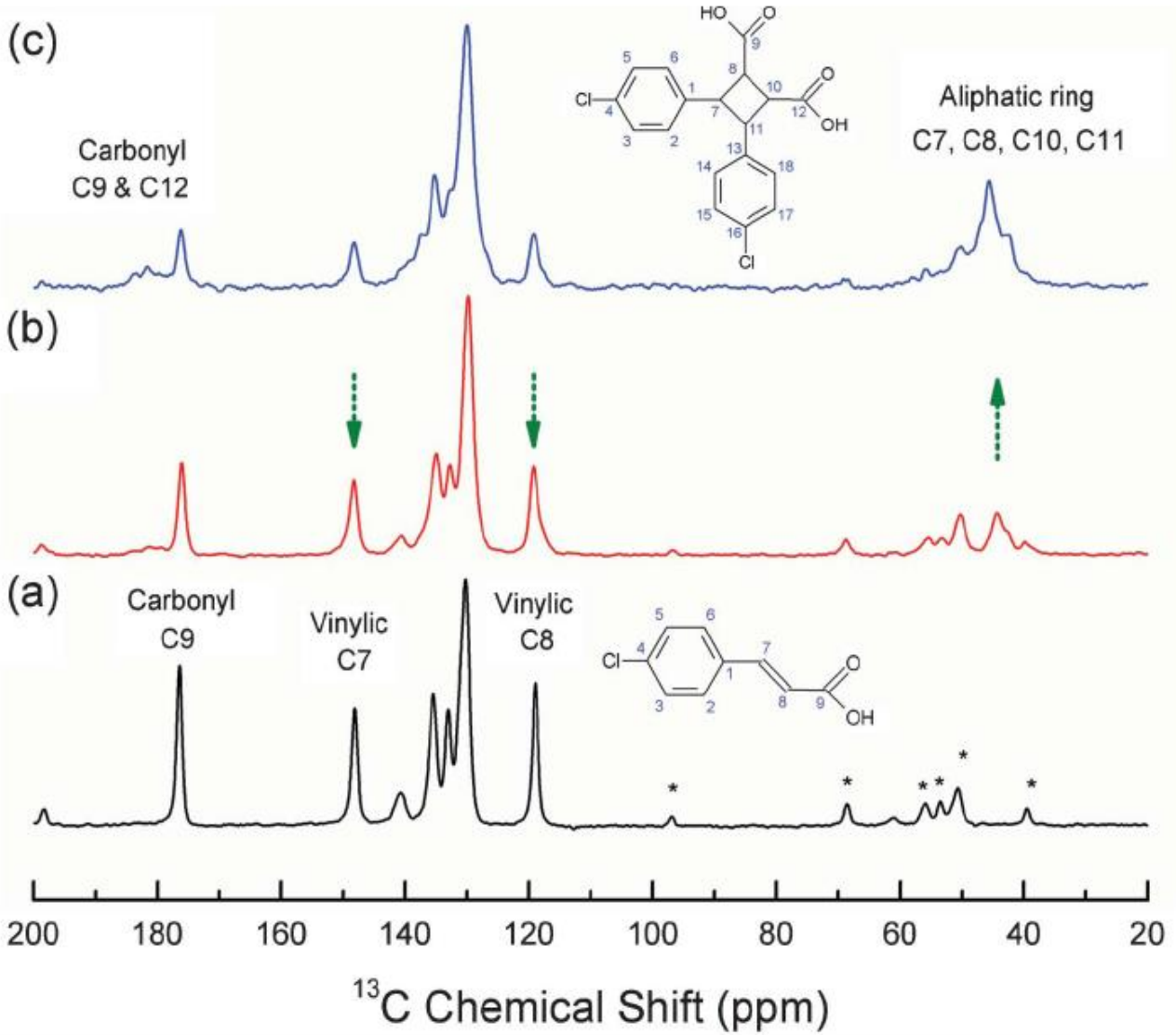
(c)
Carbonyl
C9 & C12
Aliphatic ring
C7, C8, C10, C11
(b)
(a)
Carbonyl
C9
Vinylic
C7
Vinylic
C8
200
180
160
140
120
100
80
60
40
20
13C Chemical Shift (ppm)

Figure 4.3 ^{13}C solid-state NMR data of polycrystalline 4Cl-CA powder (a) before exposure to UV, (b) after 10 min of UV exposure, and (c) after 30 min of UV exposure. Carbon numbering of 4Cl-CA monomer and dimer are shown in the insets. Formation of the dimer is characterized by the appearance of cyclobutane resonances at 45 ppm and the decrease of the vinyl C7 and C8 peaks at 118.9 and 148.1ppm. Spinning sidebands are marked with asterisks.

SEM images of representative crystals are shown in Figure 4.4a. Thick (5–10 mm) plate-like crystals, shown in Figure 4.4b, were grown by slow evaporation of an ethyl acetate solution over the course of days. Thinner plates (<1 mm), which we refer to as microribbons, were grown using the floating drop method, similar to our procedure for 9AC. These microribbons are shown in Figure 4.4c. It is important to emphasize that all three crystals in Figure 4.4 were grown from the same ethyl acetate solution, but with small changes in growth conditions that led to large changes in crystal shape.

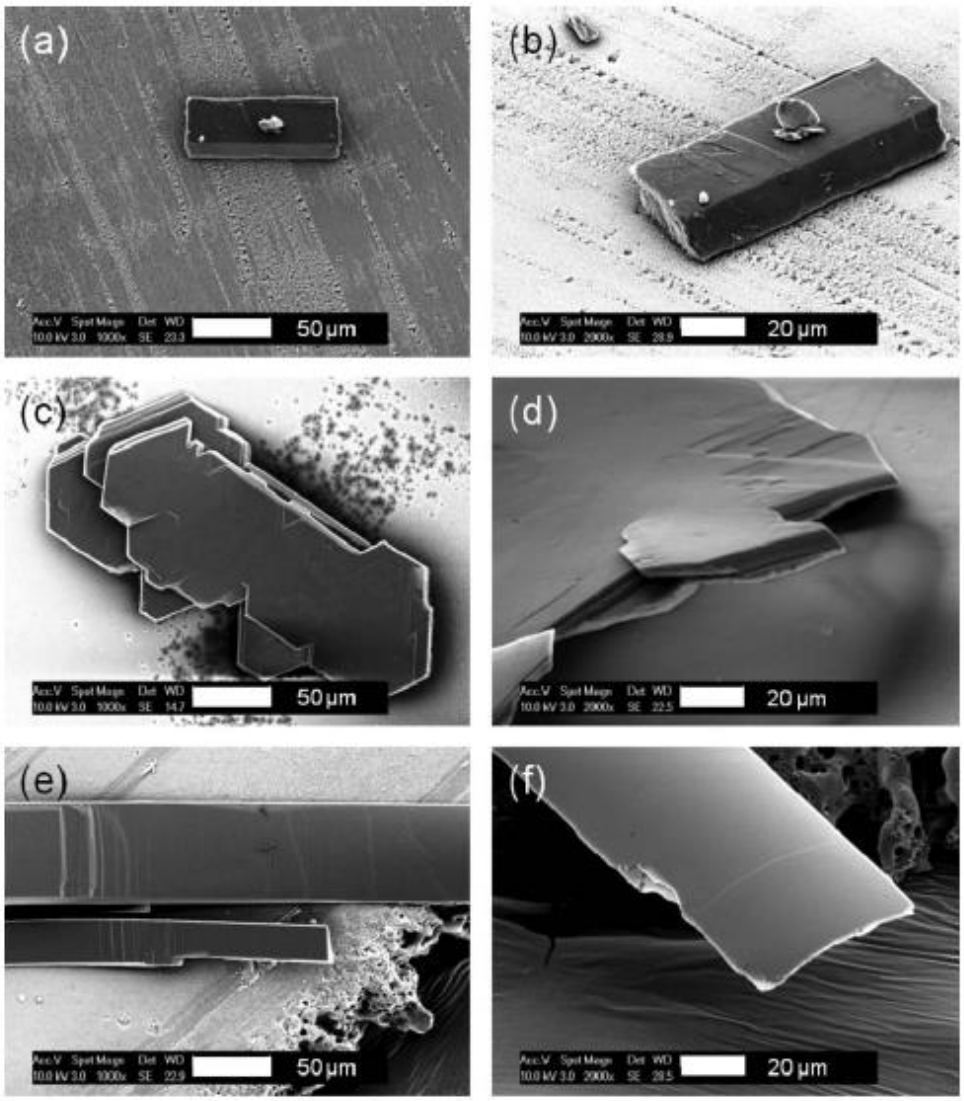

Figure 4.4 SEM micrographs of (a, b) 4Cl-CA rectangular prism crystals prepared by rapid solvent evaporation, (c, d) 4Cl-CA plate crystals prepared by slow evaporation, and (e, f) 4Cl-CA microribbons prepared by the floating drop method. (a, c, e) show top views of each molecular crystal to gauge their widths, and (b, d, f) show tilted views of the crystals to show their thicknesses. Note that the microribbon in (f) is much thinner than the plate in (d).

Both the macroscopic rectangular prisms and plates show no changes under illumination, as shown in the sequence of images in Figure 4.5a and 4.5b. If the UV exposure is continued, the crystals begin to melt after about 20 min but never undergo the splintering or jumping that we typically see in photomechanically active organic crystals like 9AC. Nevertheless, the thinner crystals grown by our microribbon method show twisting under the same irradiation conditions, as shown in Figure 4.5c. This twisting is similar to what we have observed previously for microribbons composed of 9AC, but is not reversible because the 4Cl-CA photodimer product is stable. The twisted microribbon in Figure 4.5c continues to change even in the absence of light, slowly fracturing into what appear to be multiple smaller crystals over the course of 1 h. This decomposition was observed for at least 90% of the twisted microribbons. For the larger crystals, in most cases after UV exposure, whiskers could be observed growing out of the side of the main crystal after several hours in the dark.

In 4Cl-CA, the photodimerization is not reversible at room temperature, and the photodimerized crystal decomposes over the course of hours. The origin of the slow changes in crystal morphology that take place after the light is turned off is not clear. The irreversibility and loss of crystal integrity clearly limits the potential of this material as a practical photoactuator.

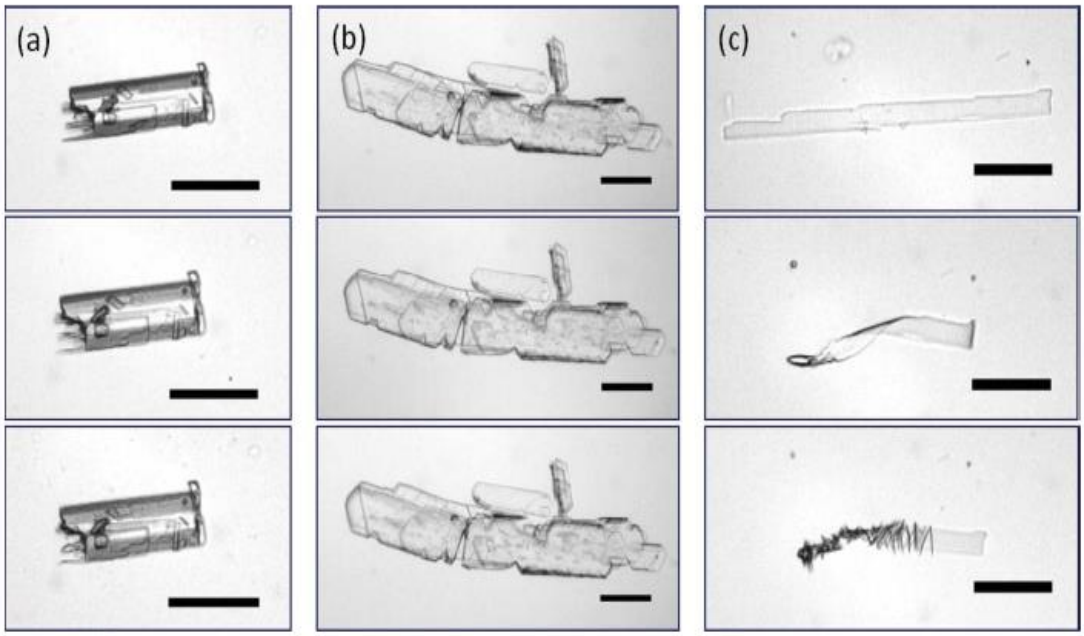

Figure 4.5 Optical images of (a) a 4Cl-CA rectangular prism crystal prepared by solvent evaporation, (b) a 4Cl-CA plate crystal prepared by slow precipitation, and (c) a 4Cl-CA microribbon prepared by the floating drop method. The top images was taken before UV (365 nm) exposure, the middle images were taken after 5 min UV exposure, and bottom images were taken 1 h after turning off the UV. Scale bars: 50 mm.

4.4 Conclusion

The ^{13}C solid-state NMR spectra clearly show the whole process of photodimerization of 4Cl-CA. The dimer peaks keep growing up and the monomer peaks keep going down or shifting. We can see the advantage of solid-state NMR in understanding the photochemical mechanism of 4Cl-CA. The chemical shift is very sensitive to the photodimerization and here we make use of a combined solid-state NMR, powder X-ray diffraction and electron and optical microscopy to characterize the photochemical response of 4Cl-CA.

With optical microscopy, PXRD, IR and solid-state NMR data [24], we find that microribbons composed of crystalline 4Cl-CA show a photoinduced twisting similar to that of 9AC microribbons. These results suggest that the twisting is a general phenomenon of microribbons that contain this type of 1D photoreactive molecular stack. All the pictures show that the photochemistry is dominated by the irreversible {2+2} photodimerization reaction, and that a new crystal phase is formed. The twisted microribbons disintegrate over the course of hours after the photoreaction, and thus 4Cl-CA is not very promising as a photomechanical material. Perhaps the most surprising observation in this work is that larger crystals of 4Cl-CA are mechanically inert when irradiated—it is only the microribbons that exhibit a change in shape (i.e. twisting). There are several possible explanations for this divergent behavior, ranging from differences in light absorption, crystal quality, and heat dissipation. But the most intriguing explanation is that the nonlinear scaling of mechanical properties, like the torsion constant, with crystal size can make smaller crystals more deformable than larger crystals. Of course,

this result will depend on the detailed shape of the crystal, but our results suggest how controlling the nanoscale crystal dimensions can lead to qualitative changes in the photomechanical response. While more work needs to be done on how mechanical properties scale with crystal size and shape, we hope the current results motivate further research on controlling the growth of molecular crystals on submicron lengthscales.

References

1. Boldyreva, E. V.; Sinelnikov, A. A.; Chupakhin, A. P.; Lyakhov N. Z.; Boldyrev, V. V. Doklady Akad. Nauk USSR 1984, 277, 893–896.

2. Lange, C. W.; Foldeaki, M.; Nevodchikov, V. I.; Cherkasov, V. K.; Abakumov G. A.; Pierpont, C. G. Journal of the American Chemical Society 1992, 114, 4220–4222.

3. Kobatake, S.; Takami, S.; Muto, H.; Ishikawa T.; Irie, M. Nature 2007, 446, 778–781.

4. Colombier, I.; Spagnoli, S.; Corval, A.; Baldeck, P. L.; Giraud, M.; Leaustic, A.; Yu, P.; Irie, M. Journal of Chemical Physics 2007, 126(011101/1-011101).

5. Uchida, K.; Sukata, S.; Matsuzawa, Y.; Akazawa, M.; Jong, J. J. D. d.; Katsonis, N.; Kojima, Y.; Nakamura, S.; Areephong, J.; Meetsma, A.; Feringa, B. L. Chemical Communications 2008, 326-328.

6. Koshima, H.; Ojima N.; Uchimoto, H.; Journal of the American Chemical Society 2009, 131, 6890–6891.

7. Morimoto, M.; Irie, M. Journal of the American Chemical Society 2010, 132, 14172-14178.

8. Naumov, P.; Kowalik, J.; Solntsev, K. M.; Baldridge, A.; Moon, J.-S.; Kranz, C.; Tolbert, L. M. Journal of the American Chemical Society 2010, 132, 5845-5857.

9. Keating, A. E.; Garcia-Garibay, M. A. Photochemical solid-to-solid reactions. In Organic and Inorganic Photochemistry, Marcel Dekker: New York 1998.

10. Takahashi, S.; Miura, H.; Kasai, H.; Okada, S.; Oikawa, H.; Nakanishi, H. Journal of the American Chemical Society 2002, 124, 10944-10945.

11. Bucar, D. K.; MacGillivray, L. R. Journal of the American Chemical Society 2007, 129, 32-33.

12. Al-Kaysi, R. O.; Muller, A. M.; Bardeen, C. J. Journal of the American Chemical Society 2006, 128, 15938-15939.

13. Zhu, L.; Agarwal, A.; Lai, J.; Mueller, L.J.; Bardeen, C.J. Journal of Materials Chemistry 2011, 21, 6258-6268.

14. Zhu, L.; Al-Kaysi, R. O.; Dillon, R. J.; Tham, F. S.; Bardeen, C. J. Crystal Growth & Design 2011, 11, 4975-4983.

15. Al-Kaysi, R. O.; Bardden, C. J. Advanced Materials 2007, 19, 1276-1280.

16. Ito, Y.; Fujita, H. The Journal of Organic Chemistry 1996, 61, 5677-5680.

17. Zhu, L.; Al-Kaysi, R. O.; Bardeen, C. J. J. Journal of the American Chemical Society 2011, 133, 12569-12575.

18. Cohen, M. D.; Schmidt, G. M. J.; Sonntag, F. I. Journal of the Chemical Society 1964, 2000-2013.

19. Schmidt, G. M. J. Journal of the Chemical Society 1964, 2014-2021.

20. Glusker, J. P.; Zacharias, D. E.; Carrell, H. L. Journal of the Chemical Society, Perkin Transactions 2, 1975, 68-74.

21. Khan, M.; Brunklaus, G.; Enkelmann, V.; Spiess, H. W. Journal of the American Chemical Society 2008, 130, 1741-1748.

22. Bertmer, M.; Nieuwendaal, R. C.; Barnes, A. B.; Hayes, S. E. The Journal of Physical Chemistry B 2006, 110, 6270-6273.

23. Fonseca, I.; Hayes, S. E.; Blumich, B.; Bertmer, M. Physical Chemistry Chemical Physics 2008, 10, 5898-5907.

24. Kim, T.; Zhu, L.; Mueller, L.J.; Bardeen, C.J. CrystEngComm 2012, 14, 7792-7799.

APPENDIX

A1. Mathematica Codes for Fitting Intensity of Peaks in NMR Spectrum and T1

This is the fitting for 30 min UV sample.

```
Directories & settings
TOOLS="C://Users//Lingchao//Desktop//T1//";
DATA="C://Users//Lingchao//Desktop//T1//bardeen vdlist//";
NAME="rk_March13_9MA_6_";
Get tools
<<"NonlinearRegression`";
Get[TOOLS<>"stat60.m"];
General::obspkg: _NonlinearRegression`_ is now obsolete. The legacy version
being loaded may conflict with current Mathematica functionality. See the
Compatibility Guide for updating information. ≫

cut[data_,list_]:=Flatten[Table[Take[data,{list[[i]],list[[i+1]]}],{i,1,Length[list],2
}],1]
spline3[a_,b_,c_,d_,x_]:=a+b x +c x^2+d x^3
readjcamp6[filename_,pointstartin_,pointendin_]:=Module[{datalist},findstring="
$$ End of Bruker specific parameters";
 datafile=OpenRead[filename];
 While[Read[datafile,Record]≠findstring];
 Read[datafile,Record];
 Read[datafile,Record];
 Read[datafile,Record];
 Read[datafile,Word];
 xfactor=Read[datafile,Number];
 Read[datafile,Record];
 Read[datafile,Word];
 firstx=Read[datafile,Number];
 Read[datafile,Record];
 Read[datafile,Record];
 Read[datafile,Word];
 maxy=Read[datafile,Number];
 maxy=10^8;
 Read[datafile,Record];
 Read[datafile,Word];
 npoints=Read[datafile,Number];
 Read[datafile,Record];
 Read[datafile,Record];
```

```
 linestart=Floor[pointstartin/1];
 lineend=Floor[pointendin/1];
 pointstart=1*linestart;
 pointend=1*lineend;
 refstart=-firstx+xfactor (pointstart-1);
 Do[Read[datafile,Record],{i,1,linestart-1}];
 temp=Table[Table[Read[datafile,{Number,Number}]],{j,linestart,lineend}];
 datalist={};
 Do[datalist=Join[datalist,Table[{refstart+(1(i-
1))*xfactor,temp[[i,j]]/maxy}//N,{j,2,2}]],{i,1,lineend-linestart+1}];
 Close[filename];
 datalist]
ref
ref
k=1024;
file="13.dx";
datapairs13=readjcamp6[DATA<>NAME<>file,1k,2k];
file="14.dx";
datapairs14=readjcamp6[DATA<>NAME<>file,1k,2k];
file="15.dx";
datapairs15=readjcamp6[DATA<>NAME<>file,1k,2k];
file="16.dx";
datapairs16=readjcamp6[DATA<>NAME<>file,1k,2k];
datapairs=(datapairs16+datapairs13+datapairs14+datapairs15)/4;
ListPlot[ datapairs,Joined→True,PlotRange->All]
```

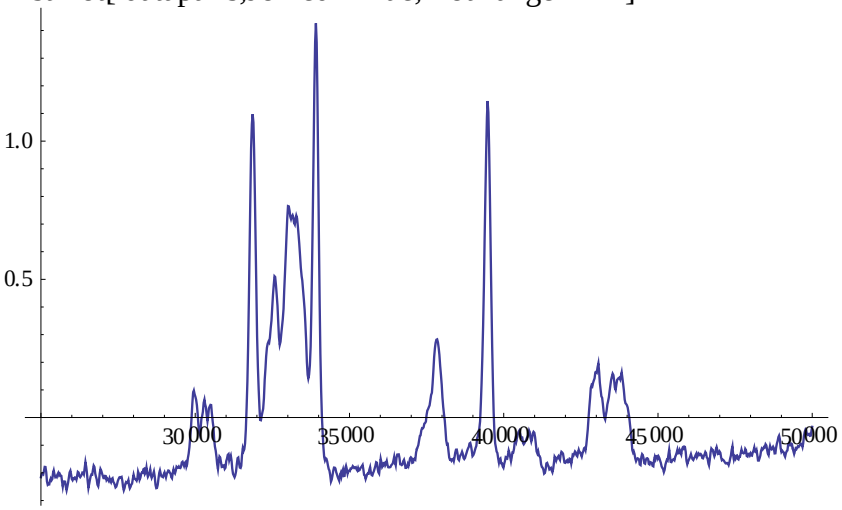


```
slorentzian2[position_,intensity1_,intensity2_,width_,freq_,x_]:=intensity1/(width
(1+4 ((x-position)/width)^2))+intensity2/(width (1+4 ((x-(position+freq))/width)^2))
slorentzian[position_,intensity1_,intensity2_,width_,x_]:=slorentzian2[position,in
tensity1,intensity2,width,10500,x]
```

```
startparams={{lorentzian,{32000,500,150}},{lorentzian,{34000,500,150}},{lore
ntzian,{38000,500,150}},{lorentzian,{39400,500,150}},{slorentzian,{30000,40,1
0,150}},{slorentzian,{30200,40,10,150}},{slorentzian,{30400,40,10,150}},{slore
ntzian,{32300,40,10,150}},{slorentzian,{32700,100,30,150}},{slorentzian,{3300
0,200,50,150}},{slorentzian,{33300,200,50,150}},{slorentzian,{33500,100,30,15
0}},{cube,{-0.2,0,0,0}}}
{{lorentzian,{32000,500,150}},{lorentzian,{34000,500,150}},{lorentzian,{3800
0,500,150}},{lorentzian,{39400,500,150}},{slorentzian,{30000,40,10,150}},{slo
rentzian,{30200,40,10,150}},{slorentzian,{30400,40,10,150}},{slorentzian,{323
00,40,10,150}},{slorentzian,{32700,100,30,150}},{slorentzian,{33000,200,50,15
0}},{slorentzian,{33300,200,50,150}},{slorentzian,{33500,100,30,150}},{cube,{
-0.2,0,0,0}}}
startparams={{lorentzian,{31866.38849110443`,363.1196980762516`,188.33373
010405938`}},{lorentzian,{33913.36132114169`,370.4719073107956`,159.8481
4780278322`}},{lorentzian,{37811.21077363562`,273.2945826879941`,471.171
9928916145`}},{lorentzian,{39480.131410248534`,177.22530294549713`,207.5
103368609727`}},{slorentzian,{29974.797049774872`,78.34394666069804`,40.
88658322253561`,210.3053141000107`}},{slorentzian,{30308.297670855845`,7
3.5466741820938`,37.715343780472764`,226.0375883103235`}},{slorentzian,{
30520.270311873257`,28.502630608894012`,15.088712126391437`,140.478389
14152047`}},{slorentzian,{32381.938067762985`,4.160838532119172`,21.5110
02008958986`,2.1183837211441796`}},{slorentzian,{32539.66392362706`,111.
59777664089492`,83.90901580859558`,372.2109304421125`}},{slorentzian,{32
998.597900667046`,306.0082437159904`,108.63208982928252`,325.335016546
02384`}},{slorentzian,{33282.58259616752`,154.64565088871586`,52.7995980
83348805`,271.8931814947634`}},{slorentzian,{33476.78613558021`,52.73688
776888131`,29.472710084117292`,186.3752709774901`}},{cube,{-
0.8051325605804054`,0.000054822728510553625`,-1.756714449186261`*^-
9,1.9011201043803538`*^-14}}}
{{lorentzian,{31866.4,363.12,188.334}},{lorentzian,{33913.4,370.472,159.848}
},{lorentzian,{37811.2,273.295,471.172}},{lorentzian,{39480.1,177.225,207.51}
},{slorentzian,{29974.8,78.3439,40.8866,210.305}},{slorentzian,{30308.3,73.54
67,37.7153,226.038}},{slorentzian,{30520.3,28.5026,15.0887,140.478}},{slorent
zian,{32381.9,4.16084,21.511,2.11838}},{slorentzian,{32539.7,111.598,83.909,3
72.211}},{slorentzian,{32998.6,306.008,108.632,325.335}},{slorentzian,{33282.
6,154.646,52.7996,271.893}},{slorentzian,{33476.8,52.7369,29.4727,186.375}},
{cube,{-0.805133,0.0000548227,-1.75671?10^-9,1.90112?10^-14}}}
data$sim=gensim[datapairs,startparams];
plot$sim=ListPlot[data$sim,PlotRange→All,Joined→True,DisplayFunction→Ident
ity];
plot$data=ListPlot[datapairs,PlotRange→All,Joined→True,DisplayFunction→Ident
ity,PlotStyle→Red];
Show[plot$data,plot$sim,DisplayFunction→$DisplayFunction]
```

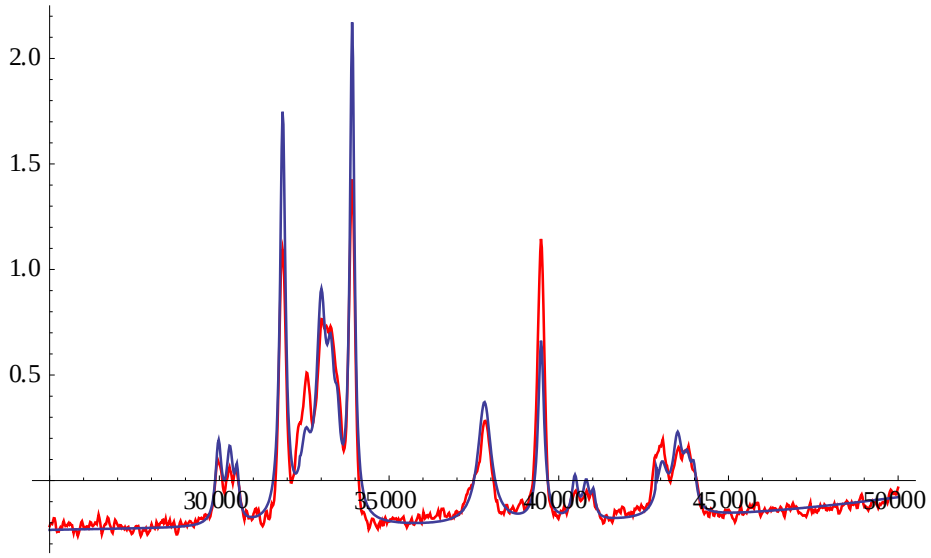

fitresults1=fitresults=fitdatatight[datapairs,startparams]
FindFit::cvmit: Failed to converge to the requested accuracy or precision within _100_ iterations. ≫
{{lorentzian,{31859.6,269.083,198.225}},{lorentzian,{33908.7,291.431,176.2}},{lorentzian,{37803.7,243.912,524.892}},{lorentzian,{39474.7,291.517,208.311}},{slorentzian,{29972.3,71.2032,30.9118,242.358}},{slorentzian,{30293.3,39.7401,21.928,204.713}},{slorentzian,{30503.,40.7519,19.7154,195.662}},{slorentzian,{32349.9,44.8826,46.9233,203.298}},{slorentzian,{32571.,143.186,76.6504,264.371}},{slorentzian,{33021.9,269.655,85.5574,349.722}},{slorentzian,{33297.2,189.789,70.113,297.374}},{slorentzian,{33499.4,53.6653,19.5103,179.137}},{cube,{-0.723644,0.0000508143,-1.70871?10^{-9},1.89758?10^{-14}}}}
data$sim=gensim[datapairs,fitresults];
plot$sim=ListPlot[data$sim,PlotRange→All,Joined→True,DisplayFunction→Identity,PlotStyle→{RGBColor[1,0,0]}];
plot$data=ListPlot[datapairs,PlotRange→All,Joined→True,DisplayFunction→Identity];
Show[plot$data,plot$sim,DisplayFunction→$DisplayFunction,Frame→True,Axes→False]

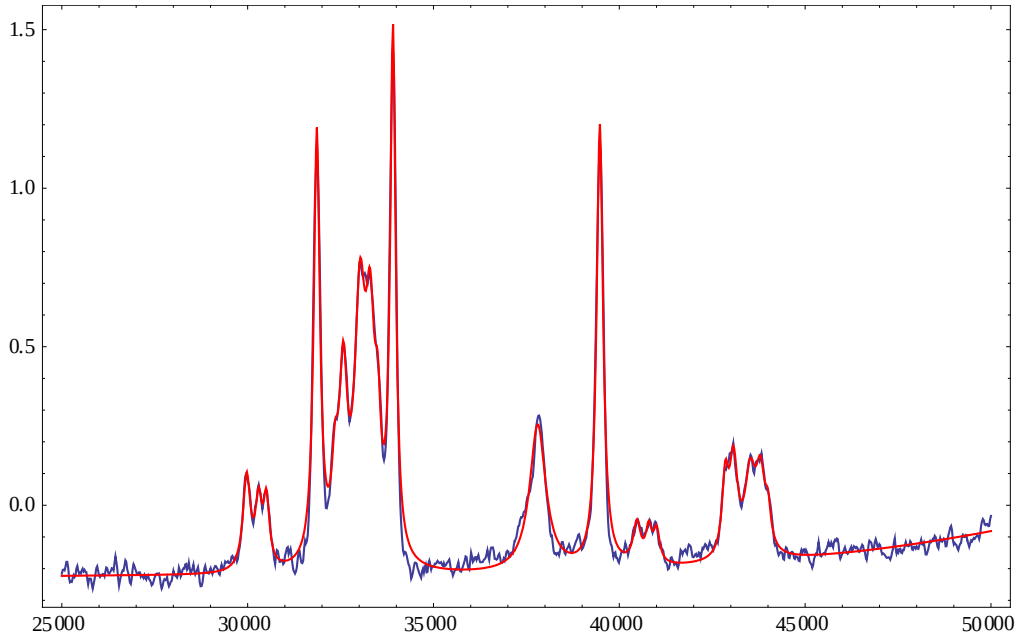


```
data$res=Table[{datapairs i,1\[RightDoubleBracket],datapairs i,2\[RightDoub
leBracket]-data$sim i,2\[RightDoubleBracket]},{i,Length[datapairs]}];
plot$res=ListPlot[data$res,PlotRange All,Joined True,DisplayFunction Iden
tity];
Show[plot$res,DisplayFunction $DisplayFunction,Frame True, Axes False]
```

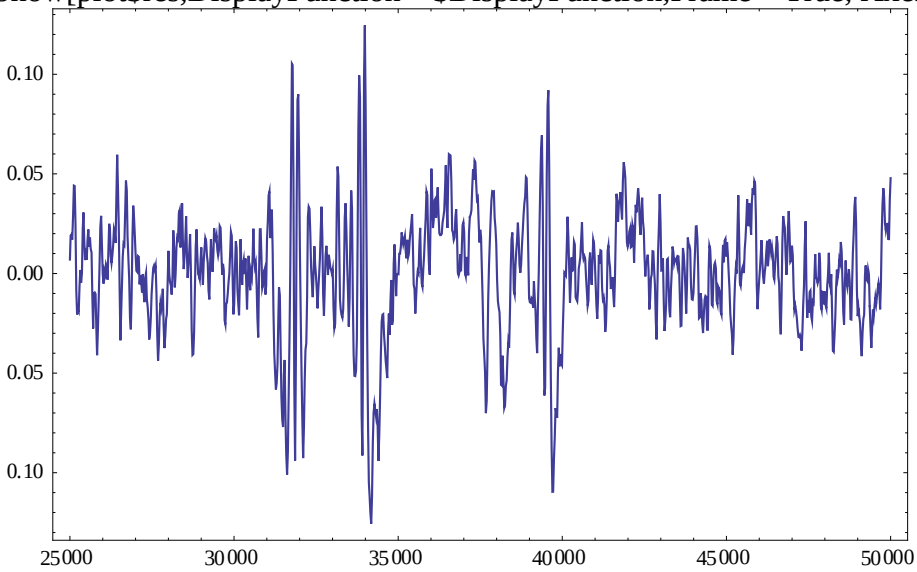


```
peak1[A_,x_]:=lorentzian[31859.574037096965`,A,198.22491994478946`,x]
peak2[A_,x_]:=lorentzian[33908.68135176172`,A,176.20006388893464`,x]
peak3[A_,x_]:=lorentzian[37803.651830521085`,A,524.8924664140686`,x]
peak4[A_,x_]:=lorentzian[39474.677624160344`,A,208.31124395422665`,x]
peak1s[A_,x_]:=slorentzian[29972.285235216816`,71.20316405340469`A,30.91
182051116609`A,242.35797451720285`,x]
```

```
peak2s[A_,x_]:=slorentzian[30293.32276144176`,39.740097667291344`A,21.92
797953585461`A,204.71276719010427`,x]
peak3s[A_,x_]:=slorentzian[30503.019660800997`,40.751920384396364`A,19.7
15407478640213`A,195.66189415607235`,x]
peak4s[A_,x_]:=slorentzian[32349.86633263552`,44.8825809536869`A,46.9233
1546280715`A,203.29759755046797`,x]
peak5s[A_,x_]:=slorentzian[32570.956307912737`,143.1860498914969`A,76.65
042413926673`A,264.3714032348878`,x]
peak6s[A_,x_]:=slorentzian[33021.90859827081`,269.65524370859254`A,85.55
744657467395`A,349.722485764084`,x]
peak7s[A_,x_]:=slorentzian[33297.21513420799`,189.78882529432602`A,70.11
304186326775`A,297.3736705926545`,x]
peak8s[A_,x_]:=slorentzian[33499.37518274259`,53.665302796639615`A,19.51
0293822197344`A,179.13728901784265`,x]

k=1024;

file="16.dx";
datapairs=readjcamp6[DATA<>NAME<>file,1k,2k];
ListPlot[ datapairs,Joined→True,PlotRange->All]
```

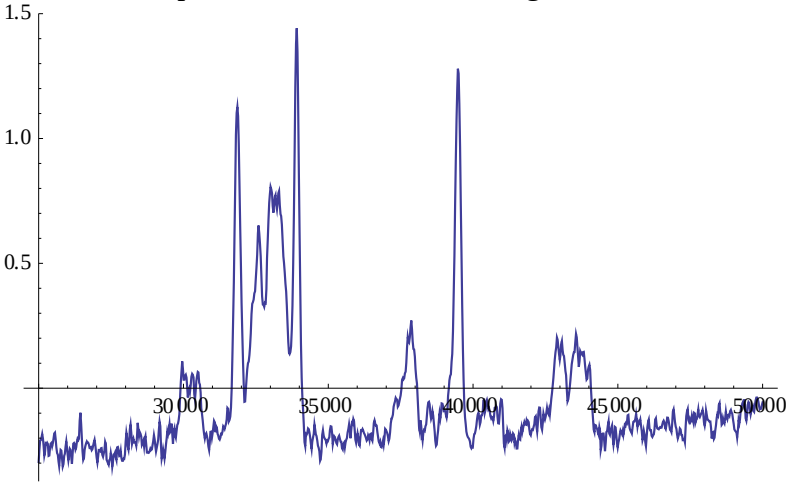


```
startparams={{peak1,{363.1196980762516}},{peak2,{370}},{peak3,{273}},{pe
ak4,{177}},{peak1s,{1}},{peak2s,{1}},{peak3s,{1}},{peak4s,{1}},{peak5s,{1}
},{peak6s,{1}},{peak7s,{1}},{peak8s,{1}},{cube,{-
0.8051325605804054`,0.000054822728510553625`,-1.756714449186261`*^-
9,1.9011201043803538`*^-14}}}
{{peak1,{363.12}},{peak2,{370}},{peak3,{273}},{peak4,{177}},{peak1s,{1}},
{peak2s,{1}},{peak3s,{1}},{peak4s,{1}},{peak5s,{1}},{peak6s,{1}},{peak7s,{1
}},{peak8s,{1}},{cube,{-0.805133,0.0000548227,-1.75671?10^-9,1.90112?10^-14}}}
data$sim=gensim[datapairs,startparams];
plot$sim=ListPlot[data$sim,PlotRange→All,Joined→True,DisplayFunction→Ident
ity];
```

plot$data=ListPlot[datapairs,PlotRange→All,Joined→True,DisplayFunction→Identity,PlotStyle→Red];
Show[plot$data,plot$sim,DisplayFunction→$DisplayFunction]

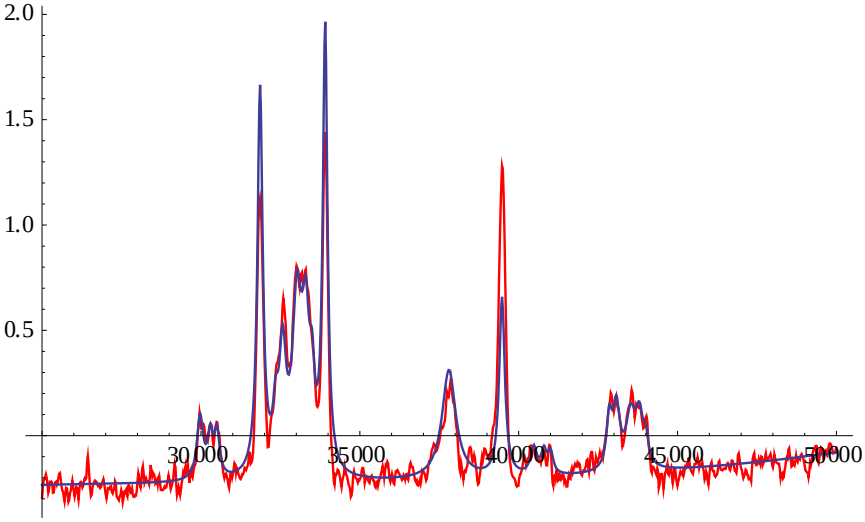

fitresults16=fitresults=fitdatatight[datapairs,startparams]
{{peak1,{279.112}},{peak2,{289.046}},{peak3,{237.426}},{peak4,{331.204}},{peak1s,{1.04016}},{peak2s,{1.0138}},{peak3s,{1.046}},{peak4s,{1.06595}},{peak5s,{1.17842}},{peak6s,{1.0654}},{peak7s,{1.05252}},{peak8s,{1.03179}},{cube,{-0.89633,0.0000640854,-2.08723?10^{-9},2.25843?10^{-14}}}}
data$sim=gensim[datapairs,fitresults];
plot$sim=ListPlot[data$sim,PlotRange→All,Joined→True,DisplayFunction→Identity,PlotStyle→{RGBColor[1,0,0]}];
plot$data=ListPlot[datapairs,PlotRange→All,Joined→True,DisplayFunction→Identity];
Show[plot$data,plot$sim,DisplayFunction→$DisplayFunction,Frame→True,Axes→False]

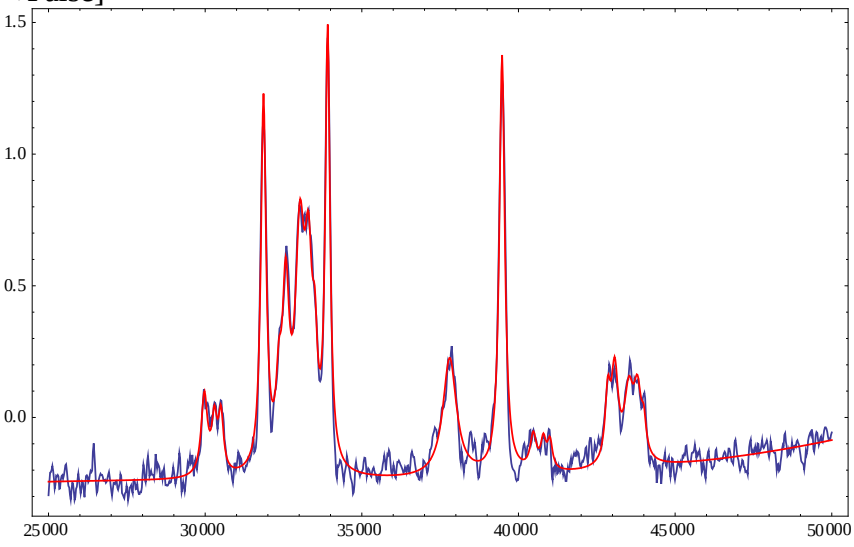

```
data$res=Table[{datapairs i,1\[RightDoubleBracket],datapairs i,2\[RightDoubl Bracket]-data$sim i,2\[RightDoubleBracket]},{i,Length[datapairs]}];
plot$res=ListPlot[data$res,PlotRange All,Joined True,DisplayFunction Identity];
Show[plot$res,DisplayFunction $DisplayFunction,Frame True, Axes→False]
```

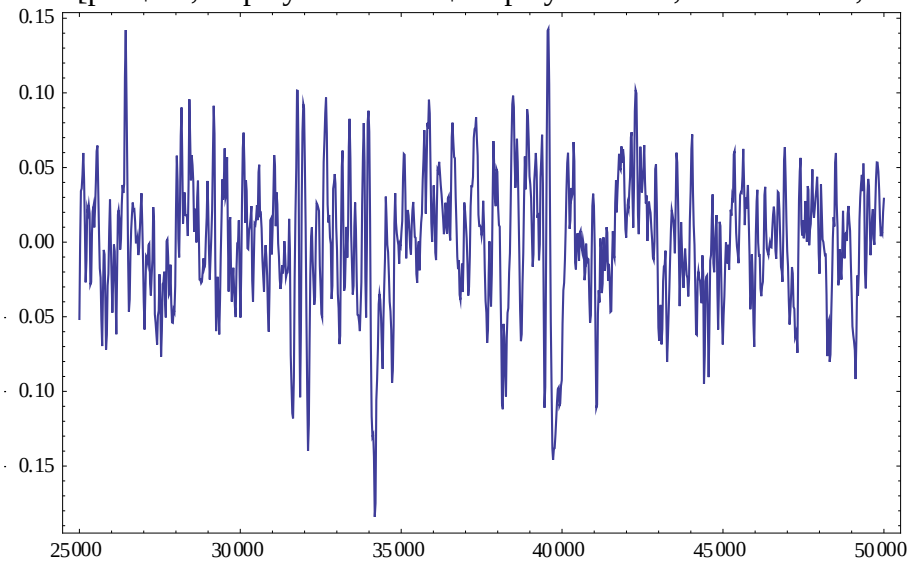

Then repeat reading and fitting file from file="15.dx" to file="1.dx".

```
peaks={{fitresults1[[1,2,1]],fitresults1[[2,2,1]],fitresults1[[3,2,1]],fitresults1[[4,2,1]]},{fitresults2[[1,2,1]],fitresults2[[2,2,1]],fitresults2[[3,2,1]],fitresults2[[4,2,1]]},{fitresults3[[1,2,1]],fitresults3[[2,2,1]],fitresults3[[3,2,1]],fitresults3[[4,2,1]]},{fitresults4[[1,2,1]],fitresults4[[2,2,1]],fitresults4[[3,2,1]],fitresults4[[4,2,1]]},{fitresults5[[1,2,1]],fitresults5[[2,2,1]],fitresults5[[3,2,1]],fitresults5[[4,2,1]]},{fitresults6[[1,2,1]],fitresults6[[2,2,1]],fitresults6[[3,2,1]],fitresults6[[4,2,1]]},{fitresults7[[1,2,1]],fitresults7[[2,2,1]],fitresults7[[3,2,1]],fitresults7[[4,2,1]]},{fitresults8[[1,2,1]],fitresults8[[2,2,1]],fitresults8[[3,2,1]],fitresults8[[4,2,1]]},{fitresults9[[1,2,1]],fitresults9[[2,2,1]],fitresults9[[3,2,1]],fitresults9[[4,2,1]]},{fitresults10[[1,2,1]],fitresults10[[2,2,1]],fitresults10[[3,2,1]],fitresults10[[4,2,1]]},{fitresults11[[1,2,1]],fitresults11[[2,2,1]],fitresults11[[3,2,1]],fitresults11[[4,2,1]]},{fitresults12[[1,2,1]],fitresults12[[2,2,1]],fitresults12[[3,2,1]],fitresults12[[4,2,1]]},{fitresults13[[1,2,1]],fitresults13[[2,2,1]],fitresults13[[3,2,1]],fitresults13[[4,2,1]]},{fitresults14[[1,2,1]],fitresults14[[2,2,1]],fitresults14[[3,2,1]],fitresults14[[4,2,1]]},{fitresults15[[1,2,1]],fitresults15[[2,2,1]],fitresults15[[3,2,1]],fitresults15[[4,2,1]]},{fitresults16[[1,2,1]],fitresults16[[2,2,1]],fitresults16[[3,2,1]],fitresults16[[4,2,1]]}}
{{52.2991,63.3683,54.6572,16.1697},{58.4867,61.9948,35.0588,19.7542},{76.598,68.8301,95.1975,28.9878},{81.918,89.7807,106.301,27.9717},{124.865,136.061,118.434,34.4823},{139.414,168.204,145.223,44.1768},{170.443,204.519,171.651,50.5803},{202.375,231.547,195.194,66.3151},{219.235,255.139,224.137,75.
```

3475},{271.59,282.127,231.19,125.101},{266.107,297.589,226.065,167.843},{2
67.478,300.544,268.251,210.346},{268.628,289.254,251.992,248.468},{273.222,
297.259,237.216,273.223},{268.628,289.254,251.992,248.468},{279.112,289.04
6,237.426,331.204}}
times=3+{0,1,2,4,8,12,16,24,32,64,96,128,184,256,512,1024};
data1=Table[{times[[i]],peaks[[i,1]]},{i,Length[peaks]}];
data2=Table[{times[[i]],peaks[[i,2]]},{i,Length[peaks]}];
data3=Table[{times[[i]],peaks[[i,3]]},{i,Length[peaks]}];
data4=Table[{times[[i]],peaks[[i,4]]},{i,Length[peaks]}];

data1={{3,52.299077187888244`},{4,58.48666413493481`},{5,76.59802407811
868`},{7,81.91802372180065`},{11,124.86456162144778`},{15,139.413636448
40402`},{19,170.44273499402777`},{27,202.37529518345207`},{35,219.23459
369555928`},{67,271.59002299074484`},{99,266.1071639316457`},{131,267.4
784647087372`},{187,268.6275143053802`},{259,273.2215716147031`},{515,2
68.6275143053802`},{1027,279.11189765663556`}}
{{3,52.2991},{4,58.4867},{5,76.598},{7,81.918},{11,124.865},{15,139.414},{1
9,170.443},{27,202.375},{35,219.235},{67,271.59},{99,266.107},{131,267.478
},{187,268.628},{259,273.222},{515,268.628},{1027,279.112}}
data2={{3,63.36826603646284`},{4,61.99479675254041`},{5,68.830100377246
15`},{7,89.78069284939887`},{11,136.06083699565838`},{15,168.2044978198
41`},{19,204.518898183561`},{27,231.54657553518112`},{35,255.1394281684
5287`},{67,282.1266850521707`},{99,297.5885959417525`},{131,300.5438315
514912`},{187,289.25405684893343`},{259,297.25892723782755`},{515,289.2
5405684893343`},{1027,289.0457446659353`}}
{{3,63.3683},{4,61.9948},{5,68.8301},{7,89.7807},{11,136.061},{15,168.204},
{19,204.519},{27,231.547},{35,255.139},{67,282.127},{99,297.589},{131,300.
544},{187,289.254},{259,297.259},{515,289.254},{1027,289.046}}
data3={{3,54.657156733977565`},{4,35.058794435498655`},{5,95.1974571208
0707`},{7,106.3010597127349`},{11,118.43375128965359`},{15,145.22281747
10785`},{19,171.65133645064984`},{27,195.19388170442988`},{35,224.13740
393149416`},{67,231.19045158325113`},{99,226.0649579736889`},{131,268.2
514470956734`},{187,251.99153853745787`},{259,237.21647385553123`},{51
5,251.99153853745787`},{1027,237.42626269544567`}}
{{3,54.6572},{4,35.0588},{5,95.1975},{7,106.301},{11,118.434},{15,145.223},
{19,171.651},{27,195.194},{35,224.137},{67,231.19},{99,226.065},{131,268.2
51},{187,251.992},{259,237.216},{515,251.992},{1027,237.426}}
data4={{3,16.16974049918958`},{4,19.7542232297222`},{5,28.9877690980194
17`},{7,27.97172217869641`},{11,34.482329654138425`},{15,44.17678387308
6244`},{19,50.58027858204367`},{27,66.3150791384562`},{35,75.3475478460
8398`},{67,125.10147149802975`},{99,167.84262883284018`},{131,210.34615
28460374`},{187,248.46768808585594`},{259,273.22329673765853`},{515,248
.46768808585594`},{1027,331.20408176509324`}}

{{3,16.1697},{4,19.7542},{5,28.9878},{7,27.9717},{11,34.4823},{15,44.1768},{19,50.5803},{27,66.3151},{35,75.3475},{67,125.101},{99,167.843},{131,210.346},{187,248.468},{259,273.223},{515,248.468},{1027,331.204}}
peak13={{3,63.67992254005659`},{5,73.67994252649642`},{7,88.71140517411496`},{9,105.07394271625513`},{11,119.38146151090633`},{13,133.77985758016933`},{15,148.18632764020182`},{17,158.8059257598544`},{19,171.94840809236263`},{21,182.52166465809478`},{23,193.68625489315414`},{25,203.38701403494096`},{27,213.99072333382534`},{29,224.07190263970827`},{31,231.5987777799567`},{33,241.791753798344`},{35,250.80851637896723`},{37,258.6544614662544`},{39,265.2664678678872`},{41,273.37269803240855`},{43,281.2731759625969`},{45,289.8046261068042`},{47,297.80877534076734`},{49,300.903603373483`},{51,309.7883674045516`},{53,314.3454966717355`},{63,342.17209700996`},{93,417.6886463382595`},{123,465.82668627552175`},{153,512.6173899924999`},{183,543.5139211485495`},{213,572.1597561108989`},{273,616.263025324103`},{333,644.9867541820247`},{393,666.3399187800294`},{453,677.4474719408263`},{513,686.3058384698897`},{573,695.607328926659 6`},{633,701.5932999506183`},{693,708.3884049562657`},{753,711.3962640160956`},{1003,706.3690744586663`}};

peak14={{3,88.86491868691922`},{5,116.3452509042446`},{7,147.16052805168061`},{9,175.26568825618142`},{11,199.83131815618282`},{13,223.4148387691873`},{15,244.13244808014204`},{17,264.29932195406303`},{19,283.6876358977696`},{21,298.8187821427408`},{23,316.0121882557224`},{25,329.6760279540681`},{27,342.90594731777225`},{29,355.544144612622`},{31,368.0313081112153`},{33,377.73008771263767`},{35,388.918582619285`},{37,396.9903726718298`},{39,407.40608532735416`},{41,414.2885716557534`},{43,423.7550736590172`},{45,430.13589911963413`},{47,436.7099321971243`},{49,445.4022280828689`},{51,449.9469722951525`},{53,456.7024893488286`},{63,485.54060810262166`},{93,534.0484036684212`},{123,562.0294945954533`},{153,571.0462780597956`},{183,580.1440673520476`},{213,584.4437169677082`},{273,588.7507164328808`},{333,592.5709284585936`},{393,600.9254360613273`},{453,612.4474825899589`},{513,602.292132459107`},{573,594.8075544932219`},{633,596.9293375543841`},{693,597.2685386647375`},{753,595.6331351891948`},{1003,593.741497664676`}}
{{3,88.8649},{5,116.345},{7,147.161},{9,175.266},{11,199.831},{13,223.415},{15,244.132},{17,264.299},{19,283.688},{21,298.819},{23,316.012},{25,329.676},{27,342.906},{29,355.544},{31,368.031},{33,377.73},{35,388.919},{37,396.99},{39,407.406},{41,414.289},{43,423.755},{45,430.136},{47,436.71},{49,445.402},{51,449.947},{53,456.702},{63,485.541},{93,534.048},{123,562.029},{153,571.046},{183,580.144},{213,584.444},{273,588.751},{333,592.571},{393,600.925},{453,612.447},{513,602.292},{573,594.808},{633,596.929},{693,597.269},{753,595.633},{1003,593.741}}
fit=FindFit[data1,{A(1-Exp[-t*Rb]),{0.1≥Rb≥0.001,300≥A≥200}},{A,Rb},t]
{A→270.839,Rb→0.0529367}

Plot[A(1-Exp[-t*Rb])/.fit,{t,0,1000},PlotRange→ All];
ListPlot[data1];
Show[%%,%]

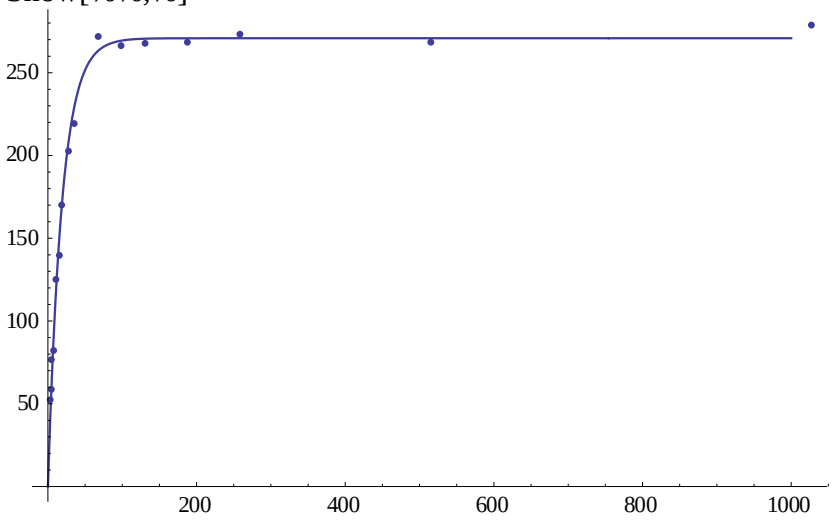

fit=FindFit[data4,{A(1-Exp[-t*Rb]),{0.01≥Rb≥0.001,500≥A≥200}},{A,Rb},t]
{A→295.41,Rb→0.00910139}
Plot[A(1-Exp[-t*Rb])/.fit,{t,0,1000},PlotRange→ All];
ListPlot[data4];
Show[%%,%]

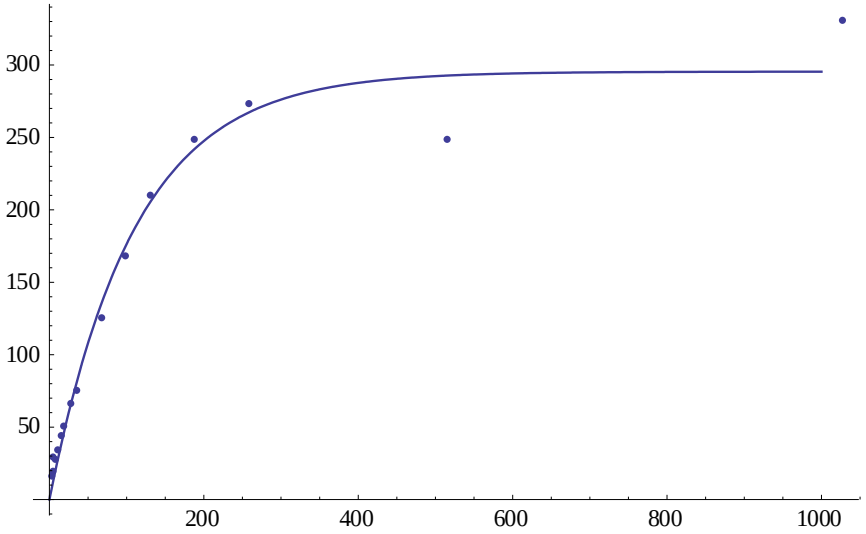

A2. Mathematica Codes for Global Fitting of 9-MA Spin Diffusion Rates

```
$DefaultFont={"Times-Italic",18};
sol=DSolve[{D[a[t],t]==-k (1-Xa)(a[t])-R1a (a[t]-Xa) + Xa k (b[t]) ,D[b[t],t]==-k Xa(b[t])-
R1b (b[t]-1+Xa) +  k  (1-Xa)(a[t]) ,a[0]==0,b[0]==0},{a[t],b[t]},t]//FullSimplify

{{a[t]→1/(2 Sqrt[1024 R1a R1b^2-4096 R1a R1b Xa]
 E^(1/2 t (1024 R1a R1b-Sqrt[1024 R1a R1b^2-4096 R1a R1b Xa])) Xa (1024-
R1a+R1b-Sqrt[1024 R1a R1b^2-4096 R1a R1b Xa]+2
 E^(1/2 t (1024 R1a R1b+Sqrt[1024 R1a R1b^2-4096 R1a R1b Xa])) Xa
Sqrt[1024 R1a R1b^2-4096 R1a R1b Xa]-
 E^(t Sqrt[1024 R1a R1b^2-4096 R1a R1b Xa]) (1024-R1a+R1b+
Sqrt[1024 R1a R1b^2-4096 R1a R1b Xa])),b[t]→1/(2
Sqrt[1024 R1a R1b^2-4096 R1a R1b Xa]
 E^(1/2 t (1024 R1a R1b-Sqrt[1024 R1a R1b^2-4096 R1a R1b Xa])) (-1+Xa) (-1024-
R1a+R1b+Sqrt[1024 R1a R1b^2-4096 R1a R1b Xa]-2
 E^(1/2 t (1024 R1a R1b+Sqrt[1024 R1a R1b^2-4096 R1a R1b Xa])) Xa
Sqrt[1024 R1a R1b^2-4096 R1a R1b Xa]+
 E^(t Sqrt[1024 R1a R1b^2-4096 R1a R1b Xa]) (1024+R1a-R1b+
Sqrt[1024 R1a R1b^2-4096 R1a R1b Xa]))}}
sol[[1]]

{a[t]→1/(2 Sqrt[1024 R1a R1b^2-4096 R1a R1b Xa]
 E^(1/2 t (1024 R1a R1b-Sqrt[1024 R1a R1b^2-4096 R1a R1b Xa])) Xa (1024-
R1a+R1b-Sqrt[1024 R1a R1b^2-4096 R1a R1b Xa]+2
```

$$e^{\frac{1}{2}t\left(1024\,R1a\,R1b\sqrt{|1024\,R1a\,R1b|^2-4096|R1a\,R1b|\,Xa}\right)}\sqrt{|1024\,R1a\,R1b|^2-4096|R1a\,R1b|\,Xa}-t\sqrt{|1024\,R1a\,R1b|^2-4096|R1a\,R1b|\,Xa}\,(1024-R1a+R1b+\sqrt{|1024\,R1a\,R1b|^2-4096|R1a\,R1b|\,Xa}))$$

$$,b[t]\to 1/(2\sqrt{|1024\,R1a\,R1b|^2-4096|R1a\,R1b|\,Xa})\,e^{\frac{1}{2}t\left(1024\,R1a\,R1b\sqrt{|1024\,R1a\,R1b|^2-4096|R1a\,R1b|\,Xa}\right)}(-1+Xa)\,(-1024-R1a+R1b+\sqrt{|1024\,R1a\,R1b|^2-4096|R1a\,R1b|\,Xa}-2e^{\frac{1}{2}t\left(1024\,R1a\,R1b\sqrt{|1024\,R1a\,R1b|^2-4096|R1a\,R1b|\,Xa}\right)}\sqrt{|1024\,R1a\,R1b|^2-4096|R1a\,R1b|\,Xa}+t\sqrt{|1024\,R1a\,R1b|^2-4096|R1a\,R1b|\,Xa}\,(1024+R1a-R1b+\sqrt{|1024\,R1a\,R1b|^2-4096|R1a\,R1b|\,Xa}))\}$$

Now to fit some data

$$a[k\_,R1a\_,R1b\_,Xa\_,Ao\_,t\_]:=Ao\,(e^{\frac{1}{2}t\left(k\,R1a\,R1b\sqrt{|k\,R1a\,R1b|^2+4k|R1a\,R1b|\,Xa}\right)}Xa\,(-(-1+e^{t\sqrt{|k\,R1a\,R1b|^2+4k|R1a\,R1b|\,Xa}})\,(k-R1a+R1b)-\sqrt{|k\,R1a\,R1b|^2+4k|R1a\,R1b|\,Xa}-e^{t\sqrt{|k\,R1a\,R1b|^2+4k|R1a\,R1b|\,Xa}}\sqrt{|k\,R1a\,R1b|^2+4k|R1a\,R1b|\,Xa}+2e^{\frac{1}{2}t\left(k\,R1a\,R1b\sqrt{|k\,R1a\,R1b|^2+4k|R1a\,R1b|\,Xa}\right)}\sqrt{|k\,R1a\,R1b|^2+4k|R1a\,R1b|\,Xa}))/(2\sqrt{|k\,R1a\,R1b|^2+4k|R1a\,R1b|\,Xa})$$

b[k_,R1a_,R1b_,Xa_,Ao_,t_]:=Ao

$$\left(e^{-\frac{1}{2}t\left(k+R1a+R1b-\sqrt{(k+R1a+R1b)^2+4k(-R1a+R1b)Xa}\right)}(-1+Xa)\left((-1+e^{t\sqrt{(k+R1a+R1b)^2+4k(-R1a+R1b)Xa}}\right)(k+R1a-R1b)+\sqrt{(k+R1a+R1b)^2+4k(-R1a+R1b)Xa}+e^{t\sqrt{(k+R1a+R1b)^2+4k(-R1a+R1b)Xa}}\sqrt{(k+R1a+R1b)^2+4k(-R1a+R1b)Xa}-2e^{\frac{1}{2}t\left(k+R1a+R1b-\sqrt{(k+R1a+R1b)^2+4k(-R1a+R1b)Xa}\right)}\sqrt{(k+R1a+R1b)^2+4k(-R1a+R1b)Xa}\right)\Big/\left(2\sqrt{(k+R1a+R1b)^2+4k(-R1a+R1b)Xa}\right)$$

peak11={{3,15.44766553870049`},{4,18.45125572103406`},{5,23.921994939977626`}
,{7,28.47025822463529`},{11,41.196871650556055`},{15,58.084433357578774`},{19,
69.42995294172141`},{27,94.83758665242162`},{35,121.75100138264362`},{67,188.7
5451411738752`},{99,254.71470438921924`},{131,300.6702948139399`},{187,355.54
68652816717`},{259,401.19647565253683`},{515,469.4510307832143`},{1027,477.61
607996866337`}}
{{3,15.4477},{4,18.4513},{5,23.922},{7,28.4703},{11,41.1969},{15,58.0844},{19,69.4
3},{27,94.8376},{35,121.751},{67,188.755},{99,254.715},{131,300.67},{187,355.547},
{259,401.196},{515,469.451},{1027,477.616}}
peak1={{3,4.68162880101393`},{4,15.090933576180005`},{5,24.07030298705888`},{
7,35.895356540683295`},{11,43.90902491936202`},{15,59.98670861578898`},{19,63.
83195343991805`},{27,94.61986268163264`},{35,96.5528536181859`},{67,188.57683
112780936`},{99,235.6997311663308`},{131,290.2528156505459`},{187,345.1567297
4488456`},{259,412.9284022444757`},{515,472.8674632200033`}}
{{3,4.68163},{4,15.0909},{5,24.0703},{7,35.8954},{11,43.909},{15,59.9867},{19,63.8
32},{27,94.6199},{35,96.5529},{67,188.577},{99,235.7},{131,290.253},{187,345.157},
{259,412.928},{515,472.867}}
peak2={{3,81.59335640143043`},{4,83.75315709283349`},{5,92.3894536823155`},{7,
116.11375435388085`},{11,147.0233955529719`},{15,178.35667858159763`},{19,189.
991939278026`},{27,223.7206555318535`},{35,216.65942738264556`},{67,234.96657
579606472`},{99,239.4631950009863`},{131,217.0530745916864`},{187,218.5112415
9503544`},{259,215.7400788169935`},{515,223.25895591534618`}}
{{3,81.5934},{4,83.7532},{5,92.3895},{7,116.114},{11,147.023},{15,178.357},{19,189
.992},{27,223.721},{35,216.659},{67,234.967},{99,239.463},{131,217.053},{187,218.
511},{259,215.74},{515,223.259}}

peak3={{3,16.16974049918958`},{4,19.7542232297222`},{5,28.987769098019417`},{7,27.97172217869641`},{11,34.482329654138425`},{15,44.176783873086244`},{19,50.58027858204367`},{27,66.3150791384562`},{35,75.34754784608398`},{67,125.10147149802975`},{99,167.84262883284018`},{131,210.3461528460374`},{187,248.46768808585594`},{259,273.22329673765853`},{515,248.46768808585594`}}
{{3,16.1697},{4,19.7542},{5,28.9878},{7,27.9717},{11,34.4823},{15,44.1768},{19,50.5803},{27,66.3151},{35,75.3475},{67,125.101},{99,167.843},{131,210.346},{187,248.468},{259,273.223},{515,248.468}}
peak4={{3,52.299077187888244`},{4,58.48666413493481`},{5,76.59802407811868`},{7,81.91802372180065`},{11,124.86456162144778`},{15,139.41363644840402`},{19,170.44273499402777`},{27,202.37529518345207`},{35,219.23459369555928`},{67,271.59002299074484`},{99,266.1071639316457`},{131,267.4784647087372`},{187,268.6275143053802`},{259,273.2215716147031`},{515,268.6275143053802`}}
{{3,52.2991},{4,58.4867},{5,76.598},{7,81.918},{11,124.865},{15,139.414},{19,170.443},{27,202.375},{35,219.235},{67,271.59},{99,266.107},{131,267.478},{187,268.628},{259,273.222},{515,268.628}}
peak5={{3,13.174274692458084`},{4,29.48942724152037`},{5,14.086947763876701`},{7,27.86536557498547`},{11,41.989151941178`},{15,36.399418703139105`},{19,60.033494646378145`},{27,77.27310642817186`},{35,100.60752517874909`},{67,168.0638149611842`},{99,212.93011147406693`},{131,256.89307133502575`},{187,318.7525210705924`},{259,359.426919645587`},{515,425.9822608213043`}}
{{3,13.1743},{4,29.4894},{5,14.0869},{7,27.8654},{11,41.9892},{15,36.3994},{19,60.0335},{27,77.2731},{35,100.608},{67,168.064},{99,212.93},{131,256.893},{187,318.753},{259,359.427},{515,425.982}}
peak6={{3,77.15347497644629`},{4,101.84989203684297`},{5,116.86345761434447`},{7,148.85459577925496`},{11,201.44601668800036`},{15,217.91389769489118`},{19,259.0818833648827`},{27,288.78206512209164`},{35,322.49235878251943`},{67,360.942495366732`},{99,369.11106178063096`},{131,362.36115799028846`},{187,369.6448864308809`},{259,365.2034774650458`},{515,375.19445283539864`}}
{{3,77.1535},{4,101.85},{5,116.863},{7,148.855},{11,201.446},{15,217.914},{19,259.082},{27,288.782},{35,322.492},{67,360.942},{99,369.111},{131,362.361},{187,369.645},{259,365.203},{515,375.194}}
peak7={{3,5.896099393423542`},{4,14.381675565540636`},{5,9.804256316608127`},{7,5.470233081532538`},{11,15.364902228776769`},{19,29.309890154486652`},{35,55.76948328788643`},{67,95.5152201184232`},{131,128.80944182215364`},{259,189.20576825514863`},{515,212.17326416411402`}}
{{3,5.8961},{4,14.3817},{5,9.80426},{7,5.47023},{11,15.3649},{19,29.3099},{35,55.7695},{67,95.5152},{131,128.809},{259,189.206},{515,212.173}}
peak8={{3,58.24307595100102`},{4,68.24869650162073`},{5,90.81346340031041`},{7,112.83791912012754`},{11,151.72690884940354`},{19,208.7553431152611`},{35,263.47137673863176`},{67,314.90804384717137`},{131,370.34633417479444`},{259,373.29764774353924`},{515,369.09835956341794`}}
{{3,58.2431},{4,68.2487},{5,90.8135},{7,112.838},{11,151.727},{19,208.755},{35,263.471},{67,314.908},{131,370.346},{259,373.298},{515,369.098}}

peak9={{3,2.765320540104988`},{4,3.9067268691084887`},{5,9.934067771583445`},{7,11.260599772754338`},{11,30.4125490280001`},{15,23.128375883160157`},{19,30.64128146090886`},{27,38.87804267032317`},{35,49.908475095006295`},{67,84.90074293879078`},{99,100.0689042592839`},{131,100.83279204170462`},{187,147.65756070643778`},{259,143.8314052811532`},{515,186.6119121125925`}}
{{3,2.76532},{4,3.90673},{5,9.93407},{7,11.2606},{11,30.4125},{15,23.1284},{19,30.6413},{27,38.878},{35,49.9085},{67,84.9007},{99,100.069},{131,100.833},{187,147.658},{259,143.831},{515,186.612}}
peak10={{3,70.53830419998057`},{4,81.92309970892548`},{5,110.4475933234359`},{7,126.62010048940404`},{11,172.80629929819352`},{15,202.01221704548658`},{19,227.13199485607794`},{27,258.83014245065107`},{35,287.95825445409247`},{67,329.46443356773824`},{99,340.18795173334803`},{131,354.86595237620105`},{187,352.8798443845793`},{259,344.7333299696665`},{515,366.2205982733698`}}
{{3,70.5383},{4,81.9231},{5,110.448},{7,126.62},{11,172.806},{15,202.012},{19,227.132},{27,258.83},{35,287.958},{67,329.464},{99,340.188},{131,354.866},{187,352.88},{259,344.733},{515,366.221}}

chisq[R1a_,R1b_,k1_,X1a_,A1o_,A11_,k2_,X2a_,A2o_,A21_,k3_,X3a_,A3o_,A31_,k4_,X4a_,A4o_,A41_,k5_,X5a_,A5o_,A51_]:=Sum[(a[k1,R1a,R1b,X1a,A1o,peak1[[i,1]]]-peak1[[i,2]])^2+(b[k1,R1a,R1b,X1a,A11,peak2[[i,1]]]-peak2[[i,2]])^2,{i,1,Length[peak2]}]+Sum[(a[k2,R1a,R1b,X2a,A2o,peak3[[i,1]]]-peak3[[i,2]])^2+(b[k2,R1a,R1b,X2a,A21,peak4[[i,1]]]-peak4[[i,2]])^2,{i,1,Length[peak4]}]+Sum[(a[k3,R1a,R1b,X3a,A3o,peak5[[i,1]]]-peak5[[i,2]])^2+(b[k3,R1a,R1b,X3a,A31,peak6[[i,1]]]-peak6[[i,2]])^2,{i,1,Length[peak6]}]+Sum[(a[k4,R1a,R1b,X4a,A4o,peak7[[i,1]]]-peak7[[i,2]])^2+(b[k4,R1a,R1b,X4a,A41,peak8[[i,1]]]-peak8[[i,2]])^2,{i,1,Length[peak8]}]+Sum[(a[k5,R1a,R1b,X5a,A5o,peak9[[i,1]]]-peak9[[i,2]])^2+(b[k5,R1a,R1b,X5a,A51,peak10[[i,1]]]-peak10[[i,2]])^2,{i,1,Length[peak10]}]
X1a=0.69
X2a=0.58
X3a=0.54
X4a=0.41
X5a=0.38
0.69
0.58
0.54
0.41
0.38
{chisqval,bestfit}=FindMinimum[{chisq[0.007716782256077797`,R1b,k1,X1a,A1o,A11,k2,X2a,A2o,A21,k3,X3a,A3o,A31,k4,X4a,A4o,A41,k5,X5a,A5o,A51],R1b≥0,1≥k1≥0,1≥k2≥0,1≥k3≥0,1≥k4≥0,1≥k5≥0},{R1b,0.065},{k1,0.005},{A1o,725},{A11,626}

,{k2,0.005},{A2o,634},{A21,517},{k3,0.001},{A3o,956},{A31,605},{k4,0.01},{A4o,550},{A41,535},{k5,0.01},{A5o,550},{A51,500}]
{25941.1,{R1b→0.063367,k1→4.17596?10^-11,A1o→677.71,A11→780.514,k2→0.0118257,A2o→460.345,A21→641.389,k3→7.71016?10^-11,A3o→775.754,A31→801.788,k4→0.00563001,A4o→485.379,A41→583.02,k5→0.00206686,A5o→460.661,A51→555.064}}

Plot[(a[k1,0.007716782256077797`,R1b,X1a,A1o,t])/.bestfit,{t,0,600},PlotRange→All,PlotStyle→{Thickness[0.005],Black}];
ListPlot[peak1,PlotStyle→{PointSize[Large],Red,Opacity[0.7]}];
Show[%%,%, Frame→ True]

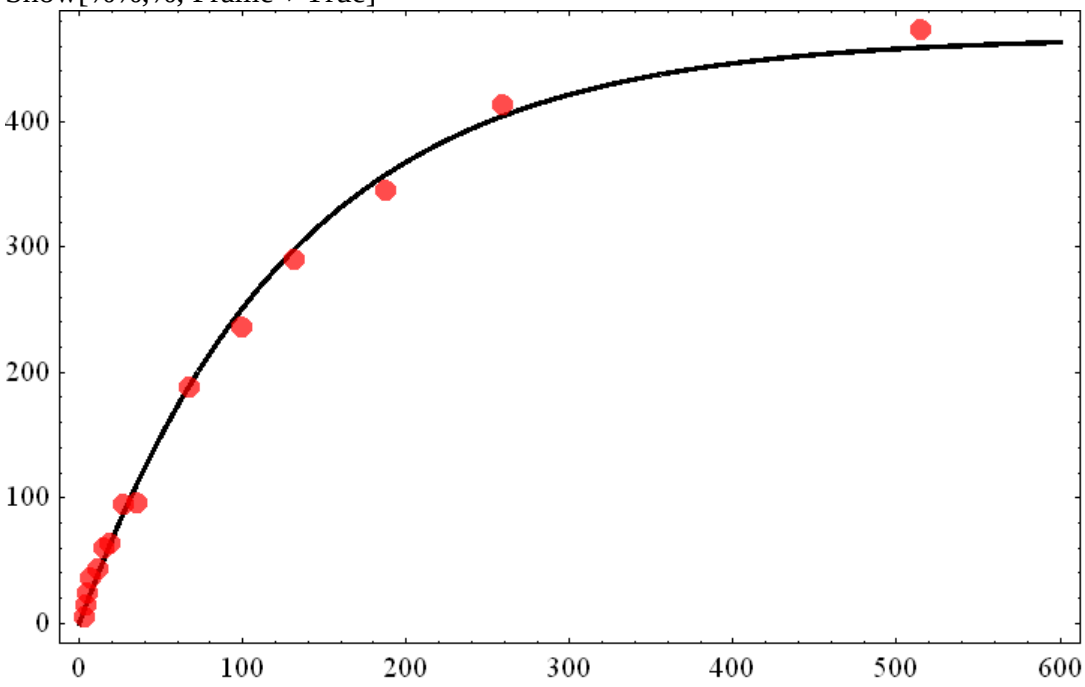

Plot[(b[k1,0.007716782256077797`,R1b,X1a,A11,t])/.bestfit,{t,0,600},PlotRange→All,PlotStyle→{Thickness[0.005],Black}];
ListPlot[peak2,PlotStyle→{PointSize[Large],Red,Opacity[0.7]}];
Show[%%,%, Frame→ True]

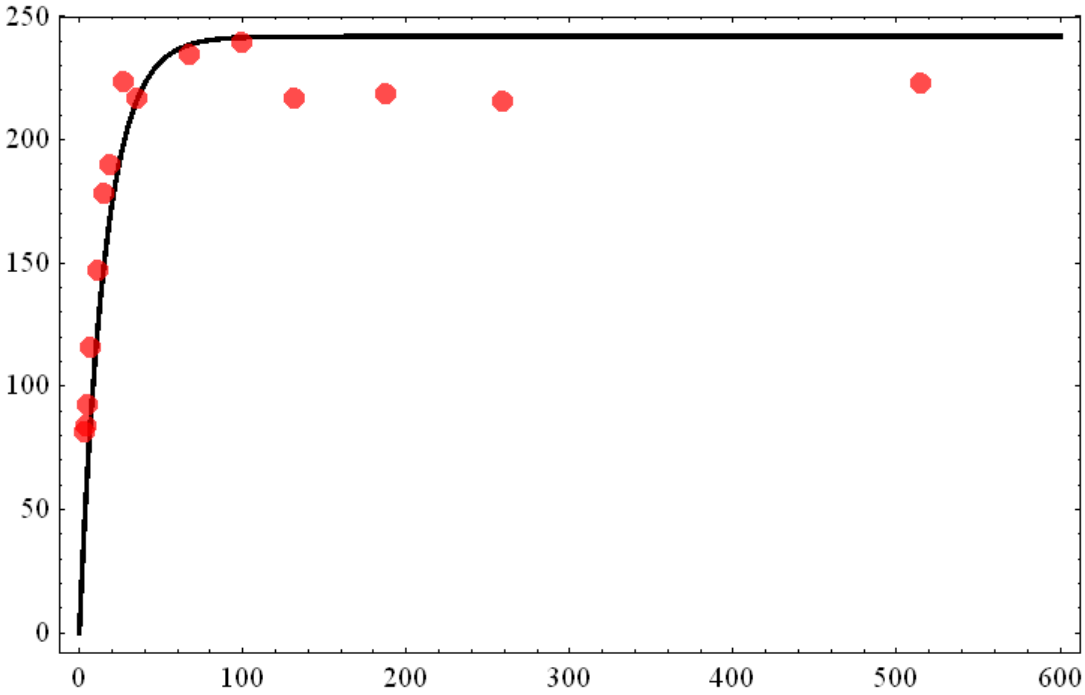


```
Plot[(a[k2,0.007716782256077797`,R1b,X2a,A2o,t])/.bestfit,{t,0,600},PlotRange→All,Pl
otStyle→{Thickness[0.005],Black}];
ListPlot[peak3,PlotStyle→{PointSize[Large],Red,Opacity[0.7]}];
Show[%%,%, Frame→ True]
```

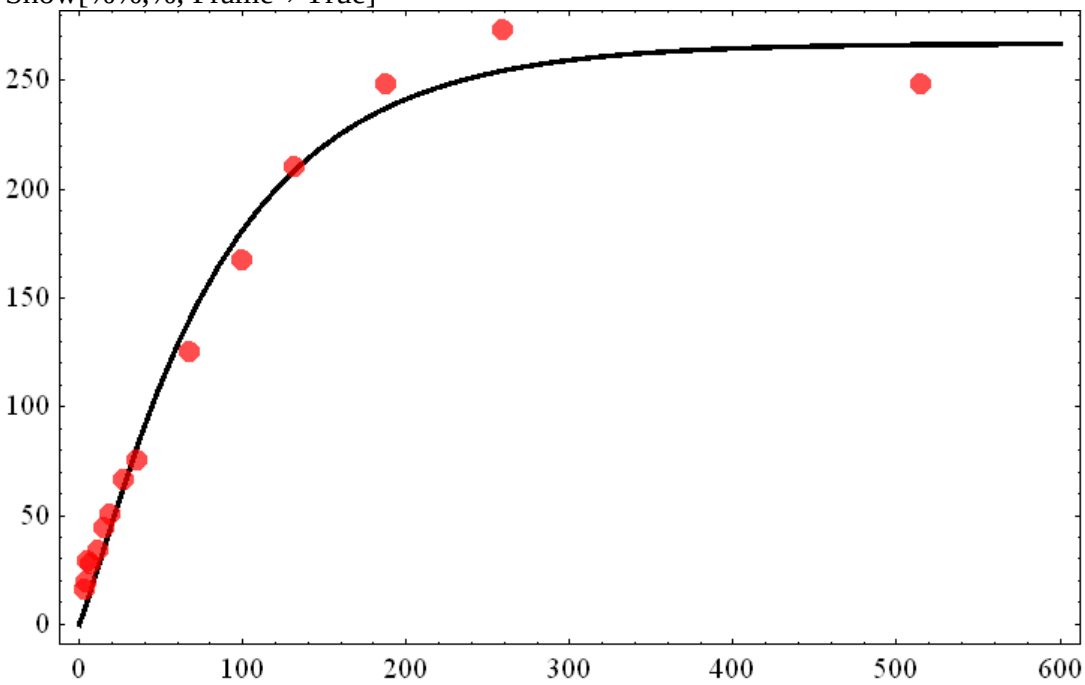


```
Plot[(b[k2,0.007716782256077797`,R1b,X2a,A21,t])/.bestfit,{t,0,600},PlotRange→All,Pl
otStyle→{Thickness[0.005],Black}];
```

ListPlot[peak4,PlotStyle→{PointSize[Large],Red,Opacity[0.7]}];
Show[%%,%, Frame→ True]

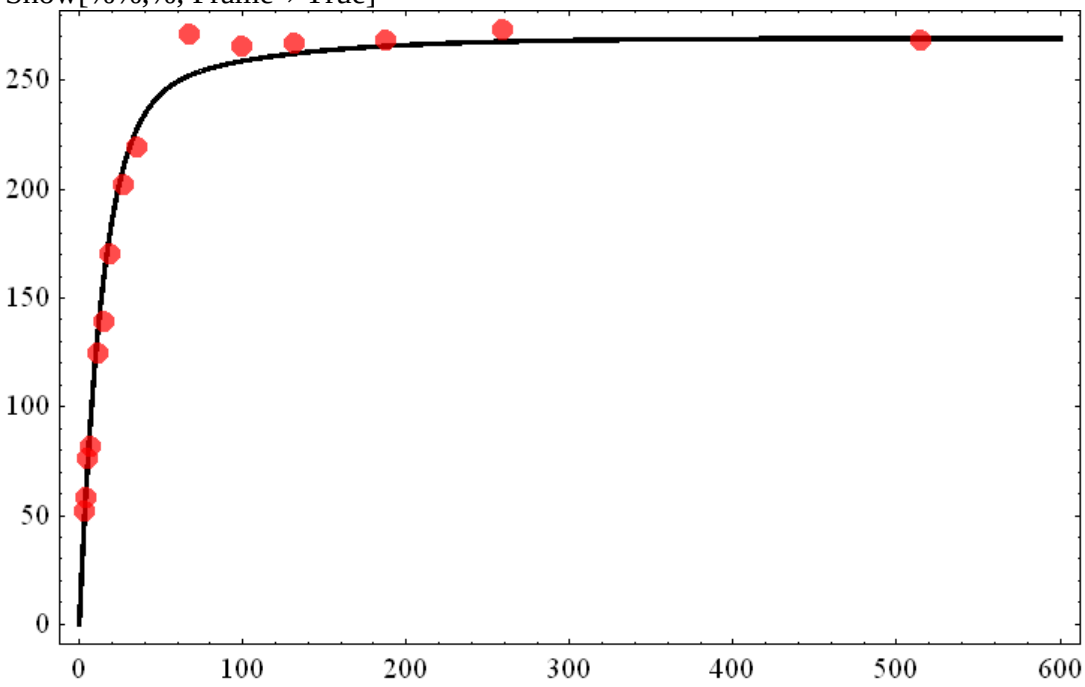

Plot[(a[k3,0.007716782256077797`,R1b,X3a,A3o,t])/.bestfit,{t,0,600},PlotRange→All,PlotStyle→{Thickness[0.005],Black}];
ListPlot[peak5,PlotStyle→{PointSize[Large],Red,Opacity[0.7]}];
Show[%%,%, Frame→ True]

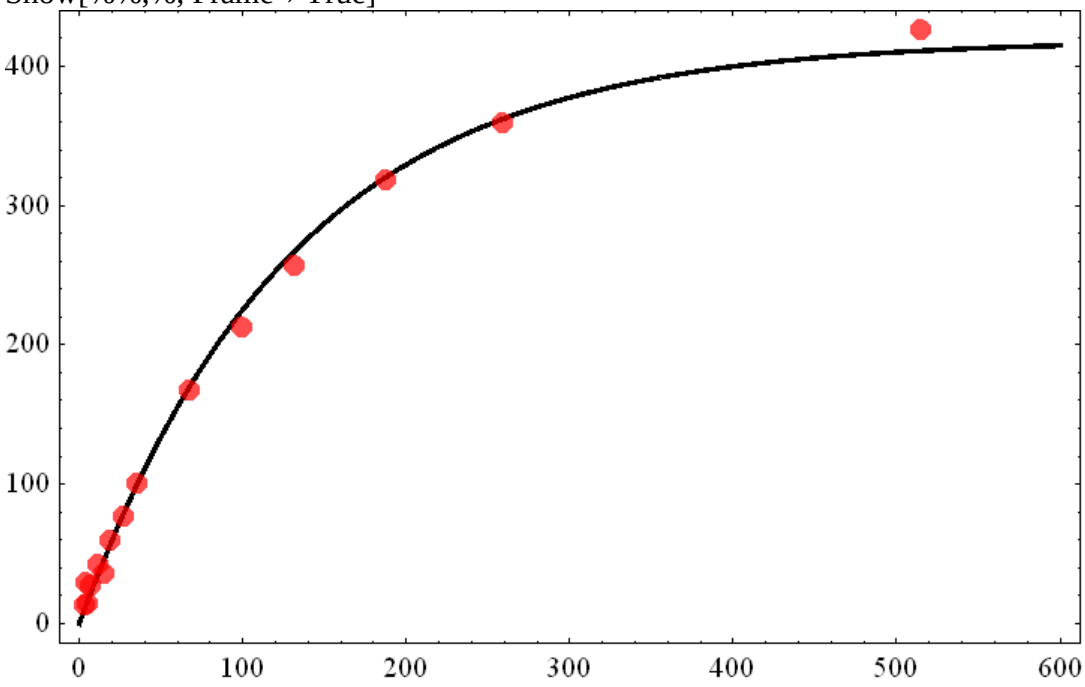

bestfit

{R1b→0.063367,k1→4.17596?10^-11,A1o→677.71,A11→780.514,k2→0.0118257,A2o→460.345,A21→641.389,k3→7.71016?10^-11,A3o→775.754,A31→801.788,k4→0.00563001,A4o→485.379,A41→583.02,k5→0.00206686,A5o→460.661,A51→555.064}

```
Plot[(b[k3,0.007716782256077797`,R1b,X3a,A31,t])/.bestfit,{t,0,600},PlotRange→All,PlotStyle→{Thickness[0.005],Black}];
ListPlot[peak6,PlotStyle→{PointSize[Large],Red,Opacity[0.7]}];
Show[%%,%, Frame→ True]
```

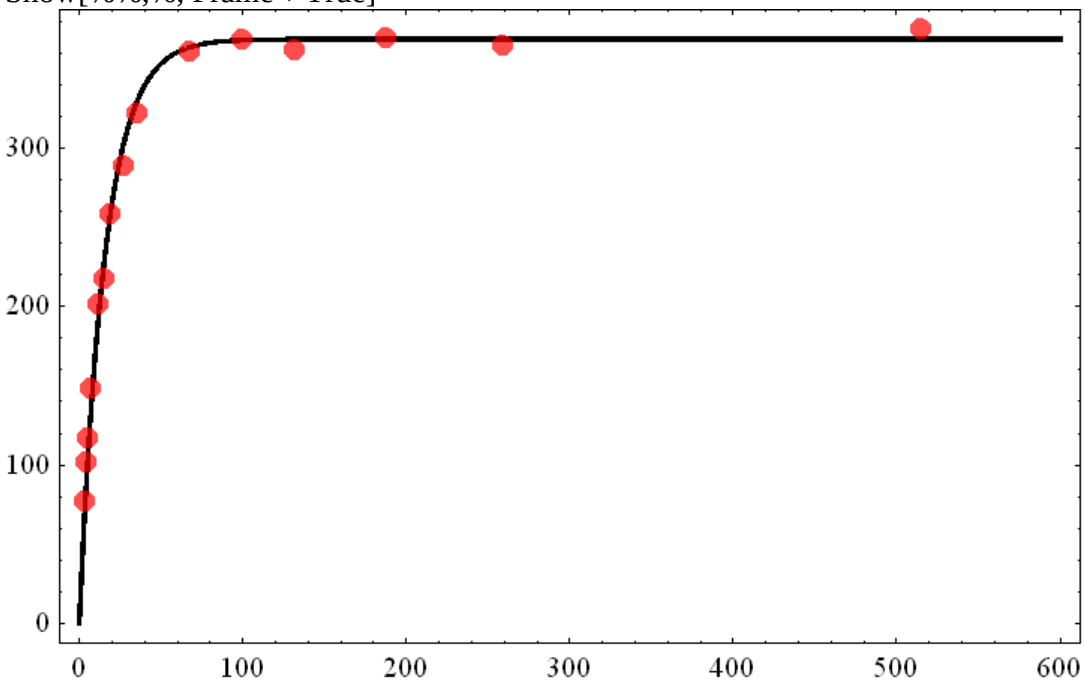


```
Plot[(a[k4,0.007716782256077797`,R1b,X4a,A4o,t])/.bestfit,{t,0,600},PlotRange→All,PlotStyle→{Thickness[0.005],Black}];
ListPlot[peak7,PlotStyle→{PointSize[Large],Red,Opacity[0.7]}];
Show[%%,%, Frame→ True]
```

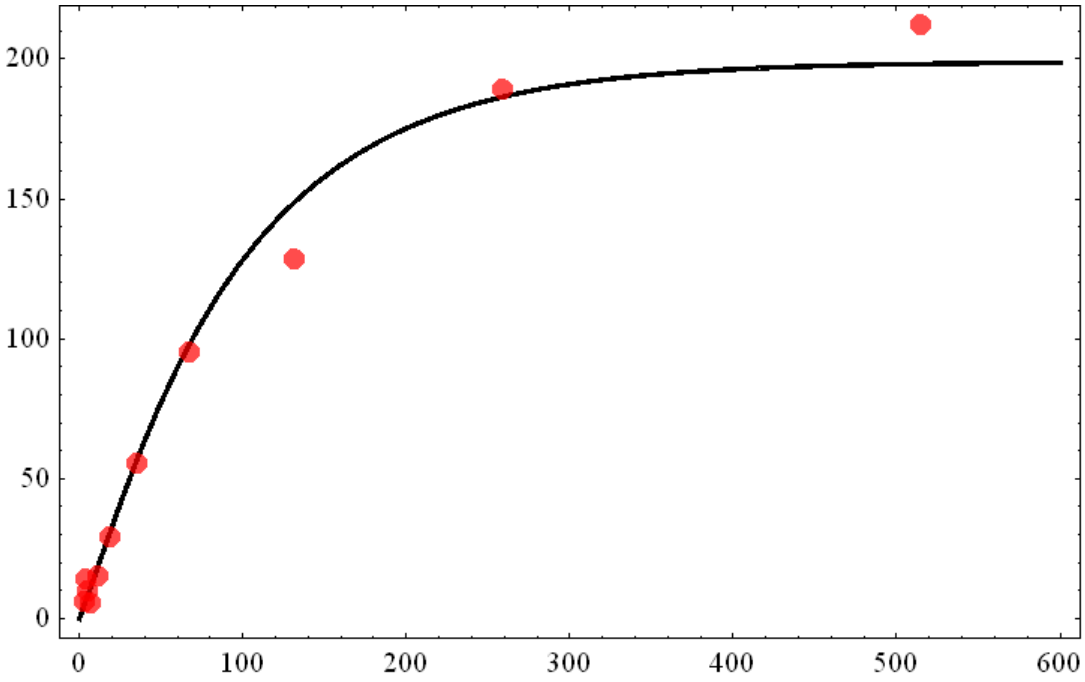


```
Plot[(b[k4,0.007716782256077797`,R1b,X4a,A41,t])/.bestfit,{t,0,600},PlotRange→All,Pl
otStyle→{Thickness[0.005],Black}];
ListPlot[peak8,PlotStyle→{PointSize[Large],Red,Opacity[0.7]}];
Show[%%,%, Frame→ True]
```

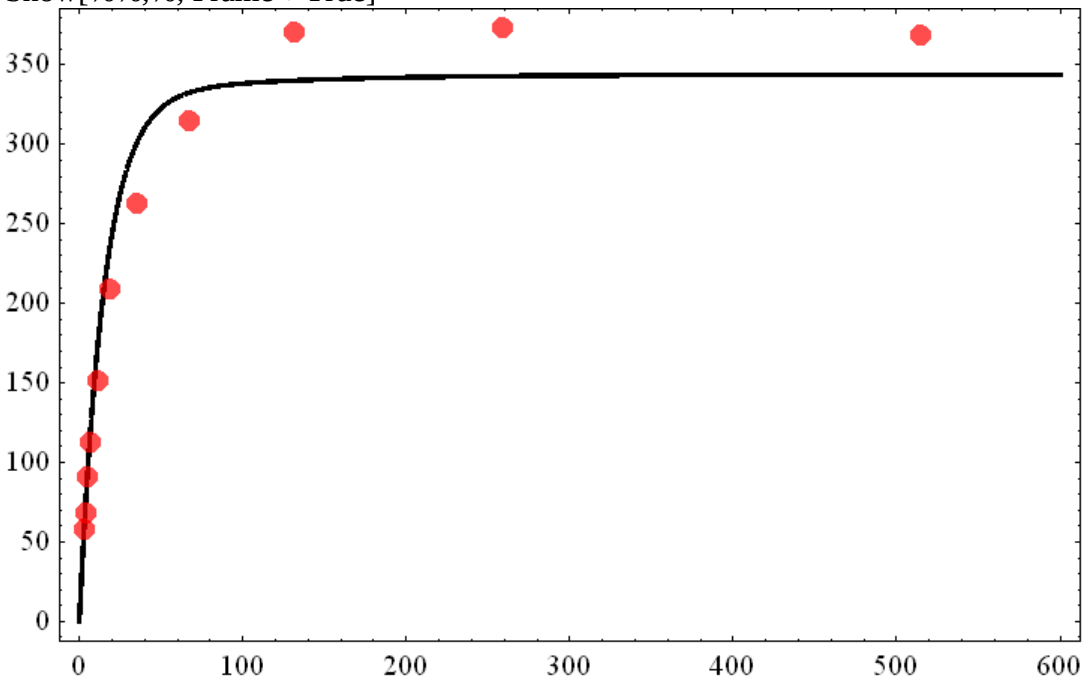


```
Plot[(a[k5,0.007716782256077797`,R1b,X5a,A5o,t])/.bestfit,{t,0,600},PlotRange→All,Pl
otStyle→{Thickness[0.005],Black}];
ListPlot[peak9,PlotStyle→{PointSize[Large],Red,Opacity[0.7]}];
```

Show[%%,%, Frame→ True]

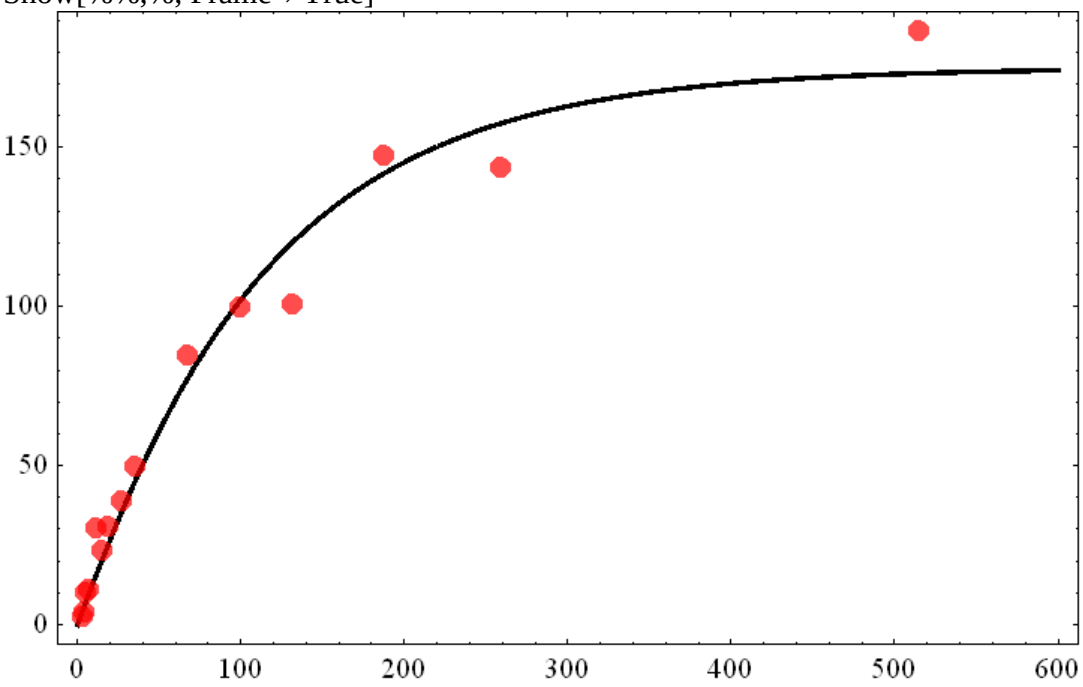

Plot[(b[k5,0.007716782256077797`,R1b,X5a,A51,t])/.bestfit,{t,0,600},PlotRange→All,PlotStyle→{Thickness[0.005],Black}];
ListPlot[peak10,PlotStyle→{PointSize[Large],Red,Opacity[0.7]}];
Show[%%,%, Frame→ True]

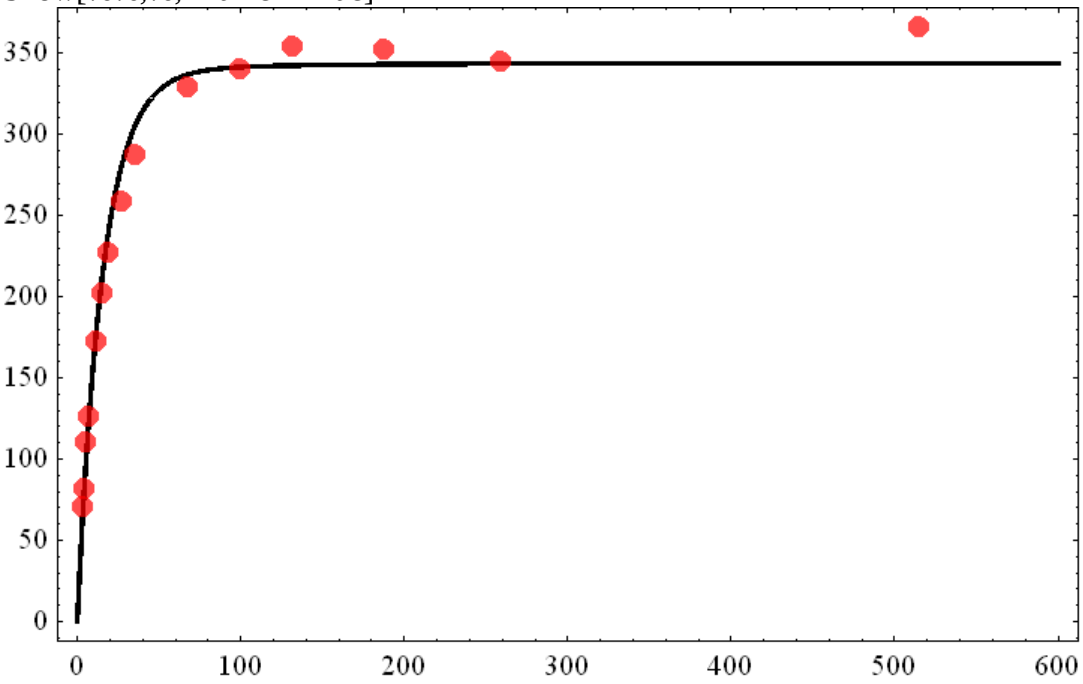

A3. Mathematica Codes for Showing the Range of 9-MA Spin Diffusion Rates

```
peak1n=Table[{peak1[[i,1]],peak1[[i,2]]/peak1[[Length[peak1],2]]},{i,Length[peak1]}];
peak3n=Table[{peak3[[i,1]],peak3[[i,2]]/1.2/peak3[[Length[peak3]-
1,2]]},{i,Length[peak3]-1}];
peak5n=Table[{peak5[[i,1]],peak5[[i,2]]/peak5[[Length[peak5],2]]},{i,Length[peak5]}];
peak7n=Table[{peak7[[i,1]],peak7[[i,2]]/peak7[[Length[peak7],2]]},{i,Length[peak7]}];
peak9n=Table[{peak9[[i,1]],peak9[[i,2]]/peak9[[Length[peak9],2]]},{i,Length[peak9]}];
ListPlot[{peak1n,peak3n,peak5n,peak7n,peak9n},Joined→
True ,PlotStyle→{Thickness[0.003]}]
```

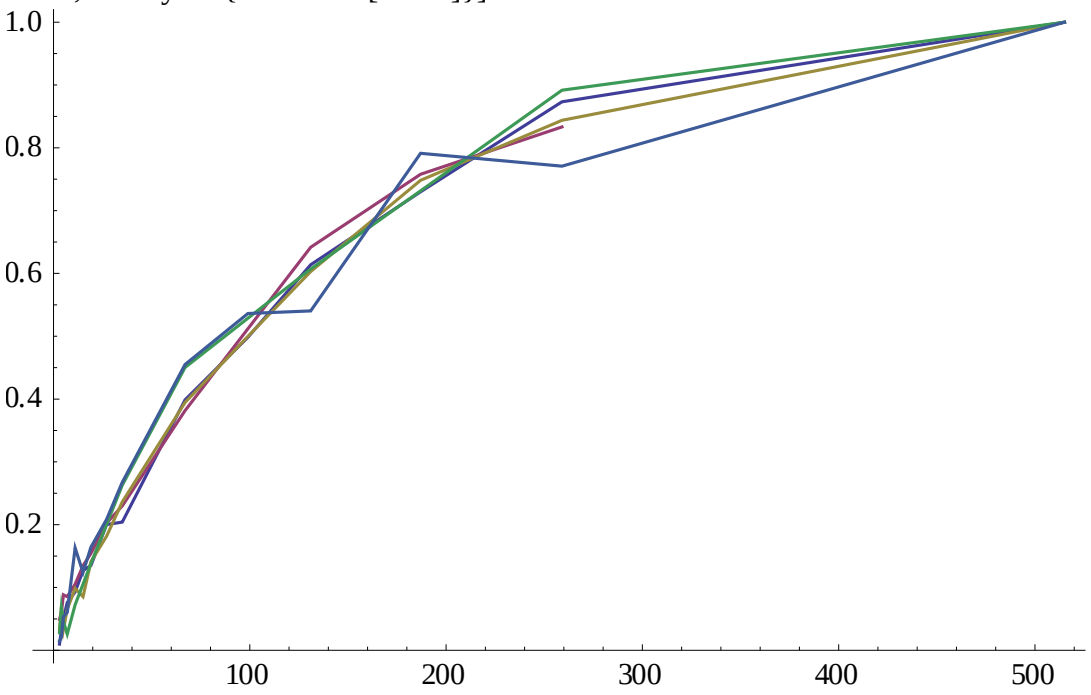


```
Plot[Table[(a[k,0.0077,0.065,0.4,1,t]/a[k,0.0077,0.065,0.4,1,10000]),{k,0.002,0.01,0.004
}],{t,0,600},PlotRange→All,PlotStyle→{Thickness[0.003],Black,Dashing[Small]}]
```

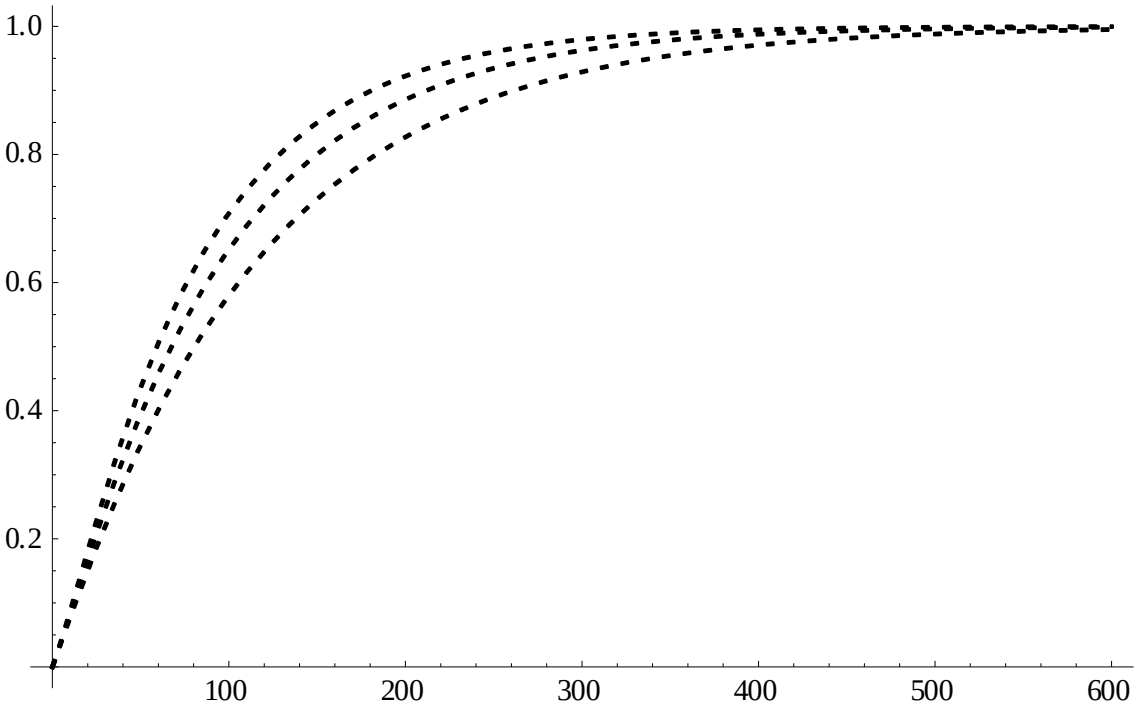

Show[%171,%181, Frame→ True]

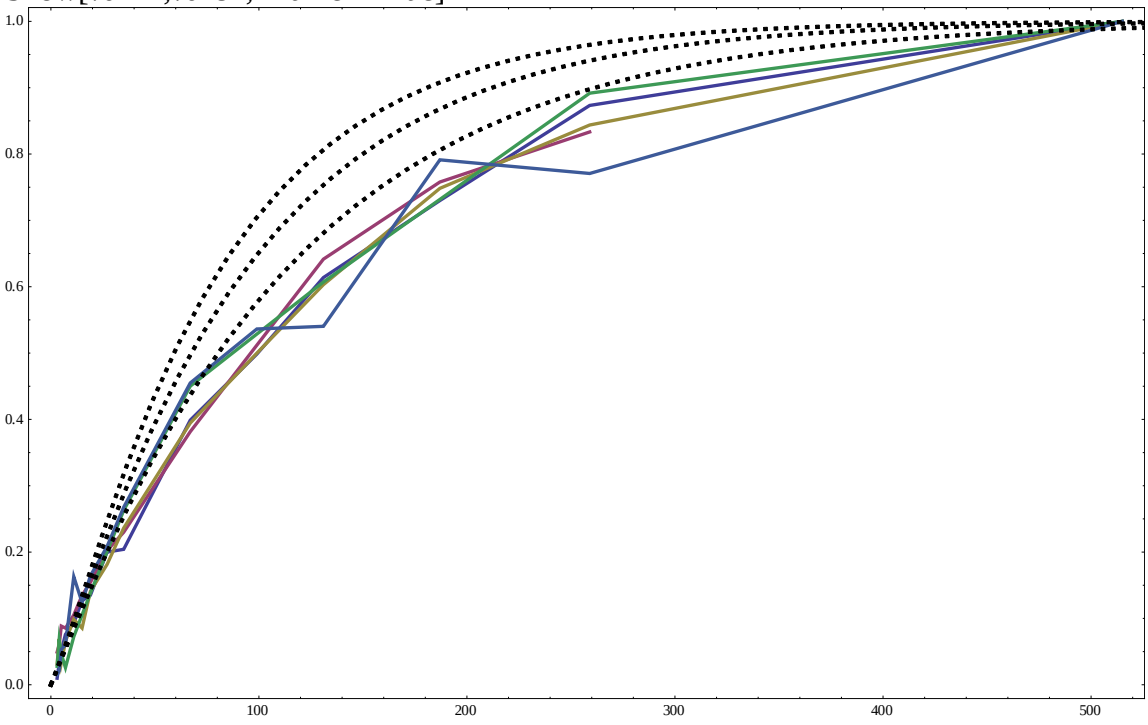

```
peak2n=Table[{peak2[[i,1]],peak2[[i,2]]/1.1/peak2[[Length[peak2],2]]},{i,Length[peak2
]}];
peak4n=Table[{peak4[[i,1]],peak4[[i,2]]/peak4[[Length[peak4]-1,2]]},{i,Length[peak4]-
1}];
peak6n=Table[{peak6[[i,1]],peak6[[i,2]]/peak6[[Length[peak6],2]]},{i,Length[peak6]}];
peak8n=Table[{peak8[[i,1]],peak8[[i,2]]/peak8[[Length[peak8],2]]},{i,Length[peak8]}];
peak10n=Table[{peak10[[i,1]],peak10[[i,2]]/peak10[[Length[peak10],2]]},{i,Length[pea
k10]}];
ListPlot[{peak2n,peak4n,peak6n,peak8n,peak10n},Joined-
>True,PlotStyle→{Thickness[0.003]}]
```

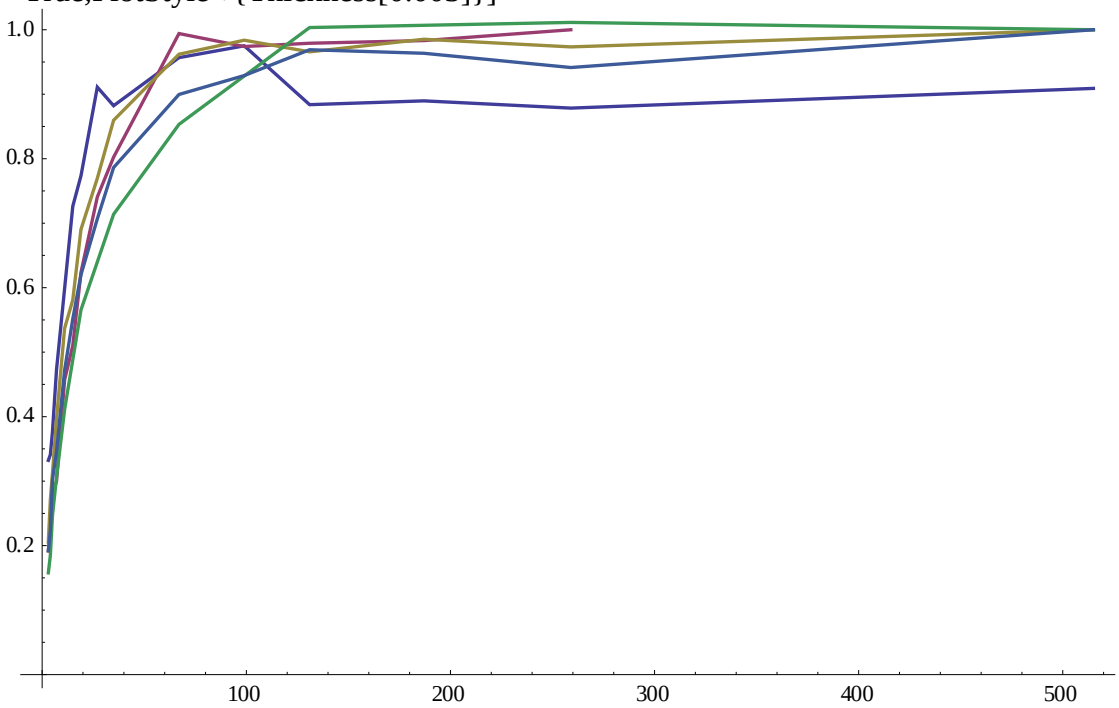


```
Plot[Table[(b[k,0.0077,0.065,0.4,1,t]/b[k,0.0077,0.065,0.4,1,10000]),{k,0.002,0.01,0.004
}],{t,0,600},PlotRange→All,PlotStyle→{Thickness[0.003],Black,Dashing[Small]}]
```

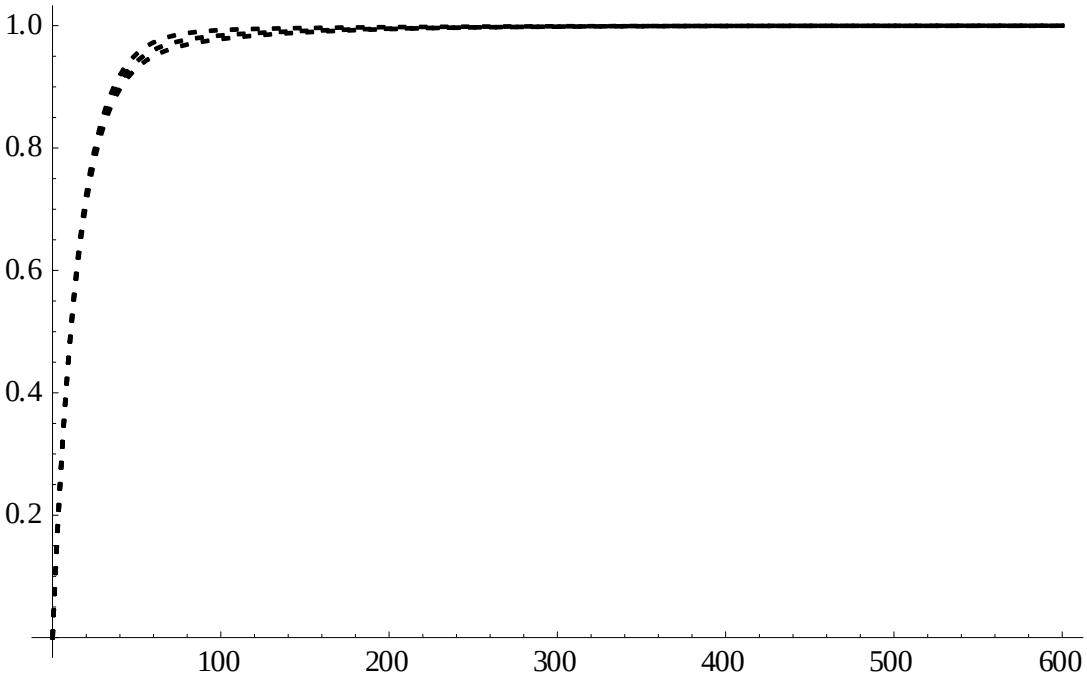

Show[%183,%186, Frame→ True]